2016

Hybrid Integrated Photonic Platforms and Devices

Jeffrey Chiles
University of Central Florida

HYBRID INTEGRATED PHOTONIC PLATFORMS AND DEVICES

by

JEFF CHILES
B.S.E.E. and B.S.C.P.E., Illinois Institute of Technology, 2011
M.S., University of Central Florida, 2016

A dissertation submitted in partial fulfilment of the requirements
for the degree of Doctor of Philosophy in Optics
in the College of Optics and Photonics
at the University of Central Florida
Orlando, Florida

Fall Term
2016

Major Professor: Sasan Fathpour

ABSTRACT

Integrated photonics has the potential to revolutionize optical systems by achieving drastic reductions in their size, weight and power. Remote spectroscopy, free-space communications and high-speed telecommunications are critical applications that would benefit directly from these advancements. However, many such applications require extremely wide spectral bandwidths, leading to significant challenges in their integration. The choice of integrated platform influences the optical transparency and functionality which can be ultimately achieved. In this work, several new platforms and technologies have been developed to meet these needs. First, the silicon-on-lithium-niobate (SiLN) platform is discussed, on which the first compact, integrated electro-optic modulator in the mid-infrared has been demonstrated. Next, results are shown in the development of the all-silicon-optical-platform (ASOP), an ultra-stable suspended membrane approach which offers broad optical transparency from 1.2 to 8.5 μm and enables efficient nonlinear frequency conversion in the mid-IR. This fabrication approach is then taken further with anchored-membrane waveguides, (T-Guides) enabling single-mode and single-polarization waveguiding over a span exceeding 1.27 octaves. Afterward, a new photonic technology enabling integrated polarization beam-splitters and polarizers over unprecedented bandwidths is introduced, called *topographically anisotropic photonics* (TAP). Next, results on high-performance microphotonic chalcogenide glass waveguides are presented. Finally, several integrated photonics concepts suitable for further work will be discussed, such as augmentations to T-Guides and a novel technique for quasi-phase-matching.

To my wife, Emily, and my family.

ACKNOWLEDGMENTS

I thank my advisor, Dr. Sasan Fathpour, for his invaluable support and mentorship throughout my Ph.D. His guidance enabled me to refine my ideas to new levels and to see a clear path to their demonstration. I am grateful to have joined his group and had such excellent opportunities for growth and learning.

I also thank my current and former colleagues, Saeed Khan, Jichi Ma, Ashutosh Rao and Marcin Malinowski for their support, friendship and appreciation of a good tangential discussion now and then.

TABLE OF CONTENTS

LIST OF FIGURES

LIST OF TABLES

LIST OF ABBREVIATIONS

ACH (state)	Asymmetric coupled hybrid
ASH (state)	Asymmetric split hybrid
ASOP	All-silicon optical platform
BOX	Buried oxide
ChG	Chalcogenide glass
dB	Decibel
E (state)	TE-only
ER	Extinction ratio
FSR	Free spectral range
GaAs	Gallium arsenide
$Ge_{23}Sb_7S_{70}$	Germanium(23) antimony(7) sulfide(70)
InP	Indium phosphide
$LiNbO_3$	Lithium niobate
M (state)	TM-only
Mid-IR	Mid-wave infrared
MLS	Multi-layer stack

MSM	Mode shape modulation
MZI	Mach-Zehnder interferometer
Near-IR	Near infrared
OSA	Optical spectrum analyzer
PBS	Polarizing beam splitter
PCMR	Polarization-cloaked micro-ring resonator
PCR	Polarization coupling ratio
PP	Periodic poling
QPM	Quasi-phase-matching
SCH (state)	Symmetric coupled hybrid
SEM	Scanning electron microscope/micrograph
Si	Silicon
SiO_2	Silicon dioxide
SiON	Silicon oxynitride
TAP	Topographically anisotropic photonics
TE	Transverse-electric
TM	Transverse-magnetic

CHAPTER 1: INTRODUCTION

The field of integrated photonics has seen vast growth since its beginnings decades ago, when it was commonly referred to as integrated optics. The promise of mass-manufacturable, compact, and reliable systems has driven much of this growth. Bolstered by advances in integrated electronics processing techniques, the performance and yield have increased to the point where commercial optoelectronic devices are routinely fabricated and sold in large quantities. More and more devices that were originally only possible using bulk optical components can now be rapidly processed on wafers containing hundreds of identical units.

There are a great many different substrates suitable for integrated photonic device processing. Since light-matter interaction forms the basis of almost all optical science and technology, the choice of material affects what sort of functions can eventually be realized. The physical form, arrangement, and composition of different materials in a substrate constitute an optical platform. A platform may range from a single-material substrate, such as bulk silicon, or an epitaxially grown stack of materials such as those found on many Gallium Arsenide (GaAs) substrates. There are many trade-offs encountered when designing and selecting the appropriate platform, such as cost, availability, process maturity, and intrinsic performance metrics relevant to the function desired. Depending on the application, it might be suitable to select an exotic, relatively expensive platform purely for its unique optical properties. The fact that optical devices typically occupy areas of only a few square millimeters means that the cost per device can still be justified, when they are processed on wafers that are several centimeters across.

The use of silicon as a photonic platform has been established for several decades, with some early versions relying on the low index contrast provided by material doping to form a waveguide core [1]. But soon afterward, another technology enabled a completely new approach and incredible

performance improvements. This was the introduction of silicon-on-insulator (SOI) wafers. SOI wafers typically consist of a thick silicon substrate (several hundred μm), with a few μm of silicon dioxide (SiO_2) on top, followed by a device layer of silicon on top of the SiO_2. The device layer ranges in thickness from tens of nanometers to a few μm. In the 1990s, SOI device layers were typically a few μm thick. But the significance of the technology was in the strong refractive index difference afforded now on all sides of the waveguide core; by etching the surface to leave an isolated silicon channel or ridge defect on a silicon slab (Fig. 1.1), on top of a silicon dioxide cladding, the light could be strongly confined to extremely small dimensions. This was previously impossible using only doping-induced refractive index contrasts. Many advanced SOI photonic devices were demonstrated utilizing this approach [2–5].

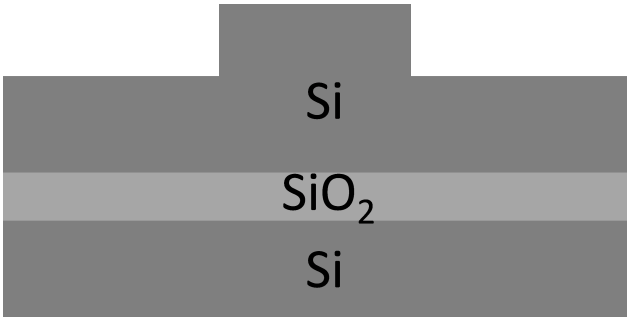

Figure 1.1: SOI optical waveguides of the ridge variety.

Since then, the compactness and performance of silicon waveguides has continued to improve. By leveraging the massive capital investment into complimentary metal-oxide semiconductor (CMOS) fabrication, it became possible to quickly and reliably produce micro- and nano-scale photonic devices using existing techniques and process facilities. New applications were envisioned for silicon photonics, such as interconnects for very-large scale integration (VLSI) chips [6].

But silicon has had one critical weakness that prevents it from achieving all basic optical functions

on one chip by itself: its indirect electronic band structure. Because of this, it cannot be used to create an efficient light generator, neither as a laser nor even a spontaneous emission source. Other materials, such as GaAs or indium phosphide (InP) have long been validated as integrated photonic platforms suitable for semiconductor optical amplifiers and lasers [7]. But they could not replace silicon for its excellence in passive waveguiding performance, so one solution that came about was to hybridize these material systems through the wafer-bonding process. In this way, the best of both worlds could be achieved. Numerous devices exploiting hybrid integration have been demonstrated such as optically-pumped [8] and electrically-pumped lasers [9].

It is safe to say that the field of integrated photonics will not likely settle on some singular ultimate platform. There are scientific and practical applications for light spanning from deep-ultraviolet (UV) all the way to the far-infrared (IR), and no known material possesses suitable optical qualities (such as transparency, nonlinearity, and resilience) over such a wide span. Nevertheless, many materials have been studied which satisfy these requirements over certain regions. The ability to freely integrate, and co-integrate, these materials into a platform will enable radically new possibilities. But most materials still lack adequate documentation in the literature. In many cases, materials are studied for applications in thin-film photonics (wherein light interacts in reflection or transmission with a normal interface), and as such, the absorption coefficient is hardly considered beyond the several-μm scale. In order for integrated photonics to assimilate more of the functions currently performed by other approaches such as fiber optics and free-space optics, especially at unusual wavelengths, the material toolbox must be expanded and unified, with these considerations:

1. Reliable methods for thin-film transfer or deposition;

2. Resulting film properties such as transparency (on the centimeter scale) and nonlinearity; and

3. Techniques for processing.

The objective of this dissertation is to address these considerations for several novel integrated photonic platforms, which will enable critical photonic functions to be performed at different wavelengths, from the visible to the mid-infrared (mid-IR). The key functions considered are, namely: broadband remote sensing, frequency conversion, and polarization control. The significance of each of these topics will now be discussed, as well as their relationship to the research outcomes of this dissertation. A graphical outline of the core topics, applications and research outcomes is provided in Fig. 1.2.

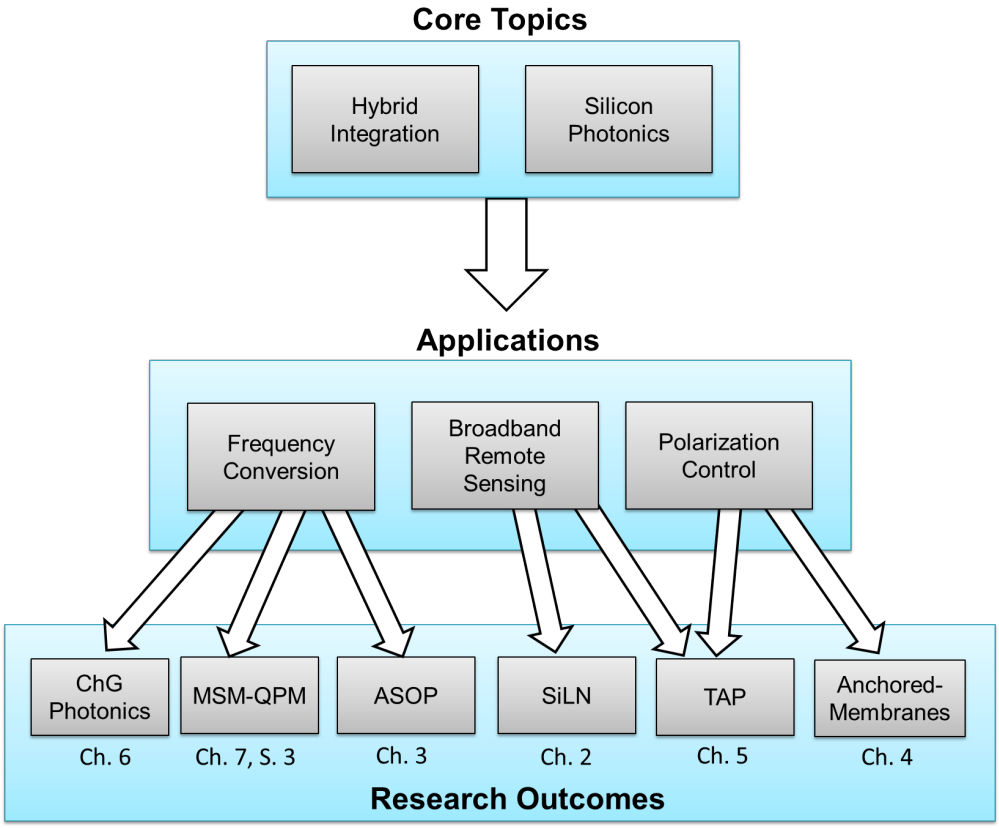

Figure 1.2: Outline of the dissertation.

1.1 Applications

1.1.1 Frequency conversion

Due to market forces driving the preferential development of certain laser lines over others, some laser sources have become ubiquitous in recent years, such as the 980 nm GaAs-based pump diode laser. This is the preferred method of pumping other lasers with emission lines in the telecom band. A similar example is the neodymium-doped yttrium-aluminum-garnet (Nd:YAG) laser, which itself acts as a conveniently available pump laser for other applications. However, emission lines are not always available at the wavelengths of operation demanded for certain applications. Thus, it is desirable to leverage these economically viable workhorse lasers in some way to access these unusual frequency domains, rather than investing an impractical amount of time and effort to develop laser systems suitable for each individual case. There are several promising methods and technologies which may be employed to realize such a frequency translation that are explored in this work.

1.1.2 Broadband remote sensing

Light is capable of propagating for extremely long distances in Earth's atmosphere, within certain atmospheric spectral transmission windows. As such, it can uncover valuable information about the atmosphere or surface features over a great distance. Moreover, optical sensing offers dramatically increased angular resolution over techniques such as synthetic aperture radar that are largely limited by the effects of diffraction. However, conventional optical remote sensing technology is rooted in bulk, free-space optical assemblies, so far as a matter of necessity. Integrated photonics could offer dramatic improvements to compactness, cost and performance, but it has not yet become a competitive alternative. The key challenges to transforming this application sector

are mainly: low propagation and insertion losses, extremely broad optical bandwidths (to allow multi-function sensing), and diverse functionality.

1.1.3 Polarization control

A key requirement in integrated photonic platforms is strict and reliable management of the state of polarization for optical channels. This has significant implications for telecommunications, on-chip laser systems, and even remote-sensing.

1.2 Research outcomes

1.2.1 Silicon-on-lithium-niobate (SiLN)

In order to truly scale down the size of a complex remote optical sensing system, it must incorporate a variety of functions. One critical function is optical modulation, which is used to provide enhanced sensitivity through coherent beam-combining receivers [10] or to provide a modulation envelope for lock-in detection. Optical modulators must satisfy the requirements of low insertion loss, high bandwidth and high extinction ratio to maximize their utility in such a demanding task. The conventional integrated photonics approaches such as free-carrier-dispersion modulators have substantial drawbacks for mid-IR operation, thus, an alternative is needed.

In Chapter 2, the SiLN platform is demonstrated, which utilizes high-quality monocrystalline silicon thin films transferred onto lithium niobate substrates to achieve efficient and high-performance electro-optic modulation on a mid-IR-compatible technology.

1.2.2 The all-silicon optical platform (ASOP)

The range of light spanning from λ = 3 - 8 μm, referred to as the mid-IR, is ideal for applications in long-range line-of-sight communications, remote optical sensing, and defense technology [11]. To support low-cost development of technology for these applications, an integrated photonic substrate with broad transparency is required. Unfortunately, the SOI platform is unsuitable due to the optical absorption of the buried oxide (BOX) layer in this region [12].

To obtain the mentioned largest intrinsic transparency window of silicon, the influence of cladding materials can be removed altogether. Suspended membrane waveguides are a technology that benefits from this, and mid-IR optical losses of 3 dB/cm have been demonstrated from suspended membranes on SOI wafers [13]. The lossy BOX layer is locally removed under ridge waveguides through a series of holes adjacent to the waveguide. However, this approach requires that the etched holes be sufficiently far from the waveguide so as to not perturb the optical mode. This results in very wide membranes with poor support and high flexure, since the oxide is removed equally in both directions from the holes. The problem is compounded for longer wavelengths, when the etched-hole separation increases. Furthermore, the trench depth must be increased to avoid radiation loss into the substrate when longer wavelengths are considered. Finally, since the BOX layer must have the same thickness as the trench, it forms an increasingly thick thermal barrier, constraining heat dissipation performance. With an ultimate goal of CMOS compatibility and practical production, these challenges must be considered in the design of a mid-IR photonic platform.

In Chapter 3, we introduce ASOP, a low-loss suspended membrane waveguide technology capable of providing extremely broadband optical transparency in the critical mid-IR region, while maintaining superior mechanical and environmental stability. Furthermore, the platform enables high-sensitivity sub-surface gas and liquid sensing through fusion-sealed internal channels. Ad-

ditionally, ASOP technology is later linked to the application of frequency conversion through on-chip supercontinuum generation, presented in Chapter 3, Section 3.4.

1.2.3 Anchored-membrane photonics

One approach to polarization management is to realize single-mode single-polarization (SMSP) waveguides, which deliberately restrict propagation to one mode of one polarization to improve the sensitivity in photonic devices [14]. The other polarization is leaked or radiated away by various means [15]. This eliminates the need for standalone polarizers and guarantees that no undesired polarization component is introduced to the system by fabrication imperfections.

In Chapter 4, the devised "anchored-membrane" waveguides, or T-Guides, are presented which show intrinsically broadband SMSP performance over record optical bandwidths, showing the potential for robust polarization-state management on a single-material, high-index-contrast technology.

1.2.4 Topographically anisotropic photonics (TAP)

The constant growth in global network bandwidth consumption has prompted the development of numerous techniques to increase the capacity of optical transceivers. Wavelength-division multiplexing (WDM), space-division multiplexing and polarization-division multiplexing are promising means of handling additional bandwidth with limited hardware [16]. Integrated photonics will play an increasingly important role in the telecommunications sector in order to reduce power consumption and costs.

The technique of polarization division multiplexing has received a great deal of attention in recent years, with the promise of potentially doubling the bandwidth capabilities of photonic in-

tegrated circuits. There are two broad strategies to achieve this. One is to design polarization-independent systems on which the waveguides exhibit practically no modal birefringence and the devices function identically for both polarizations (such as splitters, modulators, etc.). A variety of interesting approaches have been proposed to achieve this, but a complete integration has yet to be achieved. Alternatively, the transverse-electric (TE) and transverse-magnetic (TM) polarizations can be split upon entry into the chip, so that they can be routed to separate polarization-specific devices. They may be retained in the TE and TM states, or instead converted to one state with a polarization-splitter-rotator (PSR). Polarization-splitting is in general a more robust approach than polarization-independent circuits due to relaxed fabrication requirements, albeit at the expense of increased chip area. However, the performance of integrated polarization-selective devices has been greatly limited in both bandwidth and loss to date.

In Chapter 5, a novel approach called *topographically anisotropic photonics* is introduced, which employs artificially created anisotropic hybrid waveguide states to provide robust polarization management over unprecedented bandwidths.

1.2.5 Chalcogenide waveguides for Kerr-type frequency conversion

Third-order optical nonlinearities provide another potential means for achieving integrated frequency conversion, despite their relatively high intensity requirements, thanks to the small mode areas achievable with nano-scale photonic waveguides. It is critical that low-cost and mass-manufacturable technologies are developed for this purpose while achieving low losses. Chalcogenide glasses [17] can be evaporated on oxidized silicon substrates to form compact waveguides exhibiting a relatively high third-order optical nonlinearity.

In Chapter 5, a novel fabrication approach and demonstration of extremely low propagation losses in sub-micron-size chalcogenide glass waveguides is presented, opening the door for high-efficiency

nonlinear frequency conversion in a low-cost platform.

1.2.6 Raman lasers for mid-IR frequency conversion

In addition to its wide transparency window, silicon exhibits another interesting feature of strong Raman-induced optical scattering. The most useful instance of this process is known as stimulated Raman scattering (SRS). In this process, strong pump light interacts with the crystal lattice of silicon, exchanging a phonon in the annihilation of a pump photon. Depending on whether the phonon is created or annihilated, its energy will be added to or subtracted from a new photon that is generated. As such, SRS involves a virtual state, unlike the stable transitions involved in conventional lasers. However, the fact that it is a virtual state is advantageous in some respects, since it can occur for a wide range of pump wavelengths, not limited by narrow gain-bandwidths dictated by discrete transitions in ions. Consequently, SRS can be used to perform frequency conversion where convenient lasing transitions are unavailable. Silicon exhibits a large Raman gain coefficient relative to other materials, with a value of 10-20 cm/GW at 1550 nm [18]. It exhibits a small but useful gain bandwidth of 105 GHz, with a large frequency shift of 15.6 THz. SRS was first observed in silicon in 2002 [19], and was subsequently utilized for optical amplification [18] and lasing [20, 21] in the near-infrared.

In Chapter 7, Section 7.1, progress on the development of integrated Raman laser cavities on silicon substrate for mid-IR operation is presented. First, simulations and designs are investigated to ascertain the merit of different approaches such as large-core waveguides, high-contrast evaporated-film facet mirrors, and integrated distributed-Bragg-grating mirrors. These cavities are then fabricated and tested, showing promising passive optical performance which will benefit future investigations of mid-IR silicon Raman lasers.

1.2.7 Mode shape modulation for quasi-phase-matching

The use of nonlinear optical materials with second-order optical nonlinearities is the most popular means of achieving optical frequency conversion to date. Such materials lack inversion symmetry in their lattice unit cell, giving rise to an anharmonic potential. The details of its orientation as well as the arrangement of its unit cell result in certain nonlinear interaction strengths that are direction-dependent. In effect, the second-order nonlinear response of the material can be described with a tensor of these susceptibilities. For a given application, usually only one value is relevant. Paying attention to the proper polarization of the pump to maximize this strength, it can be used for the generation of new frequencies of light under high pumping intensities. However, any such conversion must satisfy both momentum and energy conservation.

Energy conservation is guaranteed by the relationships between the number and energy of the photons involved. For example, in the process of second harmonic generation, two photons at the pump frequency are consumed, giving rise to a single photon at the second harmonic, with twice their individual energies. However, the conservation of momentum demands attention to many important design details. In any normally dispersive medium, there will be a momentum mismatch between the pump and signal waves.

Several techniques have been demonstrated to date that effectively compensate this momentum mismatch through quasi-phase-matching (QPM), such as periodic poling [22] and orientation-patterned-GaAs [23]. Unfortunately, such techniques are generally suitable for only one material system, making widespread adoption to other platforms difficult.

In Chapter 7, Section 7.3, a novel concept called ”mode-shape modulation” is introduced as an alternative means of quasi-phase-matching for nonlinear frequency conversion. With this approach, the momentum difference may be compensated simply by applying a periodic variation of the

waveguide dimensions to modulate the conversion efficiency in space, opening up the possibility of efficient frequency conversion on integrated photonic material systems which are not compatible with periodic-poling or orientation-patterned-growth techniques.

CHAPTER 2: SILICON-ON-LITHIUM-NIOBATE PHOTONICS

2.1 Background

The mid-infrared (mid-IR) region of optical spectrum (3 - 8 μm) is an important range for applications in remote sensing, free-space communications, and defense technology [11]. Integrated photonics offers the best outlook for achieving these functions at low cost, while maintaining good yield and consistent performance. For the targeted applications, it is desirable to use a platform that exhibits transparency at least through the first atmospheric transmission window of 3 to 5 μm. Although the silicon-on-insulator (SOI) platform has proven highly effective for near-infrared (near-IR) photonics [6], the presence of the buried silicon dioxide (SiO_2) layer limits its usefulness in the mid-IR range due to the onset of optical absorption [12].

Alternative platforms have been proposed and explored that avoid this problem. Silicon-on-sapphire (SOS) is an existing wafer technology that has recently been used to obtain mid-IR waveguides with losses as low as 0.7 dB/cm [24, 25], but the transparency window is limited by the onset of sapphire absorption starting at 4.4 μm. We have demonstrated silicon-on-nitride waveguides with moderate losses of 5.1 dB/cm, transparent up to 6.7 μm [26]. In this chapter, the silicon-on-lithium-niobate is proposed and developed to provide new possibilities for integrated photonics in this spectrum.

2.2 The Silicon-on-Lithium-Niobate (SiLN) Platform

The choice of a photonic platform in the mid-IR should not be restricted merely to transparency considerations. A multi-element photonic circuit, such as an on-chip beam combiner [10] may

comprise numerous passive and active elements such as tunable phase shifters, optical modulators, passive routers and spectrum filters, and possibly wavelength conversion elements for accessing more efficient detectors. The materials available on the platform determine the means available to achieve these effects. Silicon photonic platforms typically enable a high integration density of passive filtering and routing elements due to the high index contrast available in their waveguides. Additionally, third order optical nonlinearities [6, 27–29] are made possible by the low multi-photon absorption in the mid-IR region, but the pump power to achieve these effects is still relatively high. Phase shifting and optical modulation has been achieved through the thermo-optic effect in silicon at speeds up to 70 kHz in the near-IR [30] and the mid-IR range at 23.8 kHz [31] on the SOI platform, but significant increases to these speeds are constrained by trade-offs with power consumption and propagation loss of the waveguides.

An alternative means to achieving on-chip phase shifts with silicon is by plasma dispersion [1], a highly CMOS-compatible approach which has been used to fabricate optical modulators in the near-IR with half-wave voltage products ($V_\pi \cdot L$) below 3 V·cm and data rates ranging from 10 to 50 Gbit/s [32, 33]. However, higher bandwidths are achieved at the expense of extinction ratio in such devices; For instance, in ref. [33], the bit rate of 10 Gbit/s achieves 18 dB extinction ratio, but in ref. [32], the higher bit rate of 50 Gbit/s is accompanied by an extinction ratio of only 5.6 dB, which is not useful for long-haul communication applications. It is thus useful to consider a figure-of-merit for the modulation performance as the product of the maximum data rate and the extinction ratio at that rate. The modulators mentioned above exhibit products of 180 and 280 dB·Gbit/s, respectively.

Furthermore, the characteristics of plasma-dispersion-based modulators will be substantially different at longer wavelengths, as is investigated in ref. [34]. Because of the stronger electroabsorption, a waveguide with a π phase shift induced from electrorefraction by free carriers would encounter an unavoidable absorption loss of 1.17 dB when operating at a wavelength of 4 μm.

This means that pure phase modulation is unachievable with this effect in the mid-IR, limiting its usefulness for applications such as on-chip beam-combining, or communication links with phase-shift-keying schemes.

Strained silicon can exhibit the Pockels effect in sub-micron waveguides in the near-IR [35], albeit with a high $V_\pi \cdot L$ of 100 V·cm. With larger waveguide cross-sections in the mid-IR, inducing strain is expected to be even more difficult.

Evidently, silicon alone may not be able to simultaneously provide all the functions required for high-performance mid-IR integrated photonics. By hybridizing it with other materials, new functions can be performed. For instance, to provide enhanced modulation performance in the near-IR, silicon organic hybrid (SOH) waveguides have been fabricated with low drive voltages down to 0.52 V·mm [36].

Meanwhile, lithium niobate ($LiNbO_3$) is a mid-IR compatible material (transparent up to 5 μm wavelength) with a high electro-optic coefficient, low refractive index ($\sim$ 2.1), and high second-order optical nonlinearity. Thanks to the fast response of the Pockels effect, near-IR $LiNbO_3$ optical modulators have achieved speeds exceeding 100 GHz [37], though with a $V_\pi \cdot L$ of $\sim$ 10 V·cm. In addition, commercially available $LiNbO_3$ modulators such as the Mach-40 005 from Covega^{TM} can provide modulation speeds of 40 Gbit/s, while maintaining an extinction ratio of 13 dB, giving a modulation performance product of 520 dB·Gbit/s, which is much higher than the aforementioned values in SOI-based devices. An optical modulator operating at a speed of 1.8 GHz and at a wavelength of 3.39 μm has been reported in Ti-diffused $LiNbO_3$ waveguides decades ago [38], but the low index-contrast available in this platform greatly limits integration density and increases the device lengths since wide gaps are required for the electrodes.

To obtain a higher index contrast, the integration of silicon and lithium niobate has been explored for near-IR applications. One approach is top-side bonding [39, 40], in which small pieces of

thin $LiNbO_3$ films are bonded on top of a silicon waveguide, so that the optical mode partially overlaps the $LiNbO_3$ top cladding. However, this approach requires extra per-device processing and is only suitable for near-IR wavelengths as it is performed on SOI substrates. Additionally, ref. [40] utilizes a polymer bonding agent, which would induce loss in the mid-IR. Amorphous silicon has also been investigated in the near-IR based on its direct deposition on $LiNbO_3$ substrates [41, 42], but the intrinsic linear loss of this material and its increasing material loss toward longer wavelengths [43] makes it unsuitable for the mid-IR spectral region.

We have recently demonstrated thin-film $LiNbO_3$ hybrid high-index contrast waveguides and modulators on oxidized silicon substrates in the near-IR [44]. The advantages over the mentioned top-side bonding approach include coupling light into $LiNbO_3$ waveguide core (rather than cladding) regions, as well as fabrication based on robust full-wafer bonding techniques rather than bonding small pieces with unreliable polymers. Unfortunately, similar to SOI, the expected loss of the oxide bottom cladding layer prohibits using our $LiNbO_3$-on-Silicon hybrid platform for mid-IR wavelengths.

To avoid material loss problems and to retain reliable wafer-scale processing capabilities, we have achieved the integration of crystalline silicon on lithium niobate substrates through direct wafer bonding and thin-film transfer techniques. We recently proposed and utilized this novel SiLN platform (Fig. 2.3) to demonstrate passive waveguides at near-IR wavelengths [45]. In contrast to the discussed $LiNbO_3$-on-Silicon platform, SiLN employs a top-silicon layer as the waveguide core material, and $LiNbO_3$ as the lower cladding. The SiLN platform has numerous practical advantages, including uninterrupted low-loss transmission throughout the wavelength range of 1.2 - 5 μm, compatibility with silicon processing techniques, and a strong effective second-order optical nonlinearity, which will greatly reduce the intensity threshold for achieving certain wavelength conversion functions.

In this work, mid-IR integrated waveguide modulators based on the SiLN platform are demonstrated, representing the first silicon-based photonic devices exploiting the Pockels effect in this wavelength region [46, 47]. First, the design and fabrication of the modulators and SiLN substrates will be described. Next, the results for passive waveguides and active devices at lower frequencies will be presented. AC modulation results at the maximum available detector speed will then be presented, followed by conclusions and remarks on the outlook of the SiLN platform.

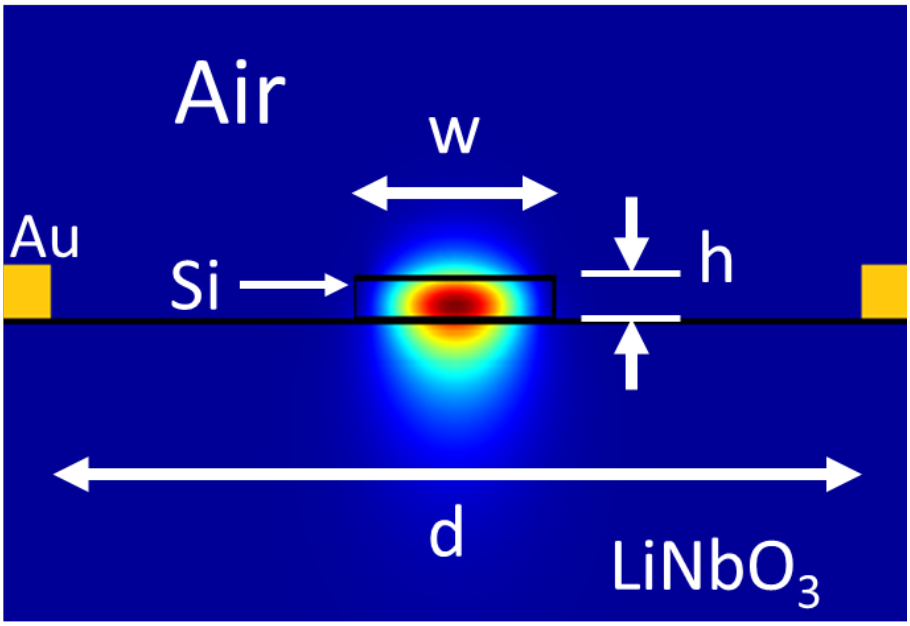

Figure 2.1: Simulated mode profile (red is the peak intensity) and modulator dimensions: w = 2.1 μm, h = 210 nm, d = 8.5 μm. The gold rectangles represent the edges of the electrodes used for modulation.

The SiLN platform consists of a bulk X-cut $LiNbO_3$ substrate, 500 μm thick, with a 210 nm-thick layer of monocrystalline silicon fusion-bonded on the top surface. This silicon layer thickness provides a large optical mode overlap with the $LiNbO_3$ substrate, while retaining sufficient mode confinement to avoid excessive bending loss at our measurement wavelength of 3.39 μm. COMSOL-based simulations of the modulator are shown in Fig. 2.1, with laterally spaced gold

electrodes creating a horizontal electric field along the z-axis underneath the fully-etched silicon channel waveguide, in order to access the largest attainable electro-optic coefficient of lithium niobate, $r_{33} \approx 31$ pm/V. The optical mode propagates along the Y-axis, with a simulated effective mode index of 2.15 for 2.1 μm-wide single-mode waveguides. The gold electrodes are spaced by 8.5 μm to avoid loss induced by optical mode overlap with the metal, with an allowance for some alignment tolerance during fabrication. The optical mode overlap into the $LiNbO_3$ substrate is 56 %. The simulated $V_\pi \cdot L$ is 13 V·cm for a push-pull configured modulator. The advantage of this modulator configuration is that there is no need to dope the silicon waveguide core (which would introduce optical loss), and it can in principle be operated at speeds well above 10 GHz, by designing the electrodes for velocity matching as in conventional $LiNbO_3$ travelling-wave modulators in the near-IR [48]. This is possible because the mechanism of modulation is the same for both SiLN and conventional $LiNbO_3$ waveguides. Additionally, due to the large optical bandwidth of Mach-Zehnder interferometers (MZIs), this modulator is simulated to achieve greater than 10 dB extinction ratio over an optical bandwidth of more than 500 nm with respect to center operation at 3.39 μm (Fig. 2.2). The bandwidth is limited by the wavelength dependence of the mode overlap into the $LiNbO_3$ substrate, which changes the $V_\pi \cdot L$ as the wavelength moves away from the center.

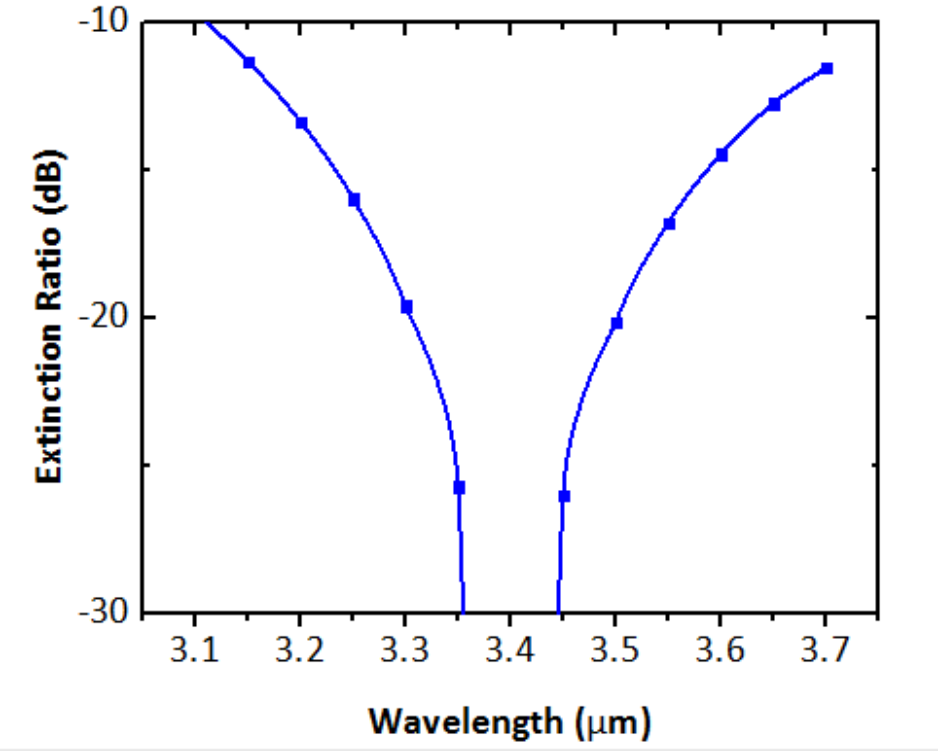

Figure 2.2: Simulated optical bandwidth of the SiLN modulator for a center operation wavelength of 3.39 μm. Blue squares show discrete simulation points and the blue line is spline-fitted.

The fabrication process for preparing SiLN substrates is schematically depicted in Fig. 2.3. A detailed discussion is available in Appendix A.1.1.

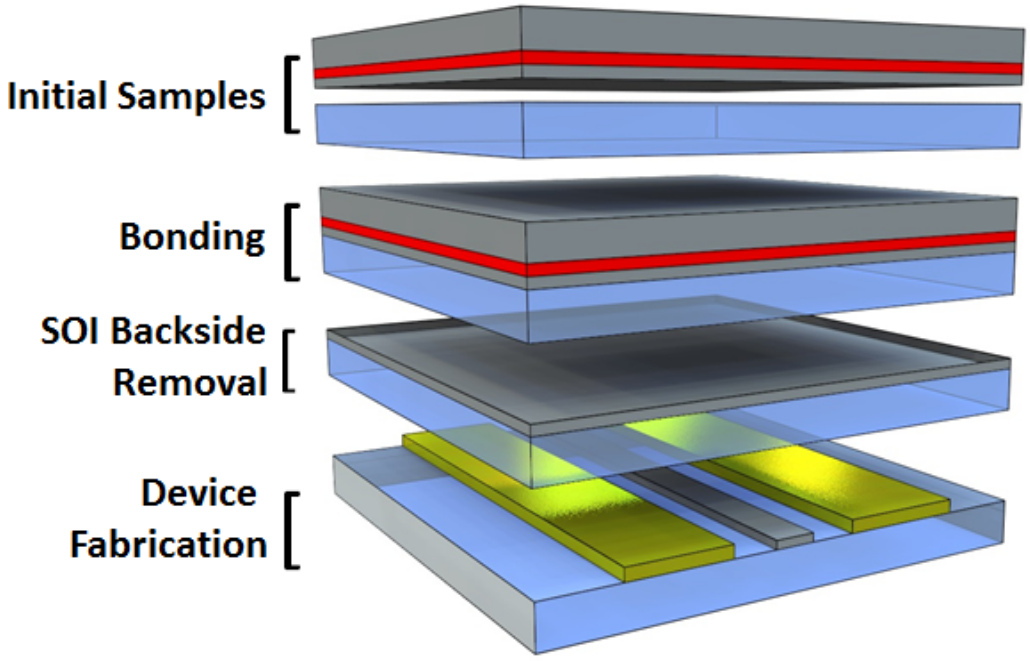

Figure 2.3: Process used to prepare SiLN chips. Grey areas represent silicon, blue represents $LiNbO_3$, red represents silicon dioxide, and gold contacts are shown in the bottom chip.

The SiLN dies were lithographically patterned into a set of MZI modulators based on Y-junction splitters and combiners, separate straight waveguides, and a small number of long-path spiral waveguides to accurately assess the propagation loss on each sample. Light was coupled in and out of the fabricated chip via 20-μm-wide, 1.7-μm-period grating couplers followed by 630-μm-long linear tapers to 2.1-μm-wide, 210-nm-thick waveguides. The active modulator section is 5 mm long. The detailed process for device fabrication on SiLN substrates is provided in Appendix A.1.2.

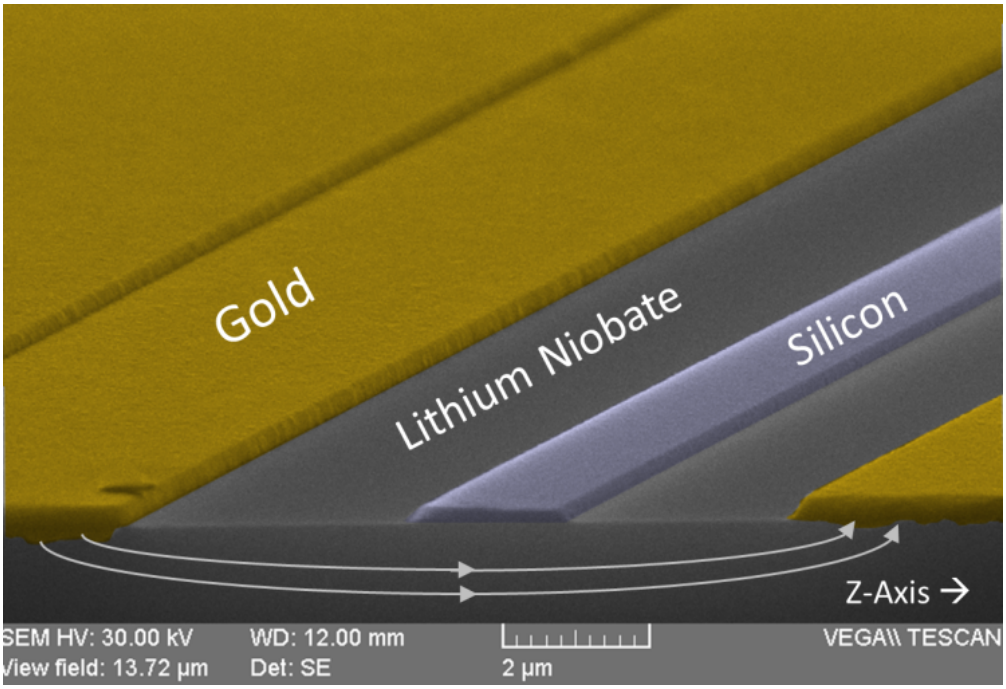

Figure 2.4: Scanning-electron micrograph of the cross-section of a SiLN modulator. The white lines crossing underneath the silicon represent the direction of the applied electric field during modulation.

The SiLN measurement setup is depicted in Fig. 2.5. A 2-mW continuous-wave (CW) Helium-Neon (HeNe) laser operating at 3.39 μm was used as the mid-IR source, coupled in through a fiber with an 18 μm core diameter at the input, and coupled out through a large-area 400-μm-core fiber to ease the alignment process. The output light was detected by a lead selenide (PbSe) detector with a specified bandwidth in the 10 kHz range. The light was chopped and then processed through a lock-in amplifier initially, but the chopper was removed once good fiber-to-grating coupler alignment was achieved.

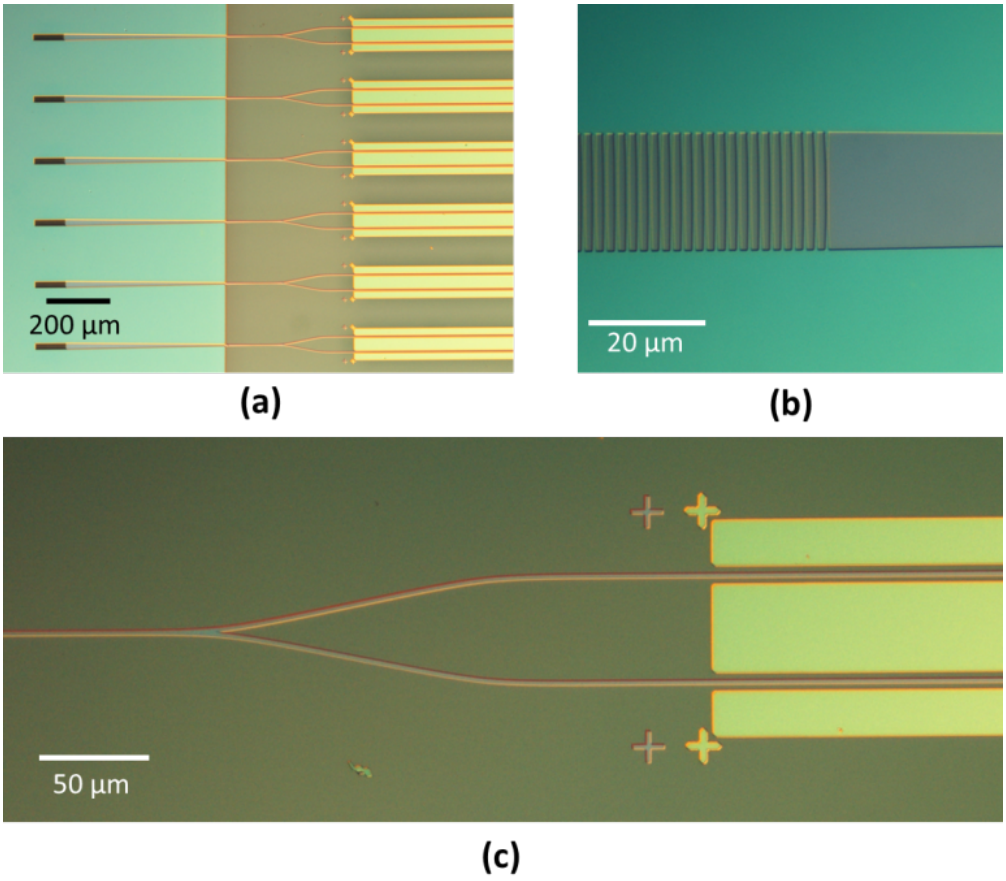

Figure 2.5: Optical micrographs of a SiLN modulator chip: (a) Wide view of chip showing half-etched (left) and full-etched (right) regions; (b) Fiber-to-waveguide grating coupler; (c) Y-junction and modulator electrodes.

First, the waveguide linear propagation loss was characterized. Straight waveguides 5.6 mm long were placed next to compact spiral waveguides which were 5.1 mm longer, using a bending radius of 300 μm. A propagation loss of 2.5 $\pm$ 0.7 dB/cm for the transverse-electric (TE) mode is obtained by the cut-back method after measuring two pairs of such waveguides. The loss figure presented is most likely not a consequence of etching-induced sidewall roughness, estimated here to be $<$ 50 nm rms, since the waveguides presented are relatively wide, and measurements of earlier produced half-etched SiLN waveguides yielded similar losses of 3-4 dB/cm. The loss may be

due to contamination at the waveguide surface. The measurement wavelength of 3.39 μm exhibits strong optical absorption with hydrocarbons, which could affect the surface of the waveguide that is exposed to air during measurements. The 400°C wet-oxidation step was crucial to reducing the propagation loss. Waveguides fabricated without this step exhibit propagation losses above 10 dB/cm. The mechanism of loss reduction is thought to be the passivation of dangling bonds at the silicon surface, reducing its adsorption of contaminants. Ultimately, the contamination-induced loss may be mitigated with use of mid-IR compatible cladding materials such as chalcogenide glasses [49] deposited on the waveguide surface, or by hermetic packaging of the devices in an inert atmosphere.

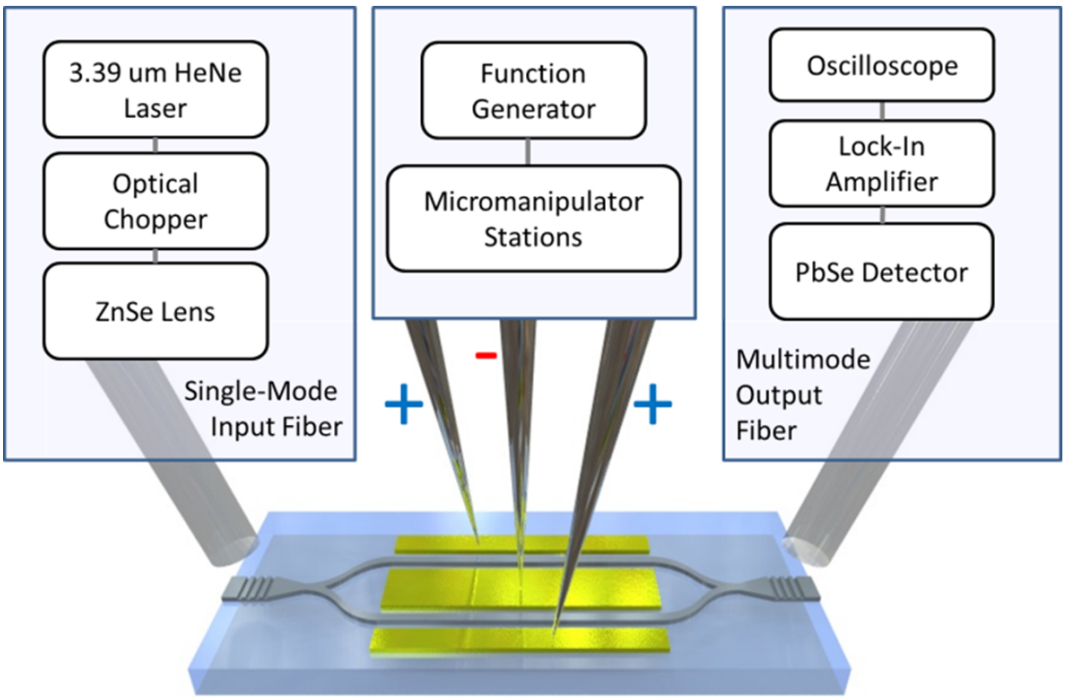

Figure 2.6: Measurement setup used for characterization.

Next, the modulators were characterized to determine the extinction ratio. The modulators were

modulator at 1/10 the frequency of the 700 Hz optical chopper used in the setup. Consequently, the square-wave chopper signal acquired a sinusoidal modulation envelope. By comparing the square-wave amplitude at the minimum and maximum of this envelope, we were able to obtain an AC-characterization of the extinction ratio (Fig. 2.7). The chopper is necessary in this setup to obtain the relative values of maxima to minima. The measured extinction ratio is $\sim$ 8 dB, which is lower than the predicted value. This can be attributed to an intensity mismatch between the two arms in the interferometer, probably resulting from small isolated interfacial bonding defects at the Si-$LiNbO_3$ interface. By using commercial vacuum wafer bonding systems, the density of these defects can be greatly reduced, resulting in higher quality surfaces and better device performance.

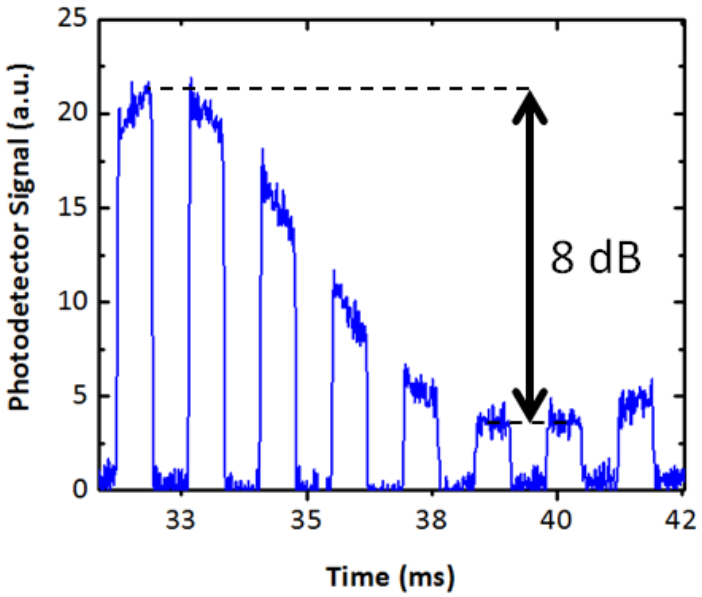

Figure 2.7: Transmission through the device during simultaneous optical chopping at 700 Hz and optical modulation at 70 Hz. The photodetector signal (blue data line) has been shifted to emphasize the envelope.

The total on-chip insertion loss of the particular modulator under consideration was determined by comparing its unmodulated transmission to that of a straight waveguide of the same length.

In addition to the modulators propagation loss of 1.4 dB, an excess loss of 1.9 dB was observed. This can be attributed to several sources, such as point defects present in the lithography on that particular device, imperfections in the nano-tip of the Y-junction splitter, and increased metal electrode proximity resulting from an alignment error of 1 μm. Because of the close proximity of the standalone straight waveguides and the modulators, the coupling loss is nearly identical (verified by repeated measurements) and thus factored out. The on-chip insertion loss of the modulator is measured to be 3.3 $\pm$ 0.7 dB.

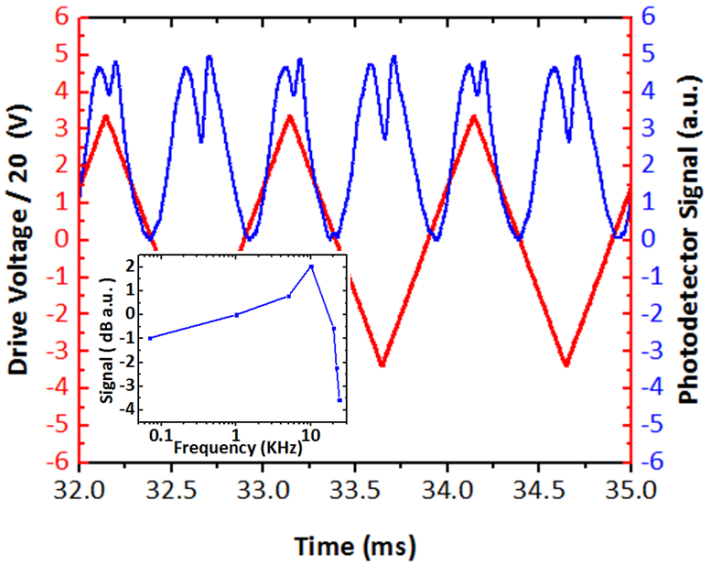

Figure 2.8: SiLN modulator response. The red line is the modulator drive voltage divided by a factor of 20, and the blue line is the optical signal transmitted through the modulator, shifted for visibility. The inset shows the frequency response, limited by the detector speed.

The measurement of the $V_\pi \cdot L$ was performed at 1 kHz (Fig. 2.8). The modulator was also measured out to the limit of the photodetectors bandwidth at 23 kHz (inset of Fig. 2.8), revealing an uneven frequency response of the detector at its limit. The slight distortion in the peaks of the signal is due to this behavior. The modulation speed measured in this experiment was limited by the speed of the detector available. With faster detectors and probes, and with travelling-wave

electrode design, high-speed performance ($>$ 10 GHz bandwidth) mid-IR modulators are in principle feasible similar to conventional near-IR $LiNbO_3$ devices. Finally, to rule out the possibility of leakage effects and heating-induced phase changes, a multimeter was inserted into the voltage drive circuit, but no current flow was detected (sensitivity limit was 0.1 μA) indicating negligible power consumption at low frequencies.

The obtained $V_\pi \cdot L$ value from the modulation response is 26 V·cm, which is larger than the 13 V·cm value predicted in simulations. This difference is most likely not a result of dispersion in the r_{33} coefficient (which is negligible) [38]. One possible explanation could be the well-known phenomenon of domain realignment in $LiNbO_3$ after exposure to high-energy electron beams [50] such as the one used in pattern writing. Accordingly, the domains underneath the waveguide could be misaligned with respect to the polarization axis, causing a lowered effective electro-optic coefficient. Future studies with photolithography-patterned devices can investigate this possibility in order to resolve the discrepancy between measured and simulated values of $V_\pi \cdot L$.

2.3 Conclusion

Optical modulation in the mid-IR range has been demonstrated on the proposed SiLN platform, utilizing the Pockels effect. A maximum modulation frequency of 23 kHz was observed (limited only by the detector speed), with an extinction ratio of $\sim$ 8 dB, an on-chip insertion loss of 3.3 dB and a $V_\pi \cdot L$ of 26 V·cm, at a measurement wavelength of 3.39 μm. In addition, optical waveguides were characterized on the SiLN platform in the mid-IR, showing low TE-mode propagation losses of 2.5 dB/cm. With its compact waveguides, high electro-optic sensitivity, and strong second-order nonlinearities, this platform will enable high-performance photonic chips to be created for mid-IR applications.

CHAPTER 3: THE ALL-SILICON OPTICAL PLATFORM

3.1 Background

In the Introduction, we discussed the need for a robust integrated platform capable of supporting optical waveguiding across the mid-IR spectrum from λ = 3 - 8 μm. In this chapter, we introduce the all-silicon optical platform (ASOP), which takes advantage of hybrid integration techniques to allow the fabrication of previously impossible structures for this purpose.

3.2 Design and implementation

We have built on previous suspended-membrane waveguide research [13] and designed a new platform that addresses many of the above practical issues facing photonic device fabrication [51, 52]. Using direct silicon bonding, a thin silicon membrane is fused to a bulk silicon substrate that has been pre-patterned with trenches, forming highly compact suspended membranes on this all-silicon optical platform (ASOP). Waveguides are then formed by standard lithographic techniques on the membranes (Fig. 3.1). The detailed fabrication process is described later in Appendix A.2. The ASOP frees us from many constraints inherent to SOI-based membranes. Since the trenches are formed on a separate substrate, any depth can be chosen to suit the wavelength and substrate leakage requirements. Additionally, since there are no etched holes or perforations, the membrane is much stronger and exhibits less flexure. As a result, the waveguides can be etched deeper and the membrane width can be shrunk to unprecedented values. The combination of arbitrary trench (lower cladding) depths and greatly reduced minimum membrane widths allows the ASOP to guide light over silicons transparency range of 1.2 to 8.5 μm; the loss figure is unaffected by any external material limitations. To further demonstrate the robustness of ASOP waveguides,

COMSOL^{TM} simulations were conducted to confirm that low-loss mid-IR waveguiding at the wavelength of λ = 3.39 μm with a total membrane width of only 5 μm is feasible. The leakage loss into the bulk silicon accounts for < 0.1 dB/cm for both the transverse electric (TE) and transverse magnetic (TM) polarizations. Such a design is not practical with the previously reported SOI-based membrane waveguides.

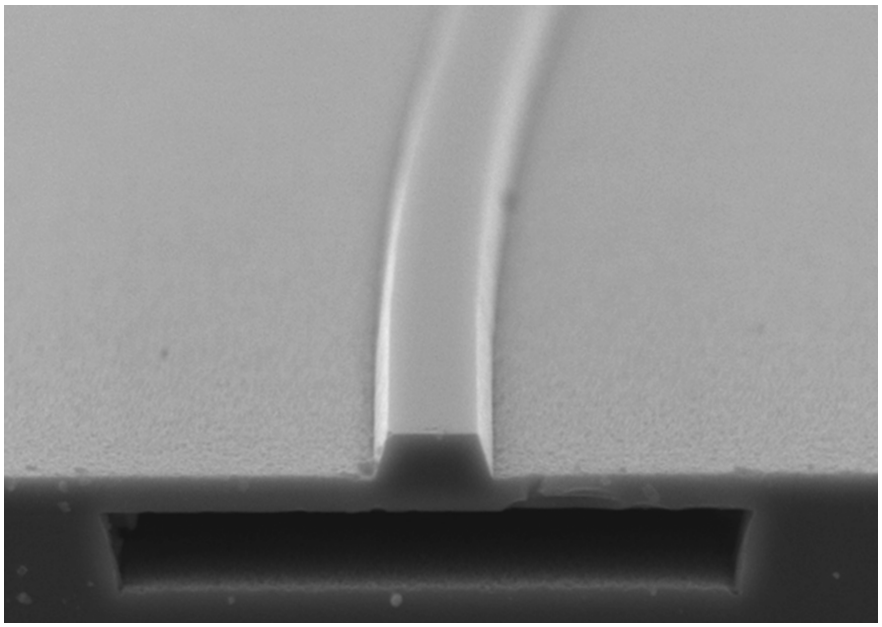

Figure 3.1: Scanning electron microscope (SEM) image of a fabricated waveguide. The fabricated waveguides are 2.4 μm wide, and have ridges that extend by 1.07 μm above the membrane. The membrane width is 17 μm, and the trench depth is 2 μm. No boundary is visible between the bonded silicon layer and the bulk substrate, indicating the high quality of the achieved fusion bond.

Our approach offers other advantages, including enhanced device-layer thermal conductivity [53], and the option for low-resistance contacts to the substrate to be formed at the bonding interface when hydrophobic bonding techniques are used [54]. In this way, a photonic device can be fully patterned and delivered to a CMOS foundry that processes bulk silicon, rather than SOI, substrates. All of these advantages represent a significant step forward in the realization of a practical mid-IR

photonic device platform.

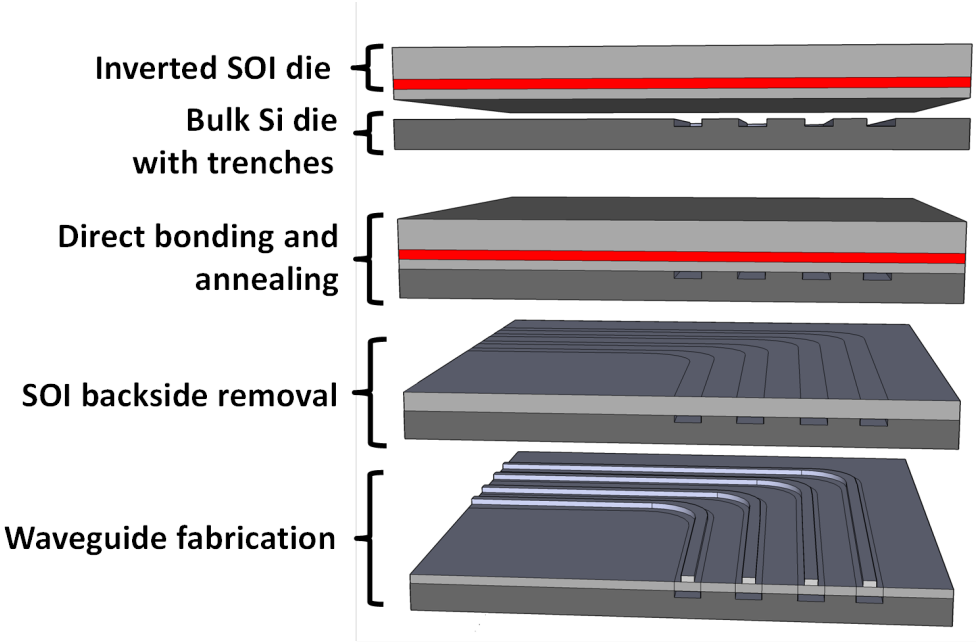

Figure 3.2: Simplified representation of the fabrication process used to produce ASOP waveguides.

A schematic of the fabrication process is provided in Fig. 3.2. Details on the process of preparing of ASOP samples are available in Appendix A.2. Samples $\sim$ 1 x 1 cm^2 were prepared with a top silicon thickness of $\sim$ 2.14 μm. The waveguides were found to be 2.4 μm wide, with 1.07 μm thick membranes (slabs) and 1.07 μm thick ridges.

Overall, the bonding quality was very high, with only a few unbonded regions in the various samples. In some cases, small bubbles appeared, but occupied only a very small fraction of the chip. The average yield for most samples was over 90% at the point of backside removal. A few waveguides were damaged during the dry etching procedure, most likely due to the $\pm$ 25% non-uniformity of the silicon device layer thickness from the SOI substrate. It is also important to consider that this particular fabrication approach is chosen only because of the limited available

equipment. When extended to a commercial process, a combination of ion-implantation, chemical mechanical polishing (CMP), and machine-automated wafer bonding may be used. This is a well-known process used to economically produce many technologies, including SOI wafers [55].

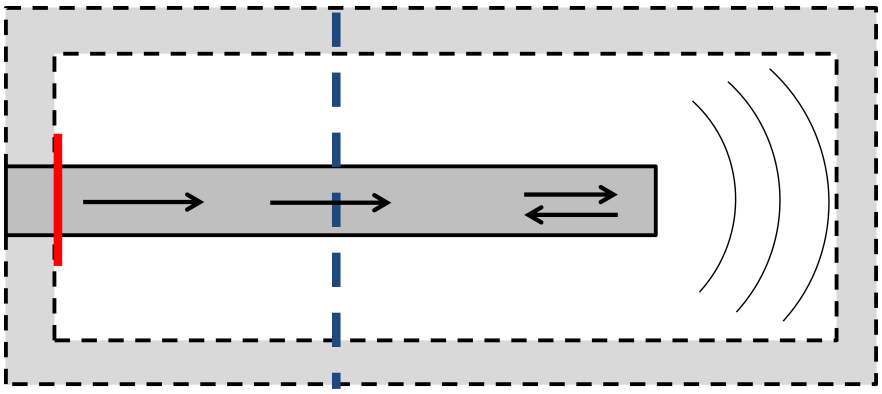

Figure 3.3: Schematic view of the 3D simulation used to determine the precise reflection coefficient of the fabricated waveguide facets. The red boundary is the source excitation point, the blue dashed line is the power monitor location, and the gray shaded region is the perfectly absorbing boundary space. Power flow is indicated at a particular point in time as forward or backward arrows and radiating arcs.

The ASOP-based waveguides were then characterized to determine their optical propagation loss. The exact reflectivity of the waveguide facets, necessary for Fabry-Perot loss measurements, was determined by a full 3-D finite-difference time-domain (FDTD) simulation using the free, open-source MEEP software package [56]. Our custom simulation approach is depicted in Fig. 3.3. The fundamental mode is excited at the beginning of the waveguide, and traverses a power monitor boundary, which registers the input power level. When the optical wave reaches the boundary, some of its energy is reflected off the perpendicular air interface, and some is transmitted and absorbed by the boundaries. The reflected portion in the waveguide passes through the power monitor again, causing a change in the power flow vector which indicates the amount reflected. The simulation was tested to confirm that boundary reflections and scattered light had only a small effect on the result. This was achieved by monitoring the optical power at several locations along

the waveguide and averaging the calculated values. The simulated single-facet reflectivity R = 0.35 for the mid-IR TE-polarized mode is significantly different from that predicted by the generic Fresnel equation (which predicted R = 0.29). This discrepancy is a known characteristic of optical guided modes with highly diverging output beams [57]. Near-IR propagation loss measurements were conducted in order to obtain accurate lengths of the waveguides and to assess the short-wavelength performance. An optimal TE-mode loss of 5.4 $\pm$ 0.2 dB/cm and a TM-mode loss of 5.6 $\pm$ 0.3 dB/cm were obtained by scanning a semiconductor tunable laser source from 1530 to 1531 nm (Fig. 3.4(a)). Next, the waveguides were characterized using a 2 mW Helium-Neon (HeNe) laser at 3.39 μm to determine their mid-IR performance. The photonic chip was placed on top of a thermo-electric cooled pad, which enabled the measurement of Fabry-Perot interference fringes through temperature tuning. The experimental measurement method and setup is the same as in our previous work on SON waveguides [26]. The lowest loss observed for the TE-polarized mode was 4.0 $\pm$ 1 dB/cm. The TM-polarized mode exhibited a minimum loss of 2.8 $\pm$ 0.5 dB/cm. The waveguides had a length of about 5-7 mm. Examples of the recorded data are presented in Fig. 3.4(b). The propagation loss is probably due to small defects in the waveguides from lithography, and from roughness of etched sidewalls.

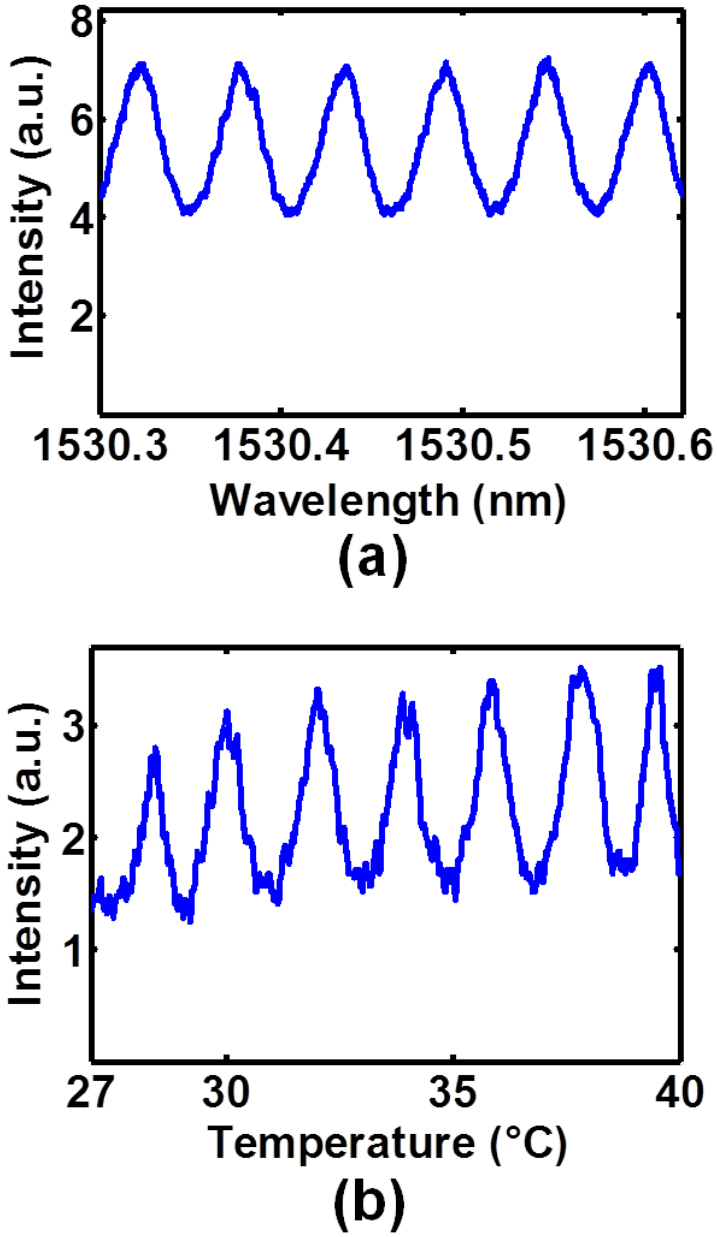

Figure 3.4: Fabry-Perot interference fringes recorded from a fabricated waveguide; (a) TE-mode near-IR data obtained by sweeping a tunable source at λ=1.53 μm; (b) TE-mode mid-IR data obtained by tuning the temperature of the chip from 27 to 40°C.

The waveguides exhibited somewhat higher propagation loss at near-IR wavelengths compared to mid-IR. A similar discrepancy was observed in our previous work on SON waveguides [58]. A probable explanation for this is a partial coupling of input light into higher-order modes when measuring at near-IR. Since these modes (which are confirmed to exist in simulations) have greatly increased propagation loss compared to the fundamental mode, the fringe contrast in Fabry-Perot measurements is reduced, leading to a higher apparent propagation loss value.

In summary, a single-material waveguiding platform for future mid-IR photonic applications, the ASOP, is demonstrated. By using direct bonding, totally unperforated, air-clad silicon membranes were fabricated and patterned with low-loss waveguides. The fabricated waveguides have a minimum mid-IR TM-mode propagation loss of 2.8 dB/cm, and a width footprint of only 17 μm, which can easily be reduced to 5 μm or less. The ASOP represents a significant improvement on previous suspended-membrane waveguide technology, with greater mechanical robustness, a more compact waveguide footprint, and better scaling to longer wavelengths due to the elimination of geometrical trade-offs with trenches and etch-holes.

3.3 Directly-written ASOP waveguides

In the previous section, μm-scale waveguides with low losses were presented for mid-IR operation using ASOP. A desirable goal for this platform is to take advantage of its geometric flexibility, and to minimize the on-chip footprint and increase the mechanical robustness even further. To this end, a modified design and process was developed. In order to enable simple testing of the devices and process, near-IR operation (1550 nm) was chosen for this test.

First, silicon samples were trench-patterned similar to the previous work, but with narrower trenches of $\sim$ 10 μm. A depth of 800 nm was etched for the trench. A silicon membrane 220 nm thick

was suspended over the trenches using argon/oxygen surface activation and wet backside removal. In order to facilitate flexible patterning of the samples with simple alignment, a novel approach of direct laser writing was employed, using the commercially available Nanoscribe dip-in laser lithography (DILL) system. With this technology, a liquid resist can be polymerized at a precise 3-dimensional coordinate, enabling high-resolution 2D or 3D patterning on a substrate. Using the Nanoscribe, polymer etch masks for microring resonators with 90-μm-radii were directly patterned on top of the suspended silicon membranes after backside removal (Fig. 3.5).

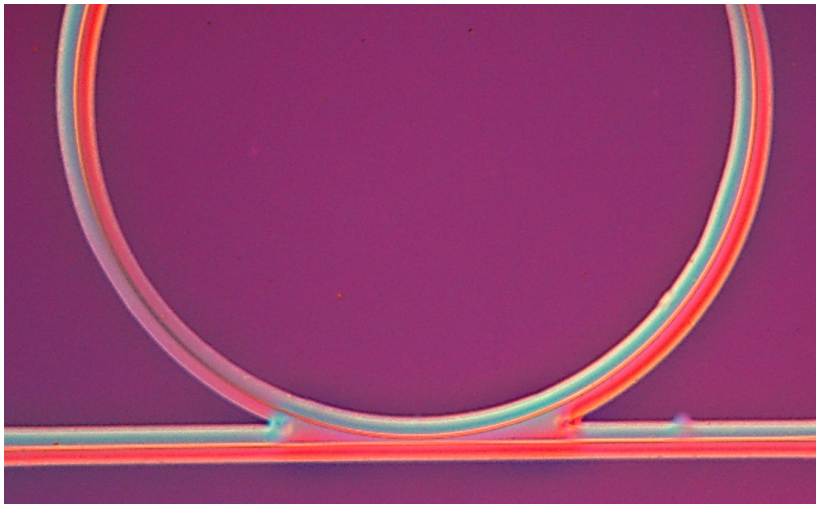

Figure 3.5: Optical microscope image of ASOP ring resonator structure patterned with direct laser lithography.

A simple optical microscope view was utilized to ascertain the correct overlay alignment for the structure. The waveguide width written was 430 nm, and the etch depth was 70 nm. The devices were tested via grating couplers, and the observed microring response is shown in Fig. 3.6. The estimated loaded quality factor (Q-factor) of the resonator is 15,600 $\pm$ 1000. The relatively low quality likely originated from contamination unintentionally introduced in the development process, as unwanted residue was redeposited on the surface and etched into the slab area. Never-

theless, this experiment validated the stability of ASOP waveguides at greatly reduced dimensions and opens up a new means of flexible processing using laser lithography at sub-μm dimensions, saving significant costs over electron-beam lithography.

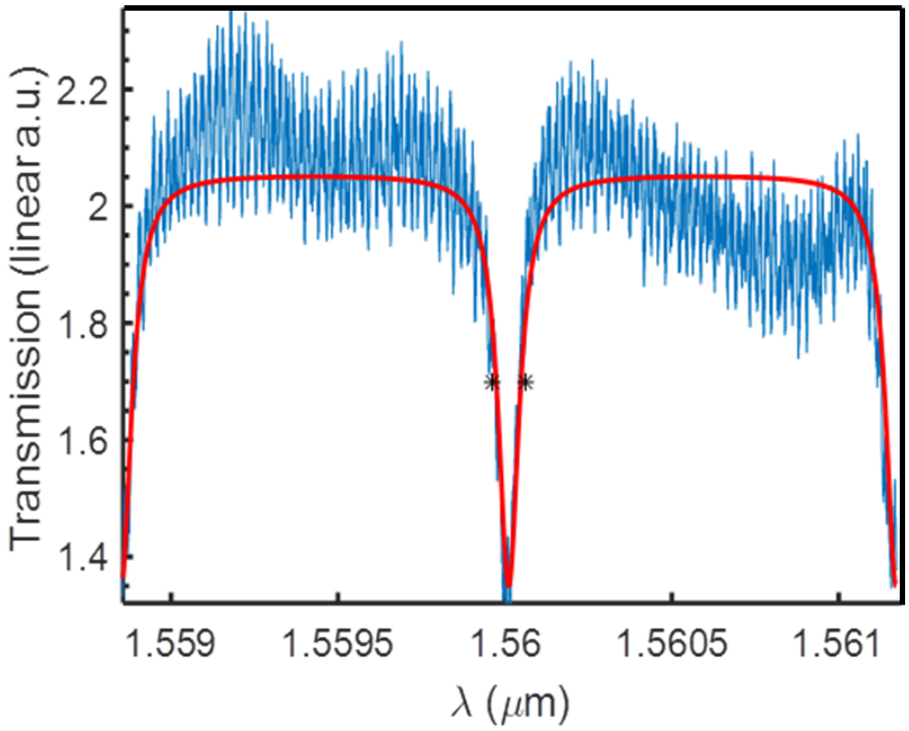

Figure 3.6: Transmission spectrum of measured ASOP ring resonator.

3.4 Mid-IR supercontinuum generation on ASOP

The wide transparency, compactness and design flexibility of ASOP are highly useful for on-chip frequency conversion in the mid-IR. For applications such as atmospheric spectroscopy, light sources must cover a broad spectrum and have excellent coherence properties. Supercontinuum generation is a means of expanding the spectral coverage of narrower pulsed light sources such as

waveguides [60] and 2-6 μm in SOS waveguides [61] previously. In both cases, the spectrum is limited by the material absorption of the substrate. As a single-material platform, ASOP naturally avoids this issue, potentially allowing much broader spectra out to 8.5 μm.

We have conducted an initial investigation into supercontinuum generation on ASOP in a collaboration with Dr. Barry Luther-Davies research group at Australian National University. Different designs were investigated to find the ideal dispersion characteristics for broader spectra. Measurements were conducted at ANU, making use of a pulsed mid-IR source with a peak power of 2-3 kW and near diffraction-limited beam quality. The spectrum was recorded by sweeping the output through a monochromator.

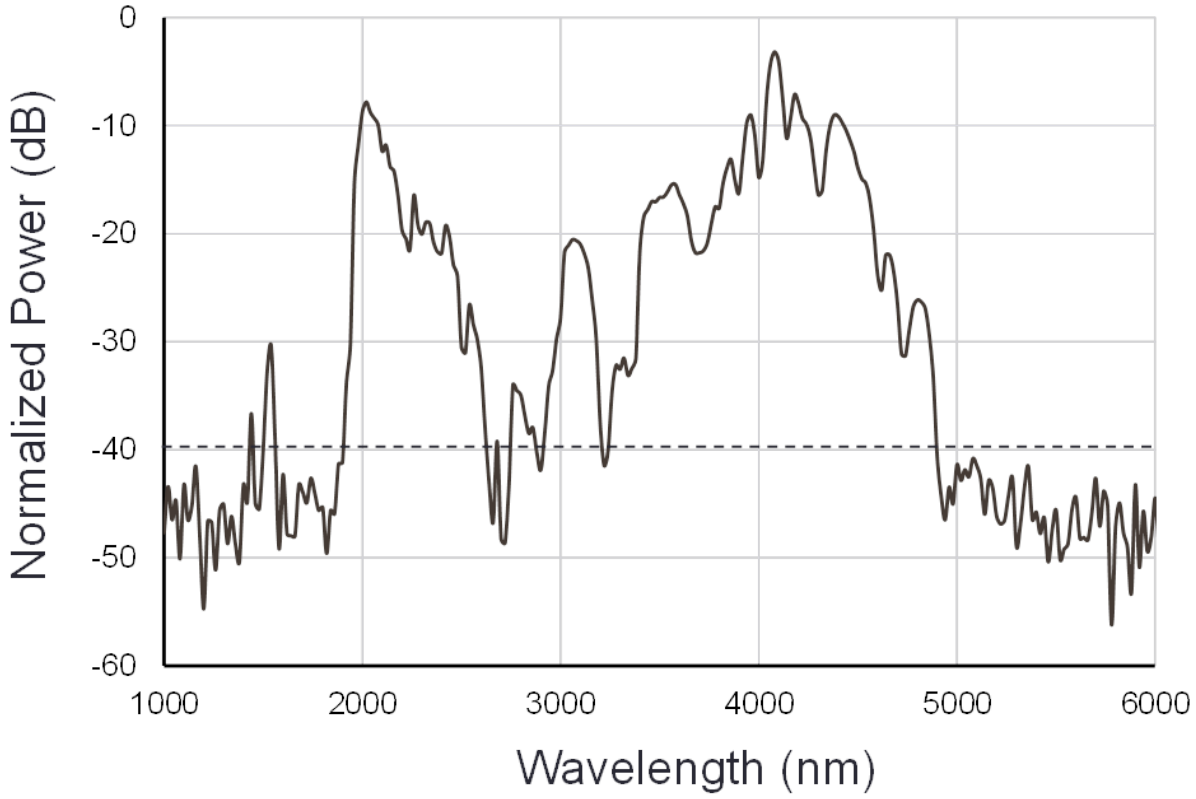

Figure 3.7: Broadened supercontinuum spectrum after propagation through a 2 μm thick ASOP waveguide.

In the first round of fabrication, silicon membranes of 2 μm thickness were used in the ASOP waveguides. Waveguides with widths ranging from 2-5 μm were fabricated, ranging from about 1-2 cm in length. An etch depth of approximately 1 μm was used. They were pumped at λ = 3.9 μm with an average power of 54 mW prior to waveguide coupling. The best waveguide measured, which had a width of $\sim$ 6 μm and a length of 20 mm, exhibited a maximum broadened spectrum from 2 to 5 μm, as seen in Fig. 3.7. It can be seen that the spectrum is highly nonuniform, however, a result which is explained by the non-ideal dispersion characteristics present in the 2 μm-thick film. This thickness was chosen simply to perform initial experiments before thinner films could be

obtained (which have more promising dispersion). Additionally, the 2 μm-thick silicon membrane had a large thickness nonuniformity of $\pm$ 500 nm, which could vary over short distances, resulting in unpredictable behavior in the waveguides due to variations in mode coupling. Nevertheless, this first experiment showed that broad spectra were achievable through supercontinuum generation in ASOP waveguides.

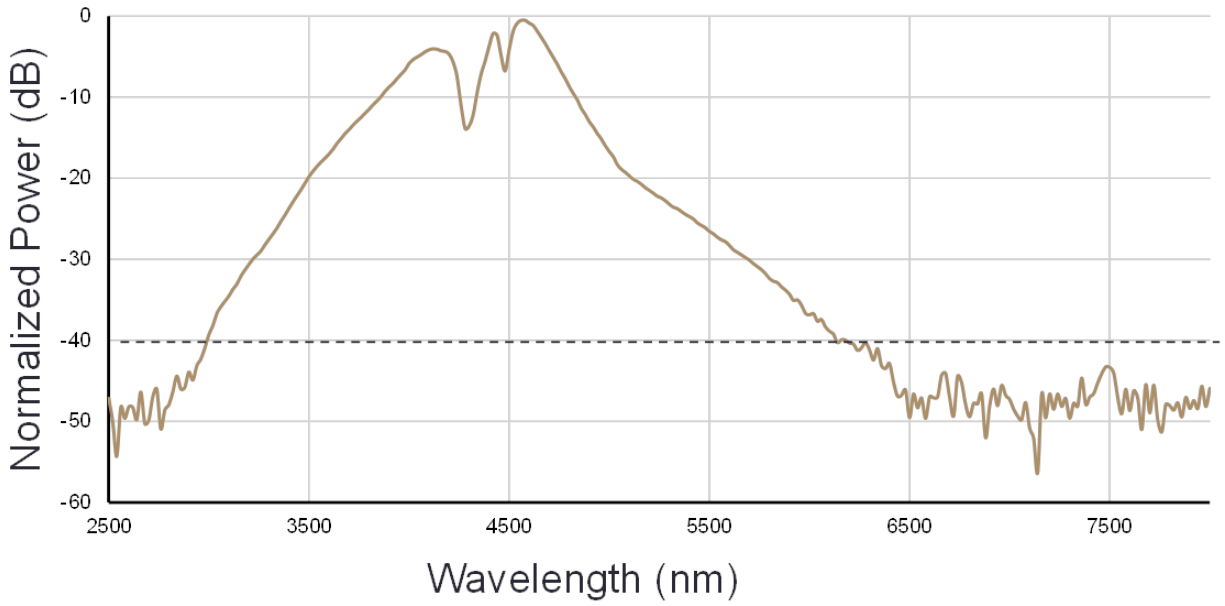

Figure 3.8: Broadened supercontinuum spectrum after propagation through a 1.3 μm thick ASOP waveguide.

The second round of fabrication utilized higher-quality SOI wafers from Okmetic to act as the donor substrates. These wafers had a nominal silicon membrane thickness of 1.3 μm and a typical nonuniformity $\pm$ 200 nm, although $\pm$ 300 nm was possible in some locations. As such, it was still a significant improvement over the tolerances available from the previous wafer supplier. It was also much closer in thickness to the ideal 1 μm value. Waveguides were fabricated with widths from 2-4 μm, lengths from 1-2 cm, and an etch depth of 1 μm. The best waveguide, with a width of

4 μm and a length of 10 mm, measured exhibited a broadened spectrum from 3 to 6 μm (Fig. 3.8, a result competitive with prior results in the mid-IR to date [60, 61]. The smoothest spectrum was achieved when a pump power of 30 mW was supplied at λ = 4.4 μm. Although slightly broader spectra were obtained upon increasing the pump power to 100 mW, this also resulted in large oscillations imposed on the spectrum, which limit its usefulness for sensing applications, where smooth and consistent spectra are required. On the long wavelength side of the spectrum, the broadening appeared to be limited by the propagation loss of the waveguides. This could partly be due to sidewall roughness during the etching, made more significant due to the increased sidewall interaction of the optical mode at longer wavelengths. Another explanation could be doping effects in the silicon membrane. The device layer was specified to have a nominal resistivity of 10-22 Ω·cm, which can result in significant losses in the long-wavelength regime due to the quadratic dependence of free carrier absorption with wavelength. A related issue could be the transfer of impurities into the silicon membrane after etching and annealing of the films at high temperatures, due to the presence of byproducts sputtered or adsorbed onto the silicon surface. This could result in further degradation of the material. Further work should be conducted to quantify any such effects and also to find strategies for mitigating them in order to push the performance of silicon to longer wavelengths.

3.5 Conclusion

In this chapter, the motivation, development, and demonstration of ASOP technology was outlined. Low-propagation-loss waveguides were tested in the mid-IR spectrum, showing high mechanical stability and compactness. Additionally, a novel approach to suspended waveguide patterning using dip-in laser lithography was demonstrated. Finally, octave-spanning supercontinuum spectra were observed by pumping dispersion-engineered ASOP waveguides in the mid-IR.

CHAPTER 4: ANCHORED-MEMBRANE PHOTONICS

4.1 Introduction

Modern integrated photonic platforms ought to achieve high optical confinement, low core and cladding material loss over a wide spectral range and polarization-state management. Wide transparency enables the same platform to be used for multiple applications requiring different wavelengths, taking full advantage of the compactness offered by an integrated approach. Polarization management is key to implementing sensitive on-chip measurements. The use of single-mode single-polarization (SMSP) waveguides provides a reliable solution by guaranteeing that only one polarization state of light is permitted to propagate in a waveguide.

Extensive work on the design and simulation of SMSP in the context of optical fibers has been conducted [62, 63], with predicted SMSP windows of up to 2.62 octaves [64]. However, the experimentally achieved fibers have fallen far short of such figures with a maximum measured window of only 0.23 octaves [65]. This low value is partially due to the inherent complexity of perfectly realizing the intricate geometries of these structures.

In the context of integrated photonics, however, little work has been done on SMSP waveguides. To achieve compact, low-cost devices, operation on the centimeter scale is desirable, which is possible through microfabrication processing techniques. There are several integrated photonic applications that could benefit from SMSP operation. On-chip optical gyroscopes have the potential to provide reliable navigational data in a compact form-factor and at low cost. However, polarization fluctuations inherent to bipolarized waveguides (supporting modes of both polarizations) can impose limitations to their sensitivity [66]. With SMSP waveguides, this problem could be addressed readily. Another application for SMSP waveguides is for on-chip supercontinuum generation, which

could improve polarization purity and beam quality by restricting propagation to a single mode. Spectra exceeding one or multiple octaves have been generated in standard waveguides with no polarization management [67, 68]. Thus, the demand in SMSP bandwidth would be much greater than what has been achieved to date.

It is well-established that operation with only the transverse electric (TE) mode can be achieved in ridge waveguides, when they are shallowly etched [69, 70]. Single transverse-mode operation can also occur in such shallow ridge waveguides with small enough widths. However, the trade-off to such a design is that only small index contrasts are achieved, resulting in large modes and poor confinement. Thus, this approach is not suitable for dense photonic integration or nonlinear applications requiring a small mode area.

Alternative approaches to single-polarization waveguides have been considered [71, 72]. A type of pedestal silicon waveguide was proposed in [72], but the technique is limited to using waveguides close to the confinement limit. This, combined with the asymmetry of the structure, causes the TE-mode to cut off at relatively short wavelengths, giving a limited predicted SMSP spectrum from 1.43 to 1.84 μm (0.36 octaves) for a challengingly narrow pedestal width of 100 nm (simulated in-house with COMSOL$^{\text{TM}}$). Propagation losses greater than 19 dB/cm were measured for the fabricated samples in [72].

Clearly, waveguide platforms with much broader SMSP bandwidth and much lower propagation losses are required to be useful as in-line polarizers. In this chapter, we show extremely broad SMSP windows and ideal dispersion profiles can be achieved with a novel structure we call the T-Guide [73, 74].

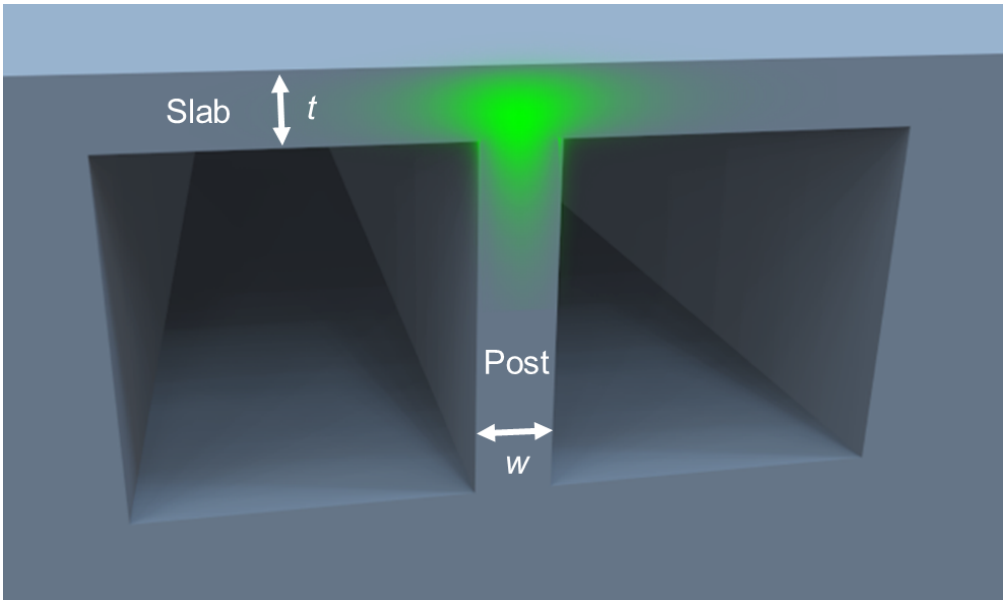

Figure 4.1: Geometry of an anchored-membrane waveguide or *T*-Guide. The simulated intensity profile of a typical guided mode is overlaid at the junction between the post and the slab.

The proposed platform is schematically shown in Fig. 4.1. Resembling our prior demonstration of all-Si suspended-membrane waveguides [51], this structure can be readily fabricated; essentially, the processing consists of patterning a handle wafer with two trenches separated by a narrow post, followed by transfer of a thin layer of material (the slab) on top, forming a guided mode at the junction between the post and slab.

The unique geometry of the proposed structures results in exotic behavior such as ultra-broadband SMSP operation, as well as flexible dispersion engineering and precise control over mode shape and positioning. Also, since no cladding materials are needed, the transparency window is limited only by the core material chosen, making the structure ideal for tougher wavelengths such as the mid-IR [11]. This feature complements the *T*-Guides ultra-broadband SMSP window and is a clear advantage over prior mid-IR Si platforms, such as silicon-on-sapphire [24] and silicon-on-nitride [26]. Additionally, a high index contrast can be retained in the waveguiding structure

thanks to the air interfaces on all sides, allowing compact waveguide dimensions. In this work, the fundamental waveguiding behavior, SMSP operation, and dispersion engineering of silicon T-Guides are considered.

4.2 Properties of optical modes in T-Guides

4.2.1 Waveguiding behavior

To explain some of the unusual optical properties of T-Guides, it is helpful to first consider their fundamental waveguiding behavior. They bear some similarity to conventional ridge-type optical waveguides in that the optical mode is laterally confined by a defect in the slab thickness. But the guiding defect in this case is a post, which is semi-infinite in its height because it adjoins with the substrate. This produces markedly different optical properties from conventional ridge waveguides or truncated ridge-type waveguides, such as those simulated in [75]. In the same way that some ridge waveguides are able to leak and thus extinguish higher-order lateral modes [76], T-Guides are capable of doing so in both lateral and vertical directions, since the structure is semi-infinite in both directions. Unlike in ridge waveguides, however, widening the post of a T-Guide will not result in additional lateral modes, as they would simply be leaked to the substrate through the post. Similarly, increasing the slab thickness cannot result in additional vertical modes, since only one field lobe can occupy the junction where the local increase in effective index occurs. Numerical results presented later confirm that no higher-order modes are present for any T-Guide design across the multiple octaves simulated.

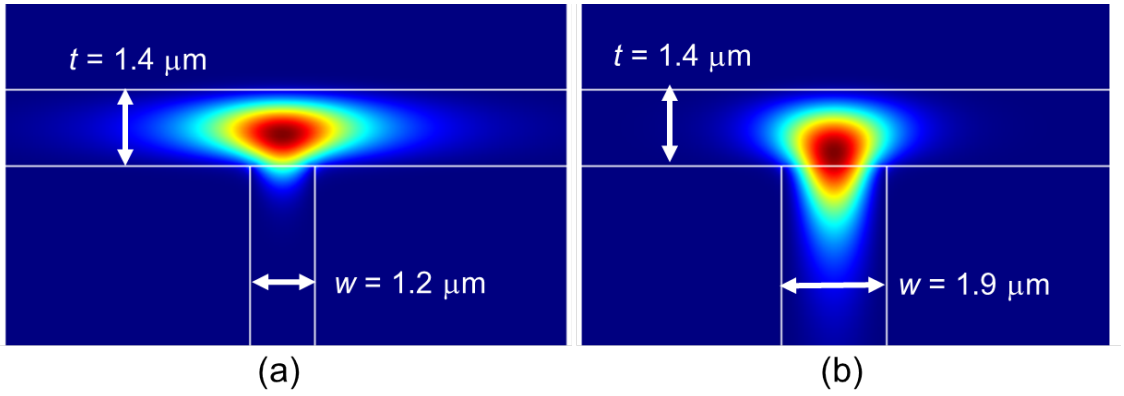

Figure 4.2: Simulated intensity profile of the TE mode for different post widths (a) w = 1.2 μm; (b) w = 1.9 μm.

An intuitive understanding of the guiding behavior of *T*-Guides can be gained by considering it as a competition between the planar modes of the slab and those of the post. To illustrate this, we consider the quasi-transverse-electric (TE) guided modes (intensity distribution) in the structures of Fig 4.2, which employ silicon as the core material, bounded by air on all sides. The confinement of the mode in the slab and post regions is determined by the effective index contrast between the guided mode and that of the respective planar mode in each region. For the slab region, this is a TE-like mode. For the post region, however, the electric field is oriented perpendicular to its long axis, so it experiences a TM-like planar mode index. The guided mode can thus be controlled in its size and shape by simply adjusting the relative dimensions of the slab and the post, which in turn changes the planar mode index contrast. For example, for a *T*-Guide operating at λ = 3.6 μm with a slab thickness, t, of 1.4 μm, we consider the effect of changing the post width, w, from 1.2 to 1.9 μm. The respective mode intensity profiles are provided in Fig. 4.2, while the effective index contrast between the slab and post modes is plotted versus the overlap of the optical mode in the post region in Fig. 4.3.

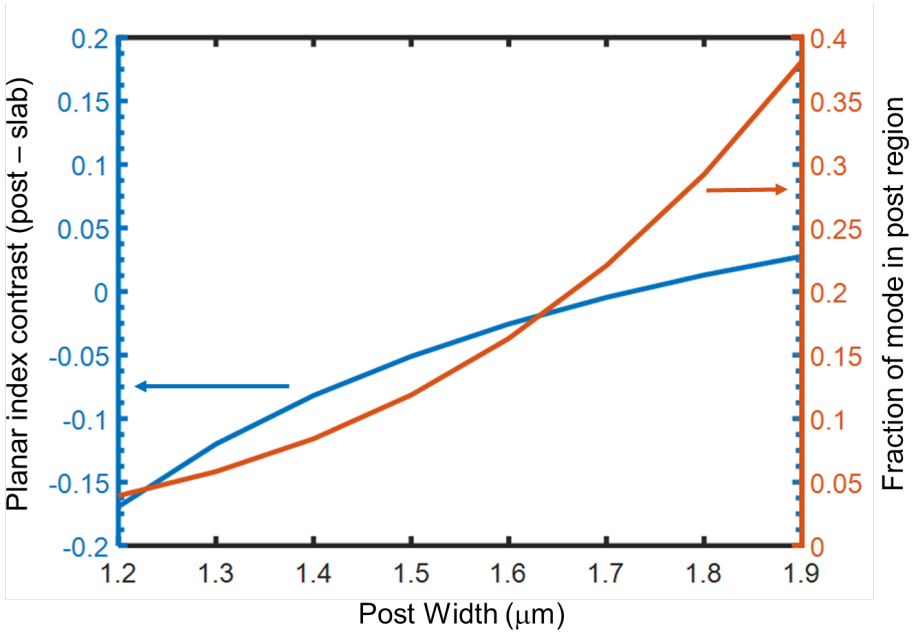

Figure 4.3: Effect of increasing the post width on the position of the optical mode. A wider post increases the TM-like planar mode index in the post region, which increases the index contrast (left axis), resulting in a higher fraction of optical power in the post (right axis).

For the smaller w, the mode resides largely in the slab. But it can be seen that once the planar mode index of the post overtakes that of the slab (positive index contrast in Fig. 4.3), there is a rapid change in the mode distribution toward the post side. This provides a means of controlling the size and position of the optical mode in T-Guides. For instance, a narrow post width can be used to obtain wider modes necessary for efficient input and output coupling, or passive structures such as splitters and directional couplers. Reasonably compact waveguide bends can also be achieved with T-Guides; for example, an Si T-Guide with w = 800 nm and t = 500 nm operating at λ = 3.6 μm experiences a critical bend radius of 190 μm, as determined through axially-symmetric eigenmode simulations. Since these waveguides are inherently single-mode, bends will never cause light to be lost to higher-order modes as would be the case in many conventional waveguide designs.

4.2.2 SMSP properties

4.2.2.1 Silicon T-Guides

In addition to their single-transverse-mode properties, *T*-Guides also exhibit single-polarization guidance over extremely broad bandwidths, and they can do so while operating in a well-confined state, far from cutoff. The broken symmetry of the structure in the vertical direction results in a rapid cutoff only for the vertically polarized, TM-like mode. To investigate this, a series of simulations were performed on various silicon *T*-Guide structures with air cladding on all sides. A simulated structure having a membrane width of 10 μm on either side, a trench depth of 4 μm, and a slab thickness t = 500 nm was employed. COMSOL was used to examine any guided modes as the post width, w, was varied in several steps from 300 to 800 nm.

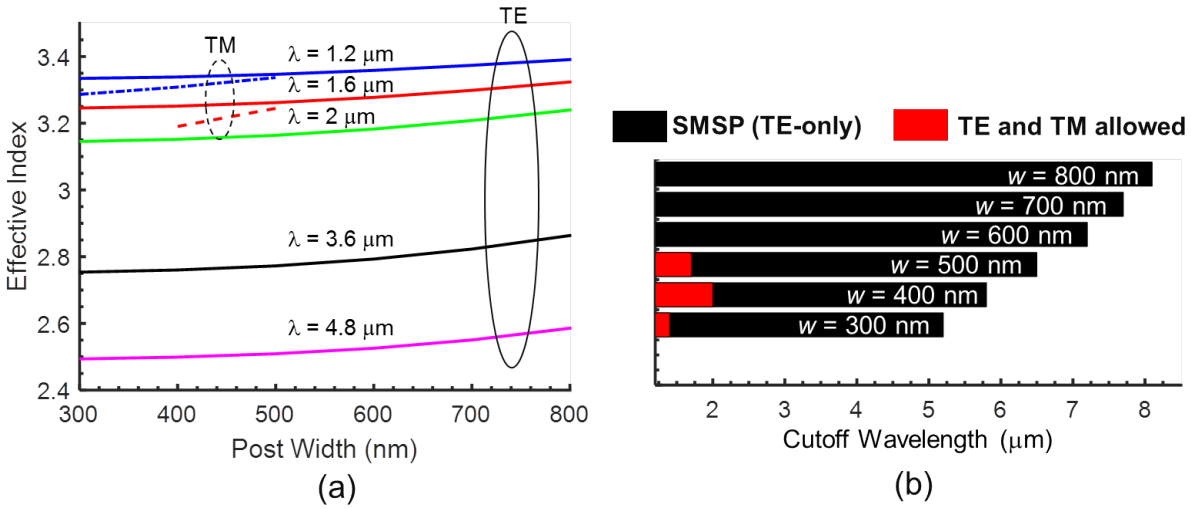

Figure 4.4: Post width vs. effective index for various wavelengths. TM modes are plotted as dashed lines and TE as solid lines; (b) Guided mode transmission windows corresponding to several post widths, spanning from 1.2 μm up to the 10 dB/cm leakage loss cutoff for each case.

Scattering boundary conditions and a leakage loss threshold of 10 dB/cm were assumed to define

the cutoff condition for modes. This value is reasonable, as it is generally chosen to correspond to the relevant length-scale of the platform (e.g., 30 dB/m for the rejected polarization in the case of [63]). The modal effective indices for different post widths are plotted in Fig. 4.4(a), along with the corresponding windows of operation defined by the cutoff condition in Fig. 4.4(b). No higher-order modes were present for any design at any of the simulated wavelengths of 1.2 to 8.5 μm, confirming the single-transverse-mode property of these structures. It can be seen that the TM modes are guided only over a very narrow bandwidth in the near-infrared, in the cases of w = 300, 400 and 500 nm. Their transmission windows vary non-monotonically with post width due to different coupling to the slab. However, they completely vanish for w $=$ 600 nm, and in the case of w = 800 nm, pure TE-mode operation is enabled in the λ = 1.2 - 8.1 μm range, which is nearly the entire transmission window of silicon. This represents an SMSP window of 2.75 octaves, a record span for both integrated and fiber-based devices. Notably, this is achieved without any complicated microstructured patterns typical of SMSP fibers. *T*-Guides are thus a promising geometry for SMSP Si waveguides, which could have applications in high-quality on-chip lasers using Raman or Kerr nonlinearities in the mid-IR [77, 78].

4.2.2.2 Silica T-Guides

Next, the same simulation method is applied to the case of silica *T*-Guides, which are more useful in broadband SMSP characterization in practice. The simulated structure in this case used a membrane width, M, of 5 μm, a slab thickness of t = 350 nm, a post height, P, of 2.5 μm, and post widths, w, varying from 250 to 450 nm. The geometrical definitions of these parameters are provided in Fig. 4.8(b). The effective index for transverse magnetic (TM) and TE modes are plotted for varying post widths in Fig. 4.5(a), and the corresponding window of operation for the mode for each post width and polarization is shown in Fig. 4.5(b). The observed results are similar to those observed in the theoretical investigations of silicon *T*-Guides, where both polarizations are

guided only at short wavelengths, and increasing the post width beyond the slab thickness results in broader SMSP windows. This occurs because the TM mode begins to leak to the substrate through the post as it is widened. In Fig. 4.5(a), this is reflected by the disappearance of the dashed lines corresponding to the TM modes, above a minimum post width. An SMSP window from 260 to 1600 nm (2.6 octaves) is possible for a post width of 450 nm with silica *T*-Guides, but smaller post widths also produce extremely broad SMSP operation.

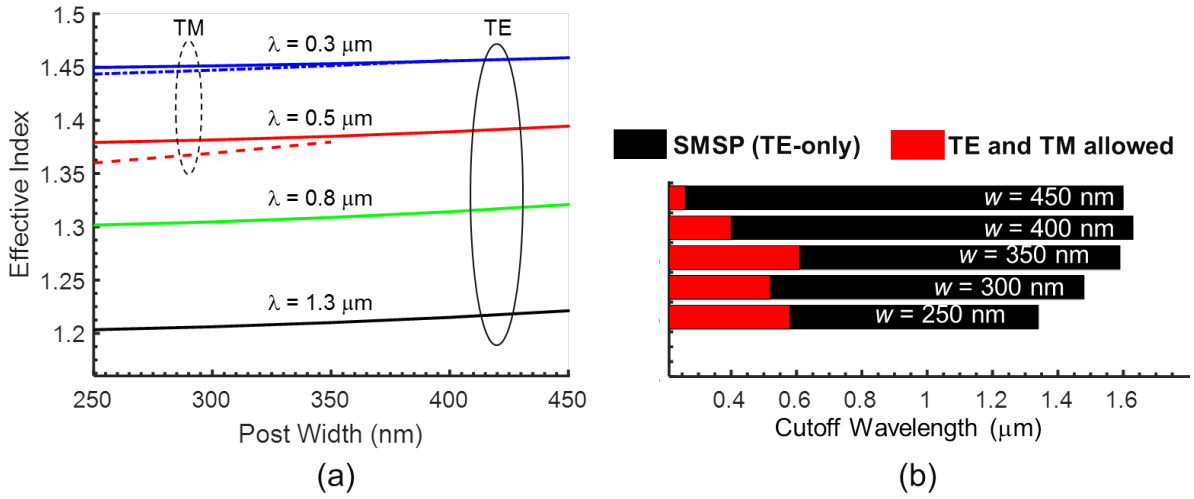

Figure 4.5: *T*-Guide post width vs. modal effective index for different wavelengths (slab thickness fixed at 350 nm). Dashed lines are TM modes and solid lines are TE modes; (b) Transmission windows (defined by ¿ 10 dB/cm loss threshold) for the TE and TM guided modes, with black corresponding to SMSP operation and red to bi-polarized operation.

4.2.3 Dispersion engineering

The unique geometry of *T*-Guides also presents new opportunities for waveguide dispersion engineering, which is of importance to phase-sensitive nonlinear optical processes, such as four-wave mixing and supercontinuum generation. For *T*-Guides, dispersion engineering can be achieved by

adjusting the overall size of the structure, as well as the relative width of the post and the thickness of the slab. Dispersion designs for silicon T-Guides are considered in Fig. 4.6, with sub-μm (i) and μm-sized (ii) geometries (see caption), showing the total group velocity dispersion (GVD) of each. Both designs show broad regions of small anomalous GVD, with varied zero-GVD wavelengths. In case (i), the anomalous-GVD region spans from wavelengths of 2.3 to 3.6 μm. In case (ii), it extends much further, from 2.9 to 7.8 μm. These results show promise for nonlinear integrated photonics with T-Guides, benefiting from their smooth dispersion profile and wideband SMSP operation.

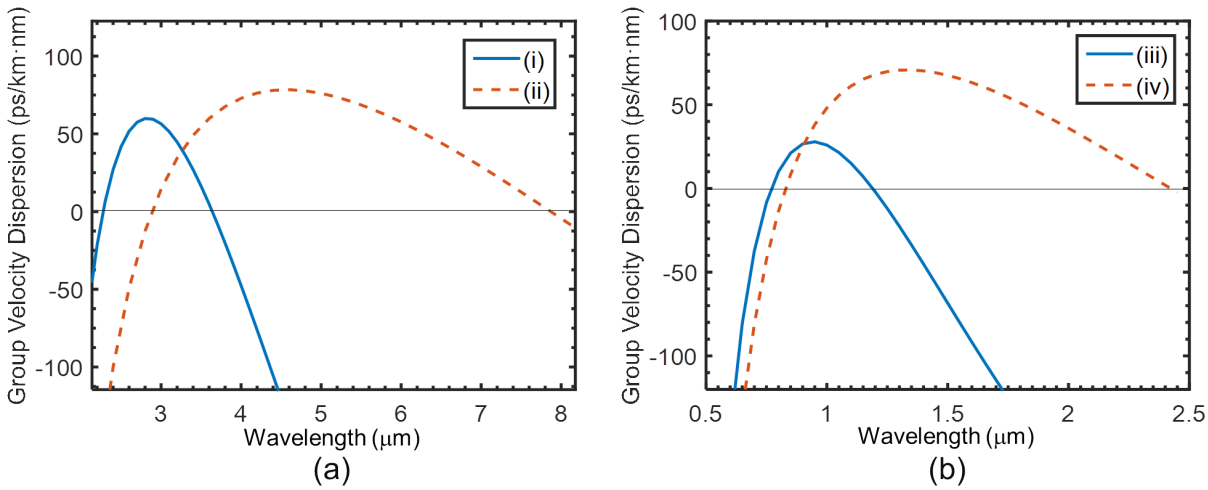

Figure 4.6: Simulated total GVD of various silicon T-Guide designs: (i) w = 0.85 μm, t = 0.64 μm, and (ii) w = 1.6 μm, t = 1.4 μm.

4.3 Fabrication and measurements

4.3.1 Silicon T-Guides

Achieving low propagation losses is a critical requirement for any high-performance integrated photonic platform. To demonstrate this, silicon T-Guides were fabricated using wafer-bonding techniques. The slab layer was transferred from donor dies of the silicon-on-insulator (SOI) type, with a device layer thickness of 1300 nm. More details on the fabrication can be found elsewhere in Appendix A.3. Straight waveguides up to 5 cm long were fabricated. An SEM of a waveguide cross section is provided in Fig. 4.7(a).

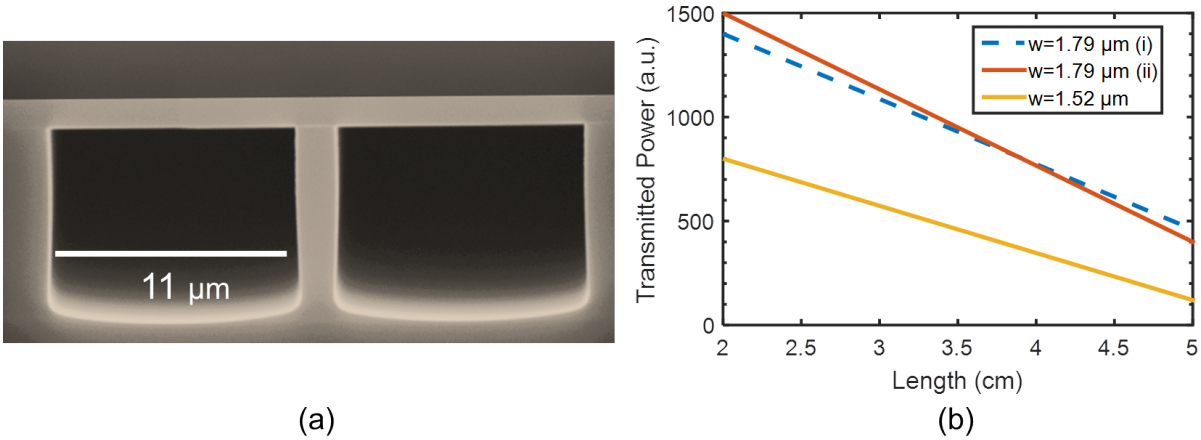

Figure 4.7: (a) SEM cross section of a fabricated Si T-Guide; (b) Cut-back measurements of two different post widths for lengths of 5 and 2 cm.

A polarized optical parametric oscillator operating at 3.64 μm was used as the source for cut-back loss measurements, obtaining TE-mode losses of 1.75 $\pm$ 0.3 dB/cm and 2.7 $\pm$ 0.5 dB/cm for 1.79 and 1.52 μm post widths, respectively (Fig. 4.7(b)). The higher loss for the shorter post width could have resulted from variable leakage due to the large thickness variation of $\pm$ 300 nm

in the slab (from the SOI wafer manufacturing method). This shows that high-quality, low-loss waveguides can be readily achieved over a large surface area using the *T*-Guide geometry. At the same wavelength of 3.64 μm, it was confirmed that extremely high losses prohibit propagation of TM input light, evidenced from negligible detected power. This confirms the expected SMSP behavior of the waveguides at this particular wavelength.

4.3.2 Silica T-Guides

For broadband SMSP characterization, however, silicon *T*-Guides may not be an ideal case due to the measurement challenges in the mid-infrared. Silica *T*-Guide counterparts, meanwhile, lend themselves much more easily to SMSP characterization using streak imaging techniques in the visible to the near-infrared range. In this section, we describe the fabrication and characterization of such devices.

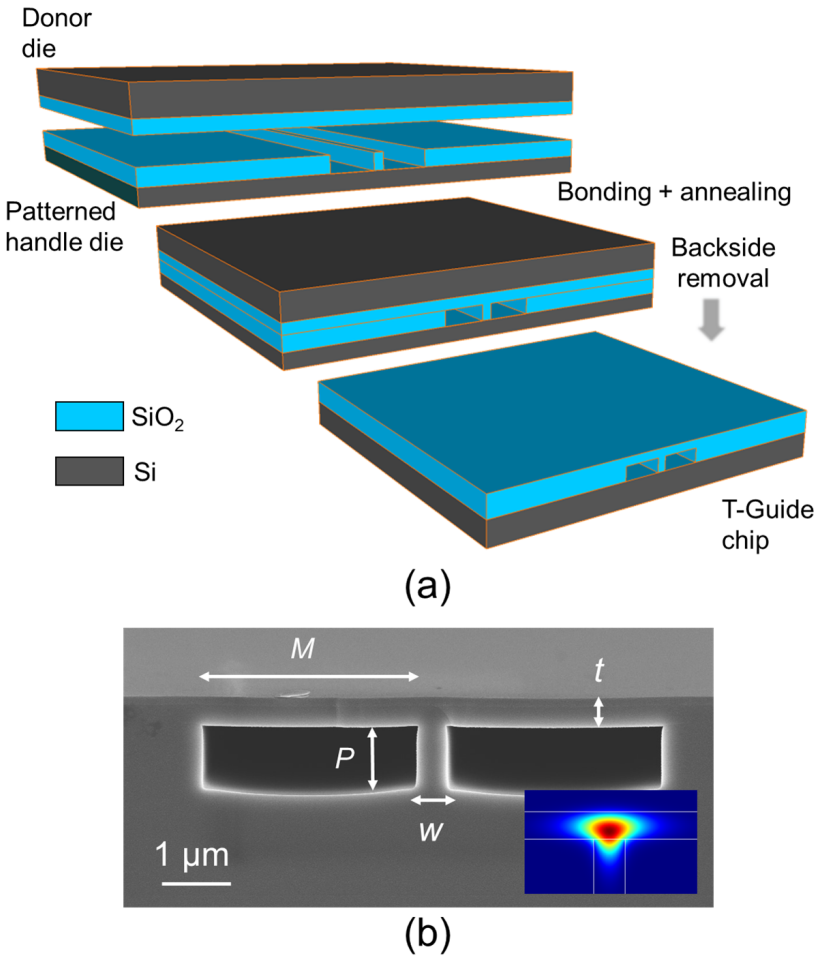

Figure 4.8: Simplified fabrication method for SiO_2 *T*-Guides; (b) SEM cross section of a fabricated silica *T*-Guide on silicon substrates (inset: simulated intensity profile of the mode).

Silica *T*-Guides were fabricated according to the flow in Fig. 4.8(a). A thermally oxidized (2500 nm thick) silicon die was patterned with trenches to form isolated posts between 250 - 400 nm wide. It was contacted and spontaneously bonded with a thermally oxidized (300 nm thick) piece of silicon (the donor die) approximately 3 x 5 cm^2. After annealing, the backside was removed with dry etching and wet etching techniques. More details are available in Appendices A.2-A.3.

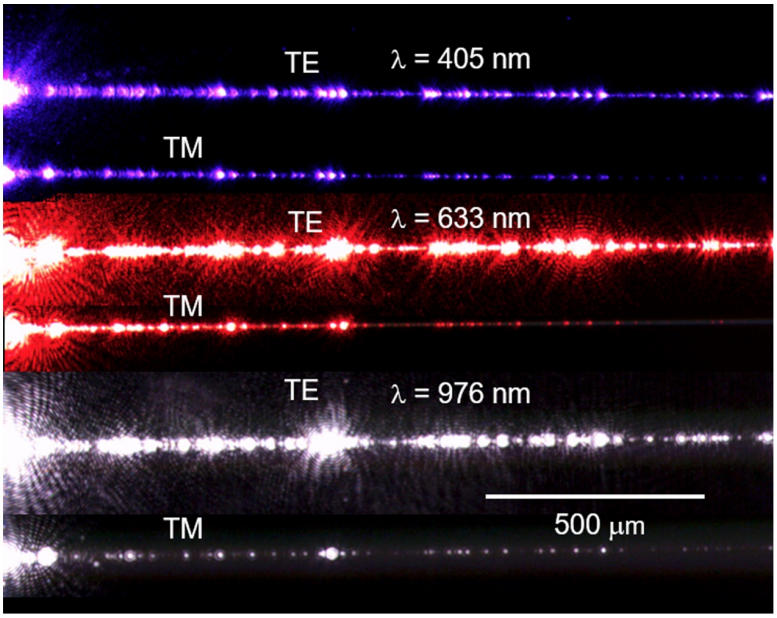

(a)

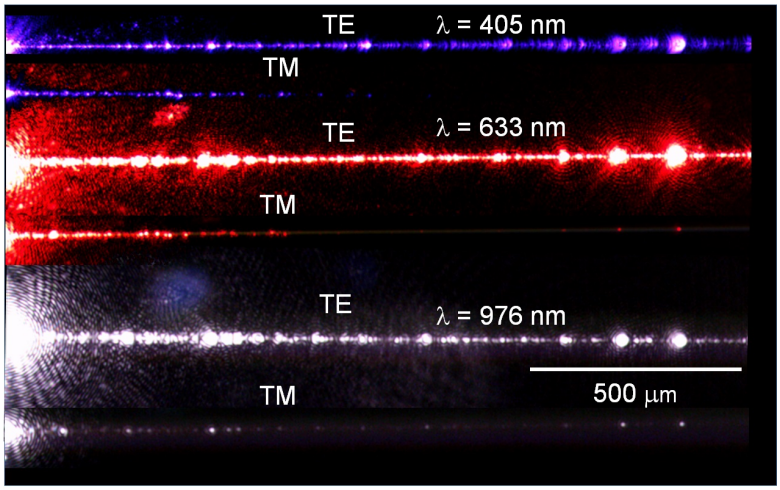

(b)

Figure 4.9: Streak images of *T*-Guides: (a) w = 250 nm; (b) w = 300 nm. Single-polarization operation is observed by the much longer length of TE-mode streaks compared to those of the TM-mode.

Cleaved waveguides were characterized to assess their SMSP window. Three different lasers were utilized: blue (diode, 405 nm), red (helium neon, 633 nm) and near-infrared (diode, 976 nm). Light was coupled into the *T*-Guides through an aspheric lens, and a top-view of scattered light from the waveguides was imaged onto a silicon camera module with 2048 x 1536 resolution through a microscope with 4.5x magnification (the infrared blocking filter was removed to permit infrared measurements). A linear polarizer was placed in front of each laser to image the TE and TM mode streaks separately for comparison. The corresponding streak images for *T*-Guides with widths of 250 and 300 nm are collected and shown in Figs. 4.9(a-b). The case of w = 300 nm showed stronger attenuation for the TM polarization, a result consistent with the expected behavior of TM light leaking to the substrate through the wider post. It can be seen that for all wavelengths and for both widths, the TM mode is severely attenuated compared to the TE mode, as evidenced by the short length of the streak. Fitting the measured intensity along the streak to an exponential decay function, the propagation loss was examined for w = 250, 300 and 350 nm. The length was accurately calibrated by using the known spacing between adjacent waveguides. A high degree of particle scattering was observed during the measurements, evidenced by the bright dots in Figs. 4.9(a-b). It results from particles trapped in between the slab and the handle wafer during bonding. Inspection of the waveguides under higher magnification confirmed this issue. This discrete scattering (as opposed to the more continuous scattering observed due to nanoscale roughness in waveguide features) thus obscured most measurements of the TE mode propagation loss. Nevertheless, two TE mode loss cases could be accurately analyzed despite the scattering: w = 300 nm at λ = 405 nm with 12 $\pm$ 4 dB/cm, and w = 250 nm at λ = 976 nm with 19 $\pm$ 3 dB/cm. Next, the TM mode propagation losses (the rejected polarization) were examined at λ = 405 nm; the corresponding TM mode propagation losses for w = 250, 300 and 350 nm were 49, 101 and 387 dB/cm, respectively. For λ = 633 nm, the TM losses were 116, 181 and 234 dB/cm. The propagation loss for the TM mode at λ = 976 nm was too large to measure accurately; however, since the largest measurable loss in this experiment was 387 dB/cm, the attenuation is expected to be

even greater. The uncertainty in all TM loss measurements is estimated to be ± 15%. All loss uncertainties were obtained after repeated curve fittings of similar streak sections. The earlier onset of single-polarization operation at shorter wavelengths here than that predicted by simulations can be explained by the slightly rounded top corners of the fabricated post (Fig. 4.8(b)), which significantly increase the rate of leakage through the post for the TM mode.

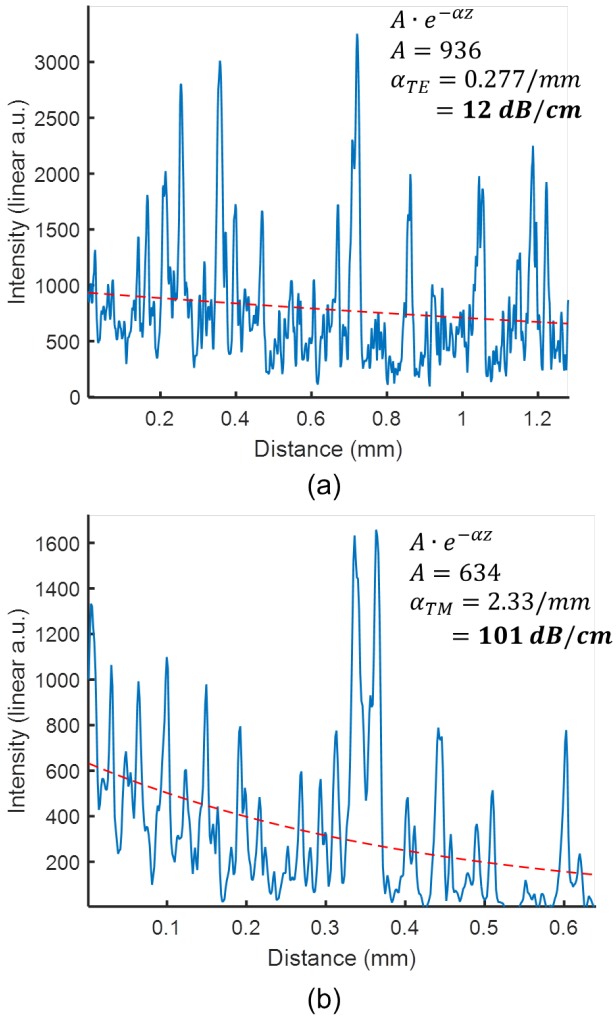

Figure 4.10: Measured (solid) and fitted (dashed) intensity of scattered light for w = 300 nm at λ = 405 nm for (a) TE and (b) TM modes.

The intensity streaks in the case of λ = 405 nm and w = 300 are plotted in Fig. 4.10(a-b) for the TE and TM modes, showing the form of the fitted function and the curve fitting parameters. With vendor-supplied thermal oxide donor wafers (instead of in-house grown films which accumulated particles during oxidation), the loss can be greatly reduced in the future by reducing the density of these defects. Future work may also include mode-field adapters to improve the coupling efficiency on and off-chip; these may be implemented by the narrowing of the *T*-Guide post width near the facet to convert the mode to a more Gaussian-like profile.

It should be noted that the modal cutoff condition of 10 dB/cm propagation loss used in the simulations cannot be straightforwardly applied to these measurements, since the performance of scattering boundary conditions is inherently different from substrate leakage. Regardless, it is clear from the streak measurements that extremely high attenuation values are achieved for the TM mode in comparison to those of the TE mode, thus demonstrating strong single-polarization operation over a span of more than 1.27 octaves (405 to 976 nm) in the case of w = 300 nm, limited by the lasers available for the measurement and the cameras spectral sensitivity. A maximum polarization-dependent loss (PDL) of 89 $\pm$ 19 dB/cm was observed in the case of λ = 405 nm for w = 300 nm (based on 12 dB/cm loss for the TE mode and 101 dB/cm loss for the TM mode). The 1.27-octave SMSP window is significantly higher than the previous record of 0.23 octaves in optical fibers [65].

Although the single-mode behavior of *T*-Guides is derived from the same well-understood mechanism as for shallowly etched ridge waveguides [69], it is nevertheless desirable to provide an experimental confirmation of this. To this end, the tightly focused input beam at 633 nm wavelength was scanned both horizontally and vertically across a *T*-Guide facet (with w = 300 nm) while the output mode profile was imaged with a camera (Fig. 4.11). The existence of higher-order modes would be evidenced by a change in the spatial distribution of the intensity during the scan. However, the mode retains its shape and only changes in absolute intensity, confirming that only one transverse mode is permitted in the *T*-Guides.

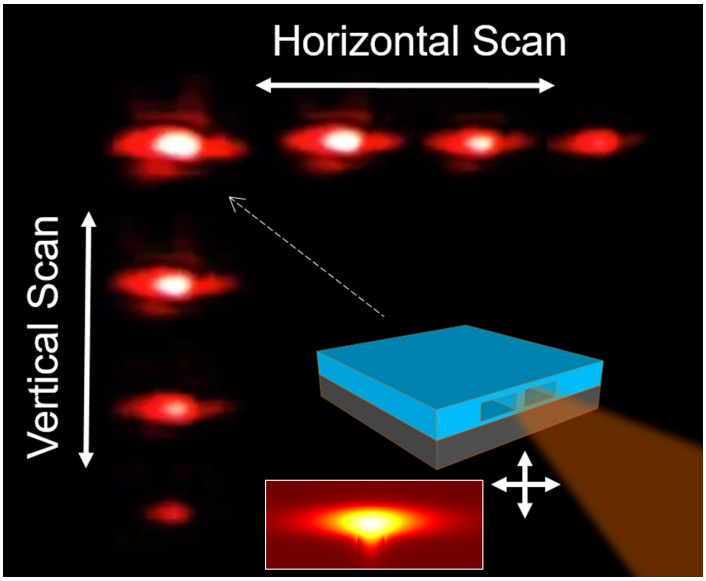

Figure 4.11: Images of the optical mode collected from a T-Guide during horizontal and vertical misalignment of the focused input beam onto the facet. The faint lines above and below the mode are a result of aberrations in the imaging optics used. Inset: simulated intensity profile of the mode.

4.4 Conclusion

In conclusion, anchored-membrane waveguides, or T-Guides, have been numerically and experimentally investigated as an integrated photonic platform supporting wideband single-mode and single-polarization SMSP operation. Air-clad silicon T-Guides were shown to exhibit SMSP windows of up to 2.75 octaves, a record span in simulations. Furthermore, dispersion engineering of T-Guides designs showed that promising dispersion profiles can be achieved with relatively flat and small anomalous GVD spanning from λ = 2.9 - 7.8 μm. Silicon T-Guides were fabricated and tested at λ = 3.64 μm, showing low propagation losses of 1.75 dB/cm for the TE mode. The superior SMSP bandwidth, smooth dispersion and simple geometry of T-Guides make them ideally suited for nonlinear integrated photonics applications.

CHAPTER 5: TOPOGRAPHICALLY ANISOTROPIC PHOTONICS

5.1 Introduction

There is a growing need for high-performance polarization-selective devices for integrated photonic systems, spurred on by the development of broadband polarization-division-multiplexed communication systems. Typical components for this purpose include TE- and TM-pass polarizers, polarization beam-splitters (PBS) or polarization-splitter-rotators (PSR).

Polarization-sensitive integrated photonics has applications beyond the telecommunications sector as well. Remote spectroscopy is a metrology technique applicable to many fields of study, such as environmental monitoring, satellite reconnaissance and planetary science. Images are collected which usually contain two dimensional intensity data, as well as some degree of spectral discrimination which helps to properly identify the composition of objects present in the scene. The inclusion of polarization data elucidates many details, and the combined study of spectral and polarimetric information in a scene is referred to as spectropolarimetric imaging [79]. Polarimetric lidar, leveraging dual lasers at 532 and 1064 nm wavelengths, has been used in the study of the vegetation canopy, the structure of which has significant implications in the study of microclimates as well as large-scale climate change [80]. In atmospheric studies, optical polarimetry allows the precise determination of the phase state of clouds due to the polarization-dependent scattering of water crystals; the POLDER spaceborne instrument successfully conducted such measurements over a spectral bands from 443 to 865 nm [81].

Currently, remote sensing systems such as those described previously rely on bulk or free-space optics as the platform of integration. This leads to poor environmental stability and large size-weight and power requirements. Integrated photonic technology provides a means of drastically

reducing these requirements and additionally driving down the cost to produce the overall system. For these reasons, the use of integrated photonics is already planned into upcoming technology for space exploration, such as NASAs ILLUMA laser modem [82].

However, to implement an integrated polarimetric remote sensing system, several key functions and performance requirements must be met. It must be capable of first separating the TE and TM signals. Additionally, it must achieve this over a broad bandwidth, typically on the order of an octave in fractional bandwidth [80, 81]. Finally, it must do so without incurring excess insertion losses, which would degrade the sensitivity of the overall system. After splitting (either in a PSR or PBS), the light in each path usually passes through an in-line polarizer to remove residual cross-polarized light. After this point, the purely polarized light in each channel is passed into whatever devices are required on the chip. The performance of several state-of-the-art, experimentally demonstrated polarization-selective integrated devices is summarized in Table 5.1.

Table 5.1: State-of-the-art integrated polarization-selective devices

Work	Device	Bandwidth (nm)	Insertion Loss (dB)	Min. ER (dB)
Dai *et* al. [83]	PSR	87	1.5	15
Kim *et* al. [84]	PBS	100	2.1	22.5
Su *et* al. [85]	PBS	150	3.4	10
Xiong *et* al. [86]	TE-pass polarizer	110	0.4	30
Shahin *et* al. [87]	TM-pass polarizer	110	2.3	18

All such devices take advantage of the dissimilar electric field distribution inherent to the TE and TM modes of the waveguides involved. Consequently, their cross-sections are specifically engineered to enhance this effect. A stronger differentiation between polarizations can be obtained by utilizing sub-wavelength structures (as in ref. [86, 87]) or tightly confined modes with significant field penetration outside the core. It is clear that while acceptable insertion losses have been achieved using this general approach, the bandwidth falls far short of the requirements for remote

sensing. The limitation in bandwidth essentially arises from the wavelength dependence of the field distribution, which results in rapid changes close to cut-off, particularly in the case of TM modes in 220 nm-thin silicon. Additionally, going to shorter wavelengths, the TE and TM mode fields become more similar in their distribution as they reach greater confinement, which leads to reduced differentiation in polarization-selective devices.

It is apparent that these approaches, developed with telecommunications bandwidth requirements in mind, are not suitable for wideband remote sensing applications. Some other method is required, particularly one that uses an effect that is not strongly wavelength dependent. At this point, we turn to the idea of manipulating the anisotropy of the optical material itself, rather than manipulating its modal birefringence. Consider a waveguide with a core consisting of some uniaxial anisotropic material with the extraordinary axis pointing in the vertical direction (perpendicular to the plane of the substrate). The TE and TM modes of this waveguide experience a birefringence which is enhanced if the extraordinary index is lower than the ordinary index. Importantly, this birefringence remains even as the wavelength becomes shorter and the mode is strongly confined, in contrast to the behavior of isotropic-core waveguides where they become less birefringent. However, making waveguides solely out of this anisotropic material does not directly enable broadband, polarization-selective devices, since the birefringence cannot be controlled or varied to any end. If instead the anisotropy could be adjusted spatially across the chip, or simply turned off in some waveguides and not in others, it could then be leveraged. This concept was first achieved through the selective disordering of quantum wells to tune the anisotropy in semiconductor waveguides [88, 89]. By controlling the spatial distribution of material anisotropy on the chip, one can design devices that exploit transitions between different materials. This was later used to demonstrate a PBS [90]. The variable anisotropy concept has also been explored by a limited number of other groups using various approaches such as polymers [91, 92] and organic crystals [93]. No broadband polarization-selective devices have been achieved with these approaches, which suffer from

poor compactness, fabrication complexities or limited environmental stability due to the choice of materials.

These spatially-engineered anisotropic surfaces provide a means to achieve integrated polarization-selective devices which minimal wavelength sensitivity. But an approach is needed which puts this technology in line with the compactness, performance and robustness achieved by high-contrast photonic platforms. The requirements are summarized as follows:

-Built from durable, stable materials

-Deposition methods compatible with conventional photonics fabrication techniques

-The ability to co-integrate both anisotropic and isotropic films to achieve maximal contrast

-High-contrast waveguides with exhibit purely symmetric cross sections

The last requirement is subtle but still crucial, as it avoids the transition to cut-off that would be inevitable for any asymmetric waveguide geometry; this is a limitation for all of the prior methods for engineered anisotropy. We propose a novel approach called *Topographically Anisotropic Photonics* (TAP) to achieving all these requirements by employing a combination of the photonic damascene process [94] with precisely engineered dielectric film stacks. The material anisotropy is derived from a multilayer stack (MLS) consisting of alternating layers (deep-sub-wavelength thickness, $t_{L,H}$) of silicon dioxide (L, low index) and silicon nitride (H, high index), exhibiting form-birefringence in the refractive index as described below by effective medium theory:

$$n_{eff,TE}^2 = f n_H^2 + (1-f) n_L^2 \tag{5.1}$$

$$1/n_{eff,TM}^2 = f/n_H^2 + (1-f)/n_L^2 \tag{5.2}$$

$$t_{H,L} \ll \lambda_H \tag{5.3}$$

where n is the refractive index, and f is the fill fraction of the silicon nitride material (high-index) in the MLS. This is a valid approximation when the thickness of the layers is much smaller than the wavelength of light inside the medium of high index (Eq. 5.3). Birefringence is observed in the material refractive index due to the different behavior of TE and TM waves. Consider a waveguide (Fig. 5.1) with a silicon oxynitride (SiON) core and an MLS cladding with refractive indices as indicated in the figure satisfying the following conditions:

$$n_{core} > n_{eff,TM} \tag{5.4}$$

$$n_{core} < n_{eff,TE} \tag{5.5}$$

$$n_{clad} < n_{core} \tag{5.6}$$

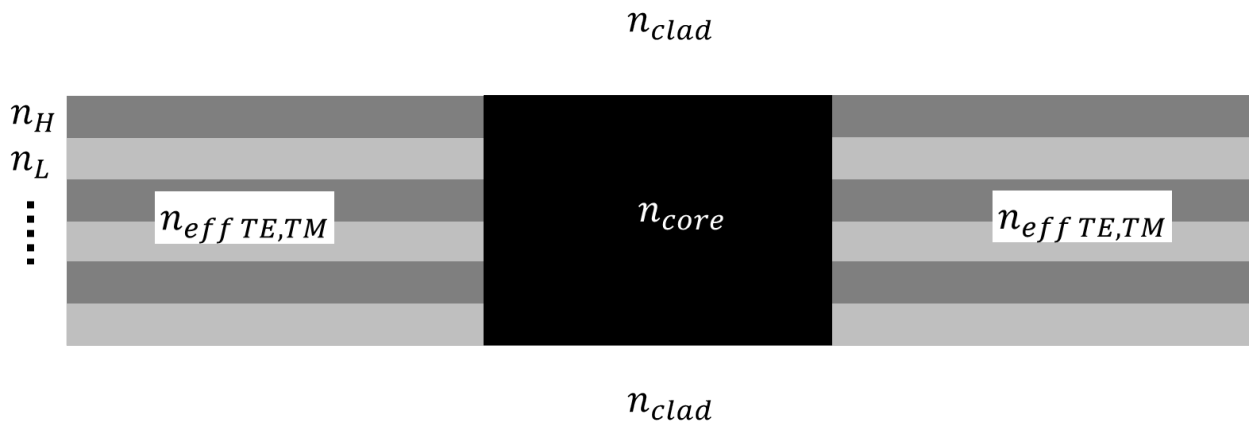

Figure 5.1: Single-polarization waveguide state employing an anisotropic cladding and an isotropic core.

If the MLS cladding material is constructed such that $n_{eff,TE}$ and $n_{eff,TM}$ satisfy Eq. 5.4 and 5.5 through Eqs. 5.1 and 5.2, the waveguide displays intrinsic single-polarization behavior, in that TE-polarized light will become anti-guided due to the negative index contrast, and TM-polarized light will be guided normally. Similarly, if the core and cladding materials are simply swapped in place such that the core is MLS and the cladding is the isotropic material with n_{core}, the waveguide will only guide TE polarized light. An optical micrograph of the cross-section of such a waveguide is provided in Fig. 5.2.

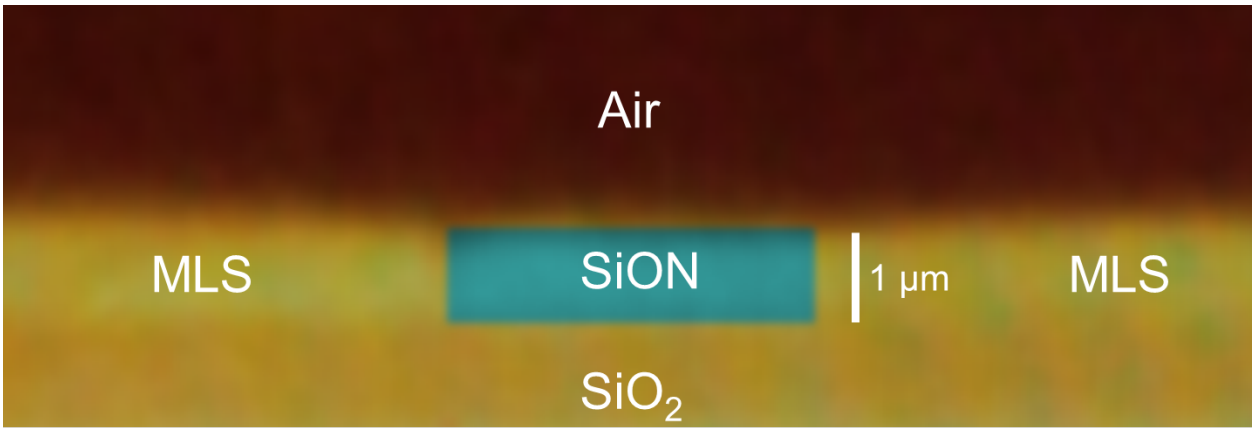

Figure 5.2: Optical micrograph of an *M*-type TAP waveguide cross-section with false coloration of the SiON core to highlight its dimensions .

The proposed approach indeed allows both of these arrangements, and more, to be achieved in the same process. This is realized in the following manner. The MLS is first deposited on an oxidized silicon substrate. Next, the anisotropy is ”mapped” on the surface by etching the MLS in some areas and then filling it with SiON or SiO_2 as core or cladding materials. Etch-back techniques are used to restore surface flatness after the etching and re-fill deposition steps. A complete description of the fabrication technique is provided in the appendices. A variety of unique waveguiding ”states” may be realized with TAP, which are summarized in Fig. 5.3.

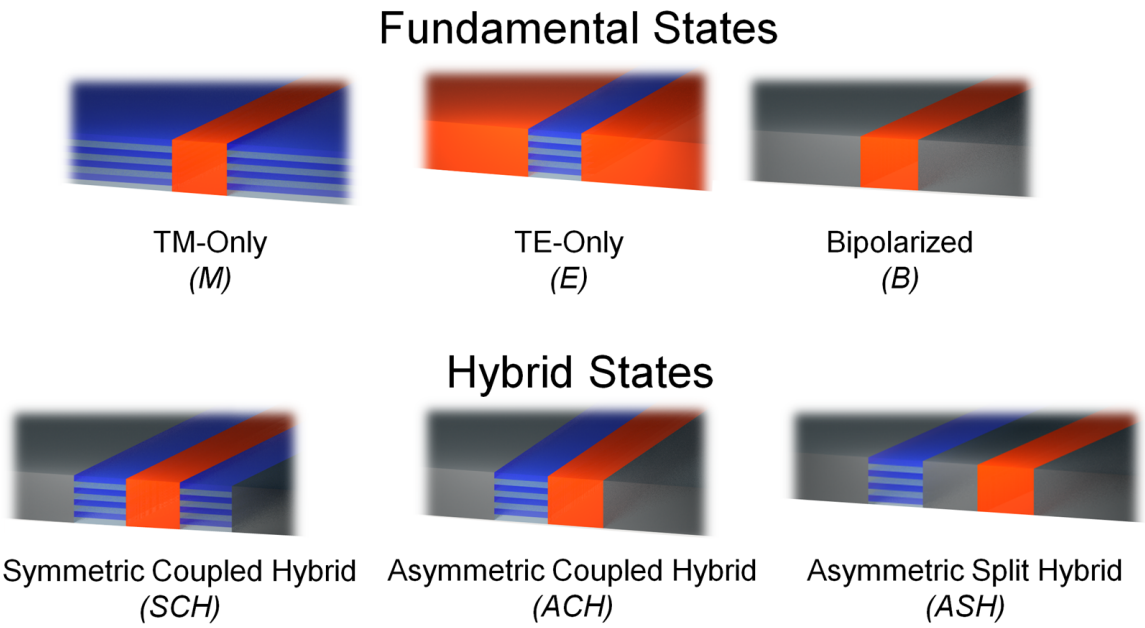

Figure 5.3: Schematic view of the fundamental and hybrid states possible with *topographically anisotropic photonics*.

The states are divided into *fundamental* and *hybrid* types. The fundamental states include TE-only (E), TM-only (B) and bipolarized (B). They consist of one core material with symmetric claddings of another material. The hybrid states, which each use two different core materials, include the symmetric coupled hybrid (SCH), asymmetric coupled hybrid (ACH) and asymmetric split hybrid (ASH). In each fundamental and hybrid state, a different relation exists between the TE and TM modes. For example, in the *ACH* hybrid state, the TE mode is concentrated in the MLS core due to the higher refractive index, whereas the TM mode is concentrated in the SiON core due to the low refractive index it experiences in the MLS (Fig. 5.4). Importantly, the polarization-selective behavior of the hybrid states is robust to many factors, including confinement factor, waveguide geometry tolerances, and even some degree of variability in the refractive indices.

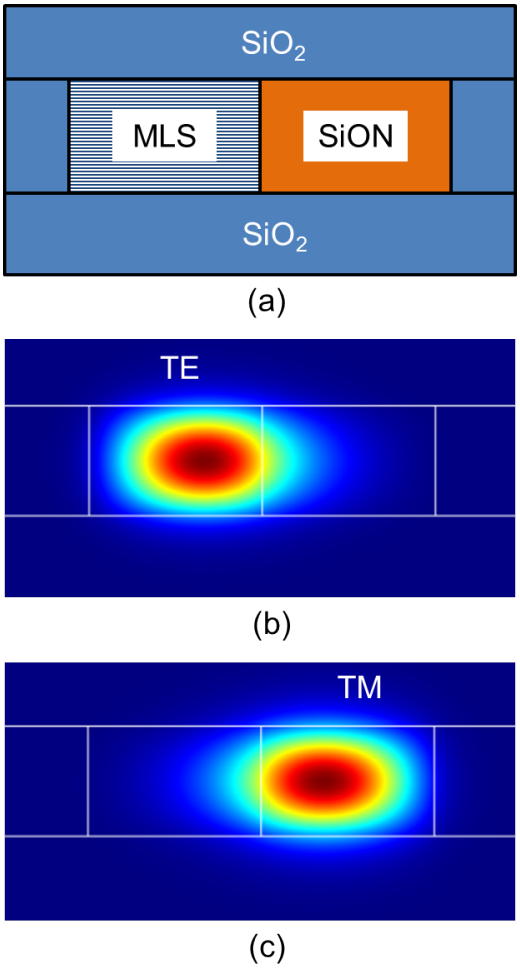

Figure 5.4: *ACH* hybrid waveguide state showing (a) the cross-sectional geometry, (b) TE-mode intensity profile, and (c) TM-mode intensity profile.

5.2 Design and simulation

Now, we consider how to apply TAP to the goal of achieving broadband and efficient polarization-selective devices. With TAP, light can start in any one of the fundamental states, generally in *B* for incoming light of an indeterminate polarization. Next, to parse the TE and TM modes, a transition may be made to one or more of the hybrid states, which will result in a new polarization-

mode distribution. Finally, it undergoes a transition back to another fundamental state to resume transmission elsewhere on the chip. As long as these state transitions are performed adiabatically, the performance can be extraordinarily high in terms of bandwidth and efficiency.

In this section, polarization-selective devices such as PBS, polarizers and polarization-cloaked micro-ring resonators (PCMR) are designed and simulated using this simple approach. To support the goal of scalable manufacturing and low process complexity, all designs share several parameters for the materials and films, such as device layer thickness and refractive indices. No special processing steps are required for any particular type of device.

5.2.1 Polarizing beam splitters

As mentioned in the previous section, the design approach for TAP involves selecting a series of waveguiding states and implementing transitions between them. The approach for designing a PBS is now detailed; a schematic of the geometry and the state transitions is provided in Fig. 5.5. It is assumed that the input state is *B*, such that it is bipolarized. Next, a transition is made to the hybrid *ACH* state mentioned earlier (Fig. 5.4), which forces the TE and TM modes into separate core regions. Afterward, a transition is made to the *ASH* state by introducing a ”wedge” of silicon dioxide cladding in between the two cores. The gap between the SiON and MLS cores is gradually widened until they do not interact. Finally, at the output, the MLS core in the TE arm is replaced with SiON (not pictured) to be compatible with the makeup of ordinary bus waveguides on the chip. Thus, the output state is again *B* for both the TE and TM arms, with the two polarization modes efficiently diverted into their respective paths.

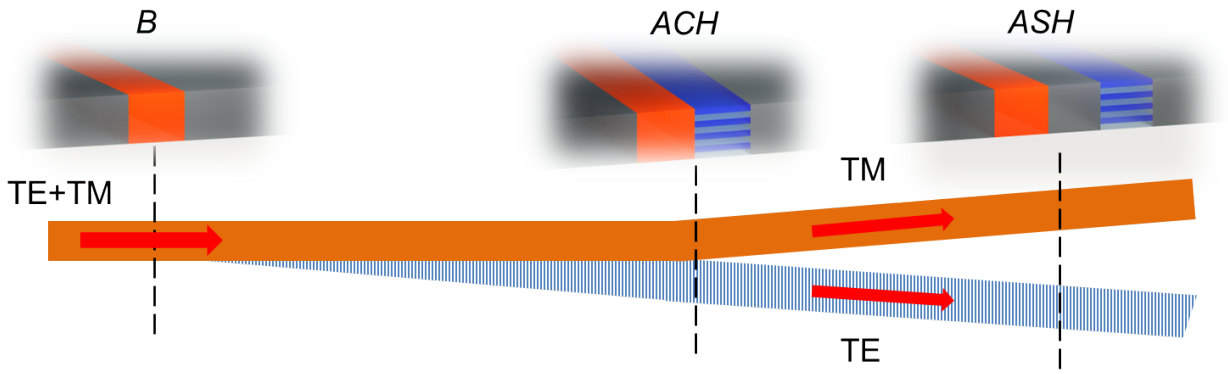

Figure 5.5: Schematic view of the proposed PBS design, showing the geometry and state transitions involved.

Although the conceptual approach to designing a TAP PBS is relatively simple, there are several important considerations with regard to the geometrical parameters. First, the $B - ACH$ transition should be long enough to avoid coupling into higher-order modes in the case of short-wavelength operation. Secondly, the wedge angle should be small enough to avoid scattering from an abrupt change in mode shape in the $ACH - ASH$ transition. Finally, the width of the waveguides in the ACH state should be sufficient to confine the TE and TM modes into separate spaces prior to splitting when operating at short wavelengths. However, it should be noted that in long-wavelength operation, this is not critical, since the TE and TM modes are still able to leak into the desired port even during the initial stage of splitting. This is observed in simulations that follow.

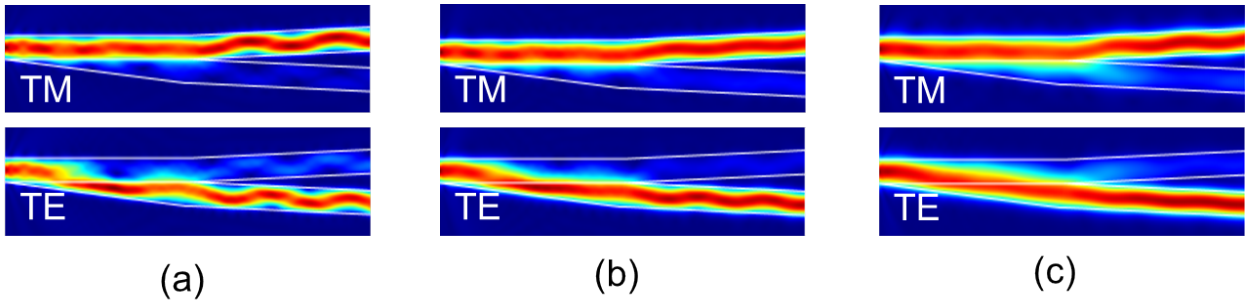

Figure 5.6: Normalized electric field profile from a top-view of the simulated PBS design for (a) λ = 633 nm, (b) λ = 850 nm, (c) λ = 1110 nm. Top: TM input light; Bottom: TE input light.

The proposed PBS design was simulated in COMSOL^{TM}using a 2D approximation, incorporating the slab effective indices for the different materials. The $B-ACH$ transition length was 40 μm, the full wedge angle for the $ACH-ASH$ transition was 1.4 degrees, and the maximum width of the SiON and MLS cores was 1.4 μm each. Simulations were conducted by injecting TE or TM light into the B-type input port and monitoring the extinction ratio and insertion loss at the TE and TM output ports. Based on light sources available for experiments, the performance was examined at λ = 633 nm, 850 nm, and 1110 nm. The normalized electric field plots are shown in Fig. 5.6 for all cases, and the performance is summarized in Table 5.2.

Table 5.2: Simulated PBS performance

Wavelength, nm	Ins. Loss (TE), dB	Ins. Loss (TM), dB	ER (TE), dB	ER (TM), dB
633	0.26	0.03	12.7	21.4
850	0.04	0.13	19.3	17.0
1110	0.10	0.20	16.4	13.8

Across the span from λ = 633 - 1110 nm, it can be seen that the insertion losses remain below 0.3 dB and the extinction ratio is always greater than 12 dB. Some multimode oscillation is visible on the output ports at shorter wavelengths, though this may be readily addressed in the future

by implementing more refined splitter geometries incorporating curved y-junctions and parabolic widening profiles. However, it is quite remarkable that the design continues to work with high splitting efficiency even in the highly multimode regime at $\lambda = 633$ nm. This would not be possible for conventional PBS designs that rely on precise mode shape engineering with purely isotropic materials. This behavior could be highly useful for receiver chips where higher power collection efficiency is desirable and multimode operation is tolerable.

5.2.2 Polarizers

Next, we consider the design of TAP polarizer devices. Given the availability of single-polarization waveguide states such as *E* and *M* in this technology, it is straightfoward to imagine how this can be implemented. The particular case of a TM-pass polarizer will be addressed here, although a TE-pass polarizer can in principle be achieved in an almost identical fashion.

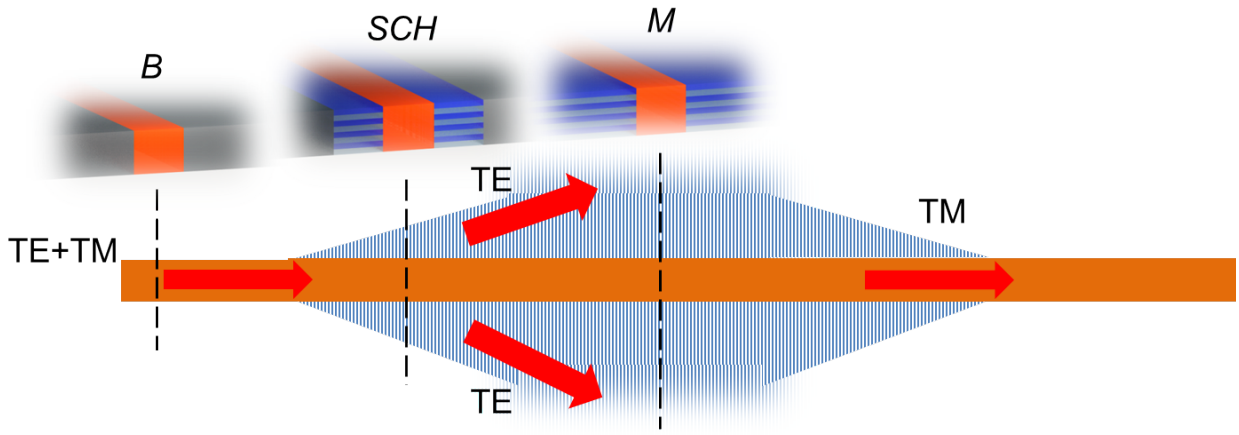

Figure 5.7: Schematic view of the proposed TM-pass polarizer design.

Again, the initial state for the input is a *B*-type waveguide with an indeterminate polarization state for the light. To begin the transition to a single-polarization waveguide, it first is gradually

converted to the *SCH* state where the TE light is pulled into the MLS cores adjacent to the middle SiON core. Then, the SiO_2 cladding is tapered down in width until the SiON core is surrounded only by MLS on either side, making it an *M*-type waveguide. Since the TE light is no longer guided, it leaks out into the surrounding environment. Once it is sufficiently radiated away from the core, a reciprocal transformation takes place back to the original *B* state. A schematic of this polarizer design is shown in Fig. 5.7.

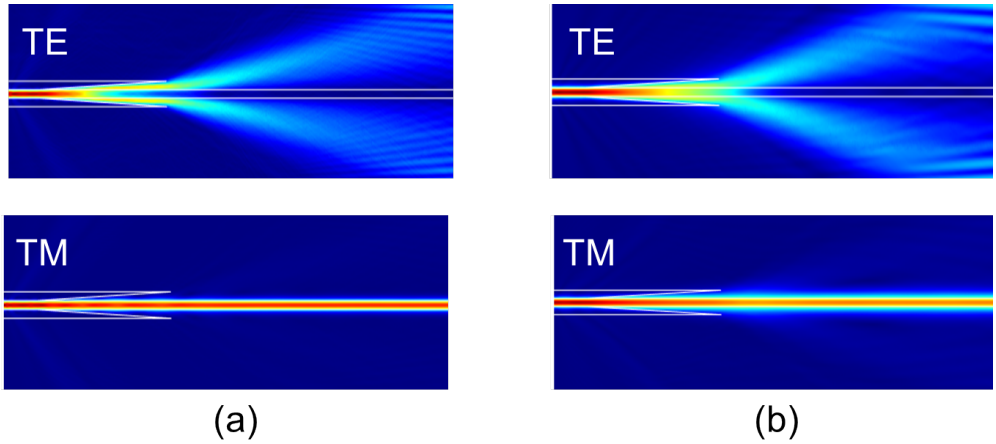

Figure 5.8: Normalized electric field profile from a top-view of the simulated TM-pass polarizer design for (a) λ = 633 nm and (b) λ = 1110 nm. Top: TE input light; Bottom: TM input light.

Table 5.3: Simulated TM-pass polarizer performance

Wavelength, nm	Ins. Loss, dB	ER, dB
633	0.04	21.1
1110	0.19	22.7

Using the same approach as for the PBS, a polarizer of this type was simulated. The core waveguide width was 1.2 μm, the $B - SCH$ transition was 40 μm long, and the propagation length in the *M* state was 100 μm. Only half the polarizer was simulated to reduce memory requirements, but the

observed insertion losses were doubled to take this into account. Operation at λ = 633 nm and 1110 nm was investigated. The normalized electric field distributions are shown in Fig. 5.8, and the performance is summarized in Table 5.3.

The performance of the simulated TM-pass polarizer is again exemplary across the entire bandwidth simulated, with insertion losses below 0.2 dB and an extinction ratio exceeding 21 dB. Such high performance is remarkable considering that both TM-pass and TE-pass polarizers can be implemented with the same processing as for a PBS.

5.2.3 Polarization-cloaked micro-ring resonators

So far, a powerful method for designing and implementing high-performance polarizers and PBS has been presented, taking advantage of transitions between the fundamental and hybrid waveguide states available with TAP. It can also be used to impart broadband, polarization-selective behavior to other integrated devices. Consider a micro-ring resonator, in which light is coupled into the ring cavity, with the amount coupled dependent on the coupling coefficient. For applications such as polarimetric remote spectroscopy, it may be desired to have light of only one polarization resonate in the ring, so as to apply a spectral filtering profile to that particular polarization state. The other polarization ideally would not couple into the ring at all in order to preserve high efficiency. We refer to this device as a "polarization-cloaked micro-ring resonator" (PCMR) since the ring cavity is invisible to one polarization state. A simple way to achieve a similar effect might be to simply pass the incoming light through a PBS, and insert the microring resonator into one arm with the desired polarization, then re-combine the polarization channels through another PBS. Despite its simplicity, this approach is inefficient, consumes significant chip area and adds unnecessary insertion losses from additional components. Alternatively, one might choose to control the TE and TM coupling coefficients into the ring by taking advantage of their different field distribution.

However, for systems with smaller index contrast, this disparity is less pronounced and useful. It also only works for one polarization, and is limited in bandwidth. As another option, one might exploit the modal birefringence of a conventional waveguide to engineer the coupling length of the bus such that one polarization achieves constructive transfer to the other waveguide, while the other encounters destructive interference. This would require relatively long coupling lengths which may not be possible depending on the size of the cavity, and it would have a limited bandwidth in order to achieve resonant coupling.

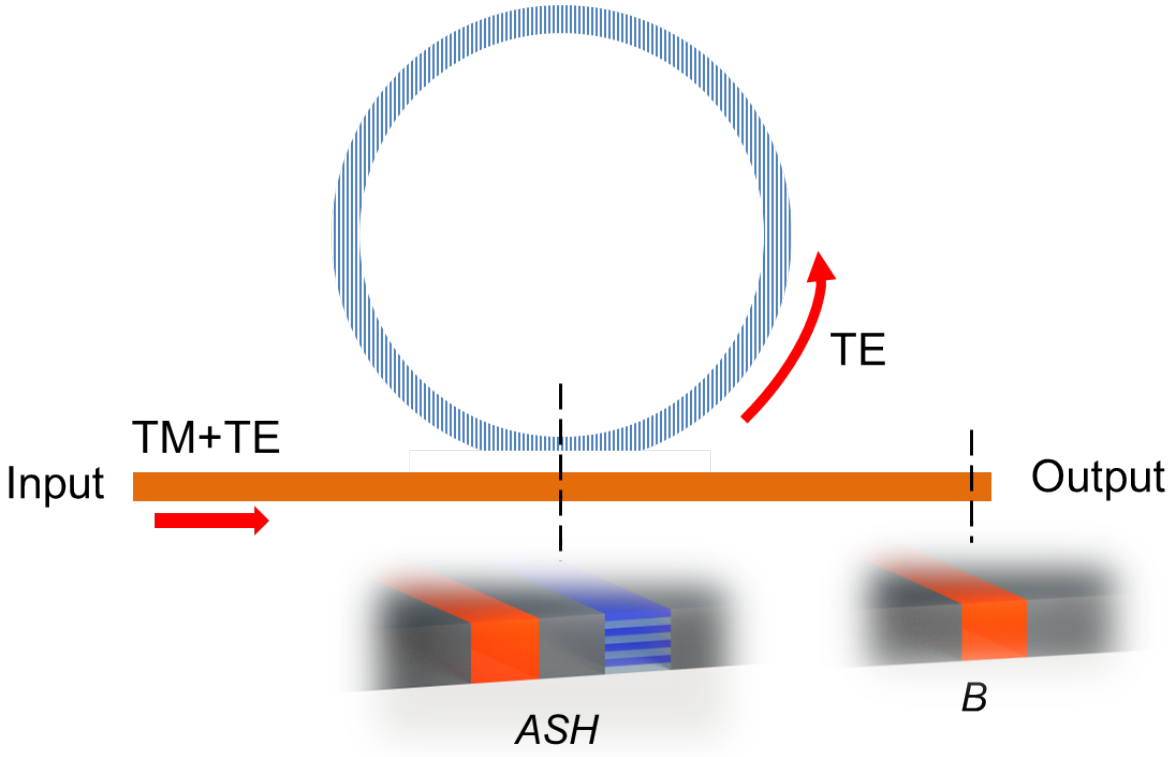

Figure 5.9: Schematic view of the proposed polarization-cloaked micro-ring resonator design (TE-resonant case).

TAP provides a means of realizing a true PCMR for the first time. The design of a TAP PCMR (shown schematically in Fig. 5.9) follows a similar procedure to that of the PBS. In the PBS, a *B*

waveguide is transitioned to the *ACH* state such that the TE and TM modes are split apart and (ideally) totally diverted into separate paths. For a micro-ring resonator, the coupling region is nothing more than a directional coupler engineered to give a specific (and usually small) coupling coefficient. Thus, one can imagine a TAP PBS that is instead engineered to be a polarization-selective directional coupler with a small but finite coupling coefficient for the resonated polarization, and zero coupling for the "through-polarization." As with a normal directional coupler, the degree of coupling is tunable by the gap between the bus waveguide and the drop waveguide. To achieve this, the transition that takes place is $B - ASH - B$ as the bus waveguide crosses the ring cavity.

There are two important structural considerations in a TAP PCMR design. First, as with the PBS, the polarization splitting is achieved by using different core materials for the TE and TM ports. For a TE-resonant PCMR, the core material in the ring waveguide should thus be MLS, and the core material in the bus should be SiON. Secondly, the transition to and from the *ASH* state should allow the mode to gradually evolve. This follows from the use of a gradually widened MLS core in the previous PBS design. Since there is now a gap of SiO_2 cladding separating the bus and the ring waveguides in the PCMR, this can instead be implemented by gradually tapering down and up the width of the ring waveguide. The degree of tapering and the gap allow control over the polarization coupling ratio (PCR) and the coupling coefficient, respectively.

The proposed PCMR design was simulated using a similar approach as before for the PBS and polarizer. The simulation was limited to the coupling section, rather than the complete ring structure, to reduce memory requirements. The bus and ring waveguide nominal widths were 1.1 μm, the ring radius was 100 μm, and a width taper-down to 900 nm was applied in the ring waveguide by "clipping" the bottom portion as seen in Fig. 5.10. An edge-to-edge gap of 500 nm was used in the clipped waveguide region. Simulations were conducted at λ = 850 nm for TE- and TM-polarized incoming light, for both the TE-resonant and TM-resonant PCMR cases. Additionally, the case of a purely isotropic ring and bus waveguide configuration was examined to validate the principle of

operation. The 2D normalized electric field profile of the simulations is shown in Fig. 5.10, and the relevant data are summarized in Table 5.4.

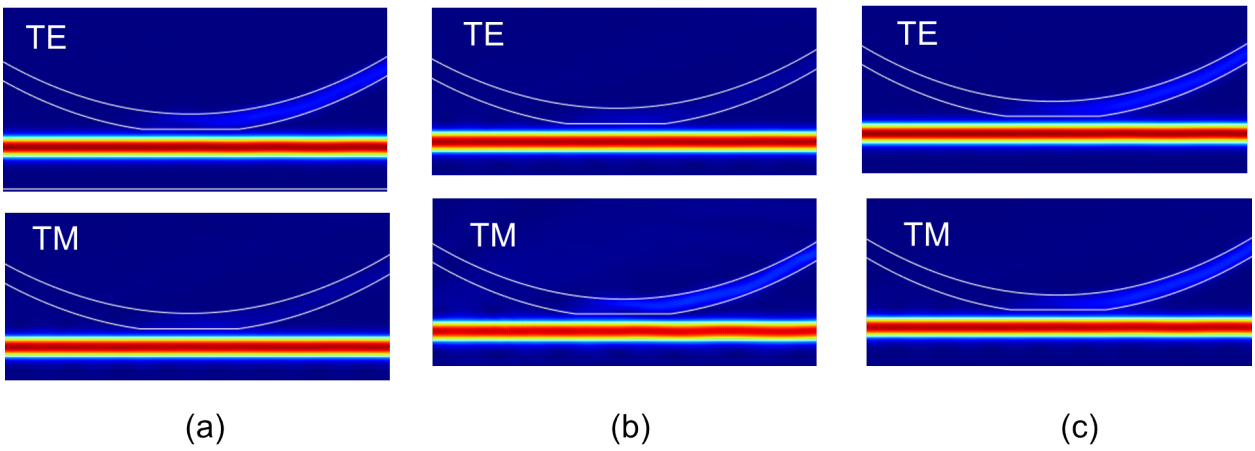

Figure 5.10: Normalized electric field profile from a top-view of the simulated polarization-cloaked micro-ring resonator for the (a) TE-resonant design, (b) TM-resonant design, and (c) SiON-core-only design (non-selective). Top: TE input light; Bottom: TM input light.

Table 5.4: Simulated PCMR performance

Device type	% TE coupled	% TM coupled	PCR, dB
TE-resonant	1.55	0.092	12.3
TM-resonant	0.091	2.66	14.7
SiON-only	1.75	2.45	1.46

For both the TE- and TM-resonant designs, wherein the only difference was simply swapping the position of the MLS and SiON core materials, a high PCR was achieved, exceeding 12 dB. Comparatively, when the same ring was simulated but with SiON in both the ring and bus cores, there was only a small PCR of 1.46 dB. This validates the design approach of using paired anisotropic and isotropic core materials to maximize the PCR in this device.

5.3 Fabrication and characterization

TAP samples were prepared for for testing of the PBS and PCMR designs. An MLS consisting of 15 pairs of Si_3N_4/SiO_2 layers (Fig. 5.11 was optimized in fill fraction to give a TE refractive index of ~ 1.715 and a TM refractive index of 1.65. The total thickness of the MLS is approximately 700 nm. The SiON film was then optimized to give a refractive index of 1.68. The MLS was deposited on an oxidized silicon substrate after previous deposition of gold markers to allow for multiple lithography stages.

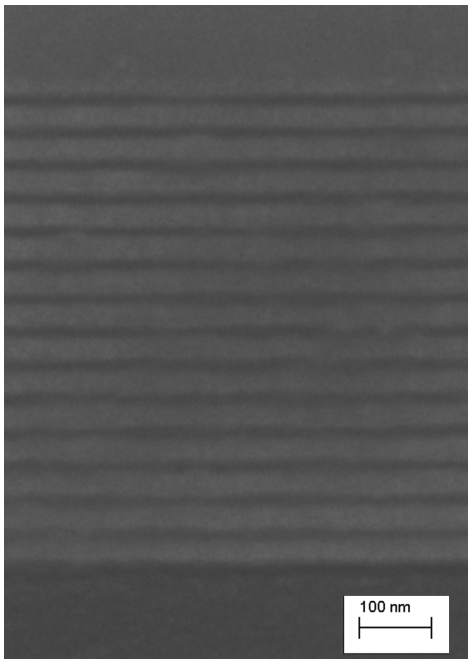

Figure 5.11: SEM of the fabricated MLS cross-section. The apparent roughness is a result of wet-etching performed to enhance the visible contrast of the layers.

5.3.1 Polarizing beam splitter

A chip layout was created to allow robust testing of the earlier proposed PBS design. An example propagation path for a PBS test device is given in Fig. 5.12. A common input waveguide 1.5 μm wide is first tapered down to 0.7 μm and propagated for 300 μm to extinguish most higher-order mode content. Then it passes through a 50:50 Y-junction splitter into a ”device” and a ”reference” path. In the device path, the waveguide width is tapered to the appropriate value for the PBS, and then back down to 0.7 μm afterward to allow a larger separation between the TE and TM ports. Finally, it is tapered up to 1.5 μm for low-loss propagation to the output ports. In the reference arm, the waveguide is tapered up to the 1.5 μm output width after a short propagation length to provide appropriate path length matching between the reference and the device path.

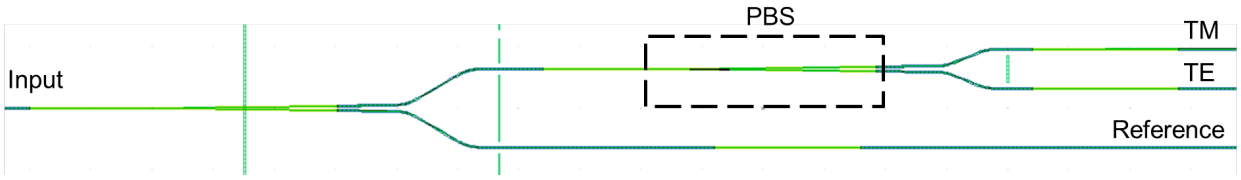

Figure 5.12: Computer-generated layout of the fabricated TAP test chip incorporating a polarizing beam splitter device.

This scheme allows highly repeatable measurements, largely independent of the input coupling conditions. Also, to improve the sensitivity, the slab material was etched in 3-μm-wide trenches at several steps across the chip (visible as long vertical lines in Fig. 5.12), causing any slab-coupled light to be diffracted out of the chip.

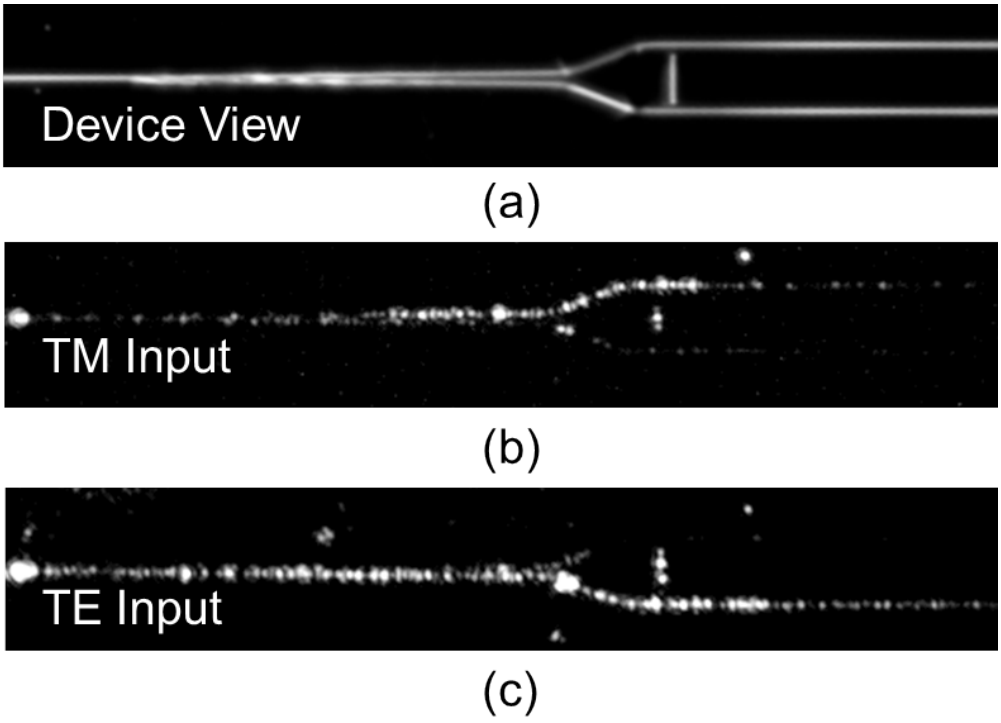

Figure 5.13: Optical micrograph of the (a) fabricated TAP PBS under (b) TM-polarized input light and (c) TE-polarized input light.

The PBS design was fabricated with the same dimensions simulated earlier (see Appendix A.5 for fabrication details). For characterization, light was coupled in through a 10x objective lens from free-space laser sources at λ = 633, 780, 850 and 1110 nm. At λ = 633 nm, a glass polarizer was used to polarize incoming light in either the TE or TM orientation. At the other wavelengths, a Glan-Taylor polarizer was used instead. An optical micrograph of a fabricated PBS and the fan-out from the device is shown in Fig. 5.13, with additional images of operation under TE and TM polarization to show the highly efficient routing achieved. Light scattering from the output facets was imaged from a top view with a digital camera, such that the TE, TM and reference ports were all visible. The optical power in each port is thus proportional to the integral of the intensity profile of the scattered light from each port. This method is superior to fiber-based out-coupling, since it

does not depend on any precise alignment at the output, and simultaneous measurements can be made on the device and reference ports, eliminating drift-induced errors. An example image of this measurement is provided in Fig. 5.14 (saturated for clarity), showing the TE, TM and reference port modes under both TE and TM illumination at λ = 850 nm. For calculation of insertion losses, the brightness was always adjusted to avoid saturation of the pixels. In some cases, the performance fluctuated based on the coupling conditions, possibly due to small amounts of multimode optical power that survived the mode filter. Several measurements were conducted when necessary and averaged to obtain the final results. The uncertainty in all PBS measurements is roughly $\pm$ 1.0 dB for insertion losses and $\pm$ 3.0 dB for extinction ratios. The characterization results are summarized below in Table 5.5.

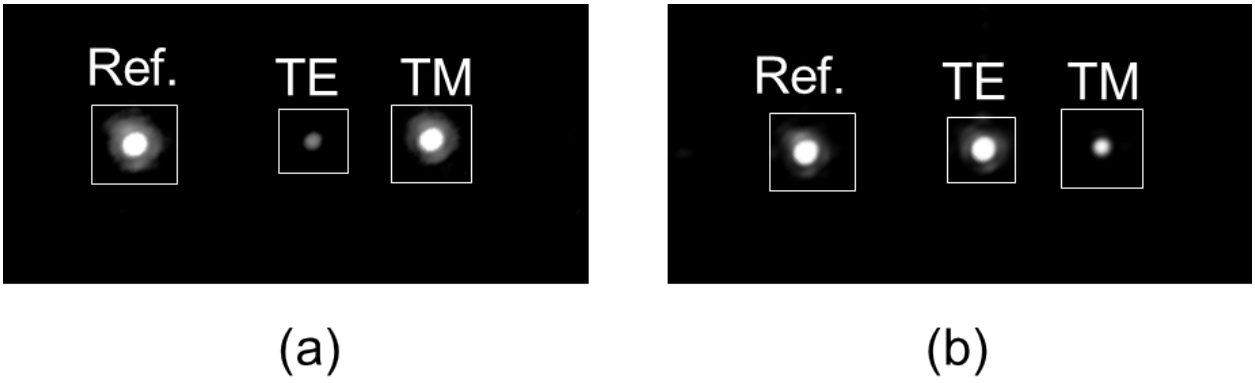

Figure 5.14: Saturated top-view digital image of the scattered light from the reference, TE and TM output ports of a fabricated PBS under (a) TM-polarized input light and (b) TE-polarized input light.

Table 5.5: Experimental PBS results

Wavelength, nm	Ins. loss (TE), dB	Ins. loss (TM), dB	ER (TE), dB	ER (TM), dB
633	1.27	0.49	5.95	25.8
780	0.15	0.98	16.3	15.1
850	0.34	1.54	12.9	26.2
1110	1.21	2.03	23.3	10.9

The fabricated PBS achieved ER $>$ 10 dB and maximum insertion losses of $\sim$ 2 dB over a 330 nm span from λ = 780 - 1110 nm, representing a fractional bandwidth of 0.51 octaves. This is the broadest bandwidth in an integrated PBS ever demonstrated, by more than a factor of 3. Moreover, the device showed acceptable insertion losses even to λ = 633 nm, although the extinction ratio for TE light was reduced to 6 dB at this wavelength. This strongly suggests the potential to extend the bandwidth of TAP PBS devices to even greater limits.

While the experimental results show drastic improvements over all prior integrated PBS devices, there is still a discrepancy between these and the simulated performance, which predicted lower losses of approximately 0.3 dB. One limitation is proximity effects during etching of nanoscale features such as the wedge splitter. For very narrow gaps, the MLS or SiON may not be etched fully, resulting in a deviation ideal geometry. Specifically, this reduces the effective contrast achieved between the MLS, SiO_2 and SiON zones. This could be addressed in the future by optimizing the etching recipe.

Another issue could be the lack of perfectly flattened surfaces after the etch-back-based planarization. A local surface planarization (in the vicinity of etched features) of approximately 200 nm was achieved, which is large enough to influence the index contrasts and interfere with ideal performance. This could be readily addressed by instead using conventional chemical-mechanical polishing (CMP) techniques to achieve a high degree of planarization (this was not used because it

was not available in-house).

5.3.2 Polarization-cloaked micro-ring resonator

Another TAP chip was fabricated to assess the performance of the PCMR design proposed earlier. It incorporated all of the same dimensions provided there, with the exception of a slightly larger edge-to-edge coupling gap of 600 nm instead of 500 nm. The TE-resonant and TM-resonant rings of 100-μm-radii were tested with a polarized single-longitudinal mode VCSEL source at λ = 850 nm (Thorlabs CPS850V), oriented at 45 degrees with respect to the plane of the chip. The light was then polarized in the horizontal and vertical directions as required with a Glan-Taylor polarizer. To sweep the laser through the ring resonances, the casing was placed in an aluminum heat-sink with a cartridge heater and thermistor and slowly heated from room temperature to 50°C. The voltage-to-temperature characteristic of the thermistor was calibrated earlier by coupling the light into an optical spectrum analyzer (OSA). A tuning range of $\sim$ 1 nm was achieved with this approach.

Light was coupled onto the chip via a 20x objective lens, and collected at the output by a lensed fiber and detected on a near-IR power meter. An optical micrograph of a PCMR on-resonance is provided in Fig. 5.15.

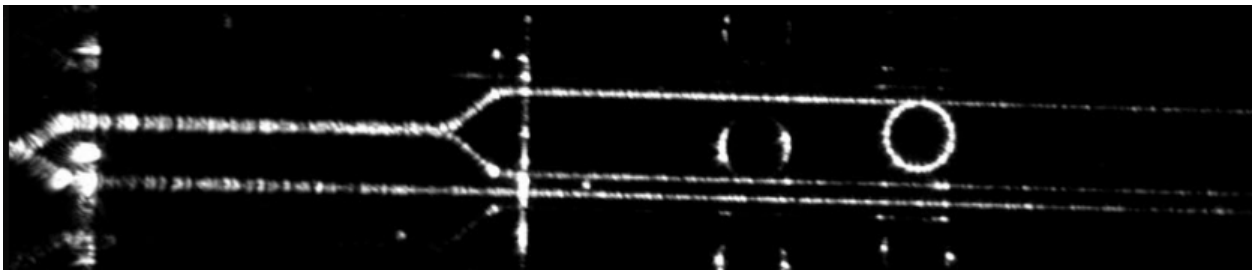

Figure 5.15: Optical micrograph of a PCMR with light coupled into a resonant mode.

The transmission spectrum during sweeps was recorded for both TE and TM input light, for TE-resonant and TM-resonant rings of 200-μm-radius (Fig. 5.16). The quality factor was measured to be 69,000 $\pm$ 20,000 for the TM-resonant device, with an FSR of 105 GHz $\pm$ 10 GHz. For the TE-resonant device, it was 112,000 $\pm$ 20,000, with an FSR of 104 GHz $\pm$ 10 GHz. The uncertainties are introduced by small deviations from the calibrated temperature-wavelength tuning curve previously obtained. The quality factor was possibly limited by etch-induced roughness on the surface or sidewalls. It is clear from Fig. 5.16 that resonances were observed for the intended polarization in each type of PCMR. However, when the input polarization was orthogonal (i.e. TE-polarized light coupled to the bus of a TM-resonant PCMR), no resonances were observed in the transmission spectrum. This provides a clear observation of a large polarization coupling ratio (PCR) achieved by the TAP PCMRs, indicating nearly perfect cloaking for the through-polarization state. This is the first demonstration of this behavior in integrated photonics.

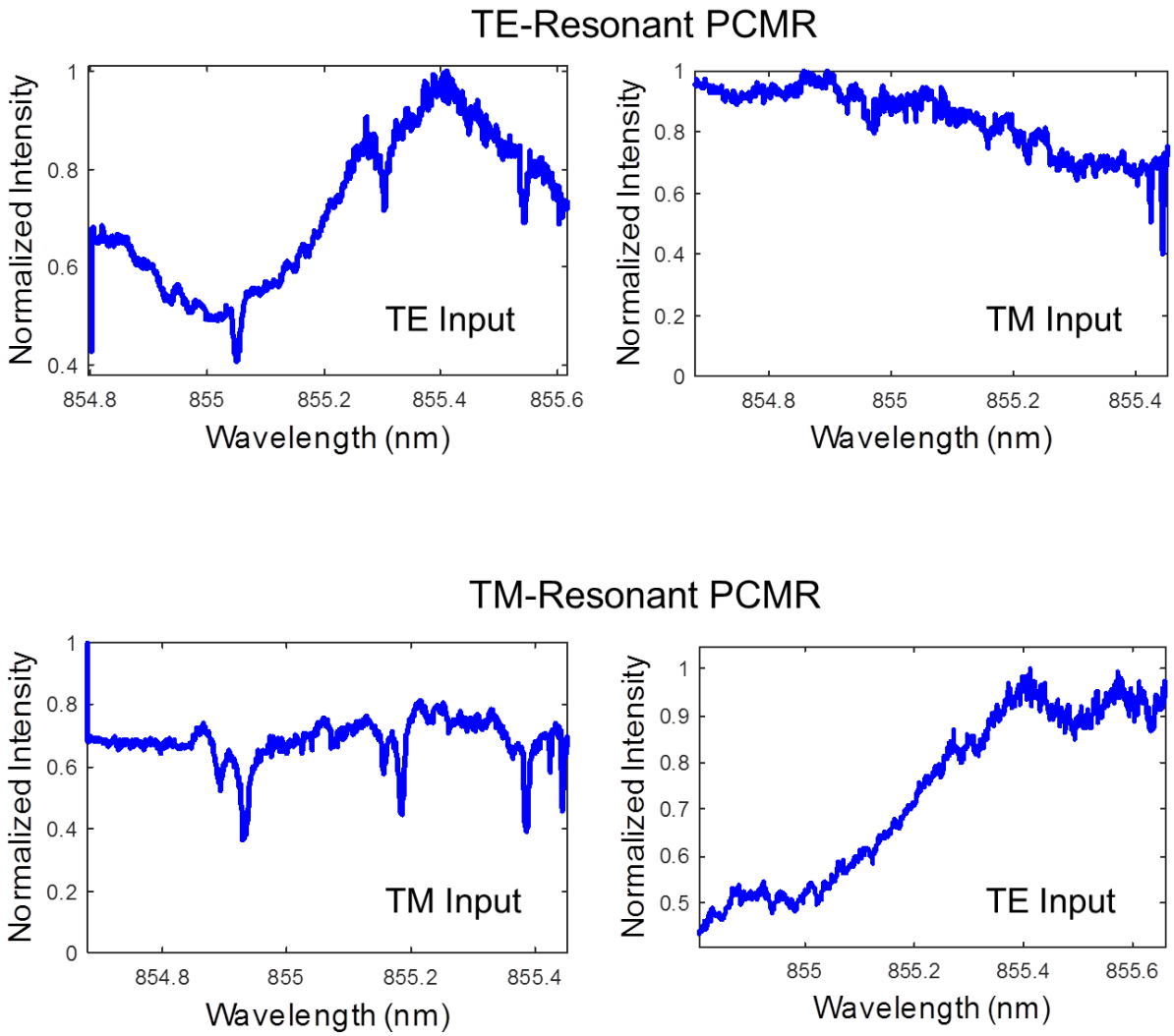

Figure 5.16: Transmission spectra from (top) a TE-resonant PCMR and (bottom) a TM-resonant PCMR.

Only a dim oscillation in the ring cavity could be perceived in the top view in the case of the TE-resonant ring with TM input light, possibly from a small amount of cross-polarized light entering the cavity. In the case of the TM-resonant PCMR, no resonance was ever observed in the top-view when TE light was injected to the bus. Additionally, since two notches are visible in the intended polarization state and the FSR between the TE and TM modes are only marginally different at

this wavelength, it is guaranteed that at least one notch would have been visible for the orthogonal polarization.

5.4 Conclusion

In conclusion, an approach to achieving broadband and highly efficient polarization-selective integrated photonics, called *Topographically Anisotropic Photonics* (TAP), was proposed, simulated and validated with fabricated and characterized devices. We investigated polarizing beam splitters (PBS) using this approach, and demonstrated a device achieving a record fractional bandwidth of 0.51 octaves, while maintaining ER $>$ 10.9 dB and a maximum insertion loss of $\sim$ 2.0 $\pm$ 1 dB, exceeding the prior record in integrated PBS bandwidth by more than a factor of three. We also designed, fabricated and characterized a novel integrated photonic device taking advantage of TAP, the polarization-cloaked micro-ring resonator (PCMR), and demonstrated that it strongly suppresses coupling into the cavity of one polarization while maintaining normal coupling for the other. Further improvements to the planarization and etching are expected to drastically improve the performance in both loss and bandwidth. Many more high-performance polarization-selective devices are possible with TAP, such as TM and TE-pass polarizers with expected losses below 0.2 dB and extinction ratios $>$ 21 dB over a span from λ = 633 - 1110 nm.

CHAPTER 6: CHALCOGENIDE INTEGRATED PHOTONICS

6.1 Background

Chalcogenide glasses (ChG) have been successfully utilized in a broad range of photonic platforms and devices [17]. They offer fairly high refractive indices, broad transparency in the infrared region, and high optical nonlinearity. The field of integrated photonics in particular, has benefited greatly from these properties, as chalcogenide materials can be readily deposited on conventional silicon or polymer substrates and patterned to form optical waveguides. To obtain the strongest nonlinear effects and retain compact device sizes for multi-element integrated photonic systems, sub-micron-sized optical modes and device features are desired. There are three main techniques which have been employed for patterning sub-micron ChG waveguides, namely, liftoff patterning, nanoimprinting, and dry etching [95–97].

Dry etching can produce features with steep sidewall angles, allowing very small gaps and grating periods to be achieved. In addition, it places no restrictions on the distribution or height of features that can be produced, making it suitable for a variety of applications.

In this chapter, microring resonators with extremely low-loss sub-micron ChG waveguides are reported [98, 99]. The waveguides are obtained by a dry etching method, featuring compact waveguide dimensions and excellent device yield. It is shown here that Cl_2 plasma etching can be used to obtain ChG waveguides with lower loss than those etched with CHF_3, achieved in the same etching chamber. In addition, highly efficient fiber-to-waveguide grating couplers are demonstrated in ChG devices, showing the robustness of dry-etching for achieving challenging feature dimensions. By using grating couplers to couple light in and out, the need to dice and polish the chips can be avoided, saving time and improving yield. Thus, they are an important element to a complete pho-

tonic platform based on ChG materials. As demonstrated in this work, the simultaneous formation of grating couplers and ridge waveguides with one etching step further reduces the complexity of this fabrication approach.

6.2 Design and implementation

Fabrication started with standard solvent cleaning of 100-mm diameter silicon wafers with 2 μm of thermal oxide grown on the surface. Electron-beam deposition was used to produce the ChG films on the surface of the silicon dioxide. This deposition method has been previously reported [100], and is further investigated here under different deposition conditions. The deposition was performed at a rate of about 1 nm/s, starting with 1 x 1 cm^2 cylindrical rods of bulk glass with the composition $Ge_{23}Sb_7S_{70}$. Bulk $Ge_{23}Sb_7S_{70}$ glass was fabricated by traditional melt quenching techniques [101]. A film approximately 630-nm-thick was deposited on the surface of the wafer. Compositional analysis with energy dispersive X-ray spectroscopy (EDX) using a JEOL 733 Super Probe was used to compare composition of the starting bulk glass and as-deposited films. Error on the measurement was approximately ± 1 at%. The bulk glass had a composition of Ge 22 at%, Sb 7 at%, and S 71 at%. The deposited film composition was Ge 22 at%, Sb 11 at%, S 67 at%. The film composition is slightly non-stoichiometric compared to the bulk glass, which is likely an effect of the varying volatilization rates of the elements, commonly seen in ChG film deposition, and observed in previous studies of thermally evaporated $Ge_{23}Sb_7S_{70}$ [102]. The film refractive index was measured to be 2.22 at a wavelength of 1550 nm using the prism-coupling method. Waveguide patterning was performed using electron-beam lithography with ZEP 520A photoresist. After resist development, the line edge roughness of the pattern was reduced by reflowing it on a hot plate at 150°C for 5 minutes. The final waveguide width after reflow was found to be 750 nm (starting with 700 nm in the design). Plasma etching was performed using a Unaxis Shuttleline

inductively-coupled plasma reactive ion etcher (ICP-RIE). Two different etching recipes based on CHF_3 and Cl_2 were investigated in order to determine the best performance (see Appendix B.5 and B.6). Both samples A (CHF_3-etched) and B (Cl_2-etched) were etched by approximately 290 nm at a temperature of 20°C. Sample A had a thickness of 600 nm, and Sample B was 650 nm thick. After the etching, the samples were coated with a benzocyclobutene (BCB) polymer cladding to protect the surfaces from contamination and to reduce scattering from the sidewalls. The curing of the polymer was performed in a nitrogen oven at a maximum temperature of 220°C. BCB has negligible ($\sim$ 0.04 dB/cm) losses in the near-infrared [103]. The simulated transverse-electric (TE) polarized mode intensity profile of the fabricated waveguides is shown in Fig. 6.1(a), with a scanning-electron-microscope (SEM) image of a cleaved waveguide facet in Fig. 6.1(b). The simulated waveguide from this geometry is single-mode, and its mode size is not significantly affected by the 50 nm thickness difference between samples A and B.

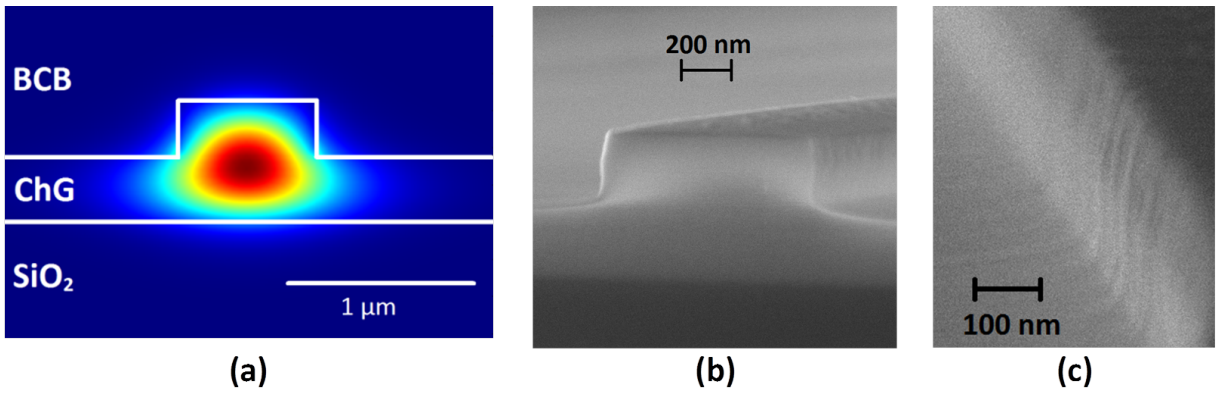

Figure 6.1: (a) Simulated TE-mode intensity profile of a fabricated ChG waveguide; (b) Scanning-electron-microscope image of a cleaved waveguide facet; (c) Higher magnification scanning-electron microscope image showing waveguide sidewall roughness.

The waveguide performance was assessed by measuring the transmission spectrum through notch-filter microring resonators. Light was coupled in and out of the chips via fiber-to-waveguide grating

couplers and linear tapers for every resonator. A typical device is shown in Fig. 6.2(c). The fabricated sample contained a sweep of coupling gap distances with a fixed ring radius of 200 μm, allowing a clear distinction between over- and under-coupled states. The values of coupling and propagation losses were disambiguated by comparison of several waveguides with identical coupling gaps for each case. The measured coupling coefficient versus bus-to-waveguide gap distance is provided in Fig. 6.3(b). All of the fabricated devices on samples A and B with gap distances between 0.9 and 1.55 μm were tested to obtain an estimate of the yield for the process. The measured free spectral range (FSR) was found to be 0.842 nm. The group index, extracted from the fitted data, was measured to be 2.30.

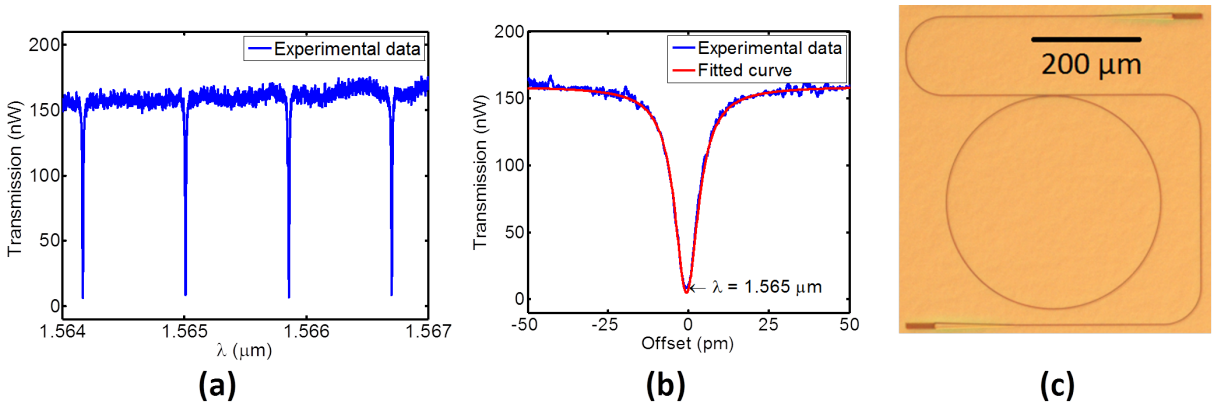

Figure 6.2: (a) Transmission spectrum of a ring resonator from Sample B (Cl_2-etched); (b) Single-resonance zoomed view showing the quality of the fit; (c) Optical micrograph of a typical device with a 200-μm-radius microring resonator and input/output grating couplers.

An example transmission spectrum on resonance for one microring is given in Fig. 6.2(a-b), showing a good quality of fit to the simulated response, obtained from standard models [104]. A histogram showing device performance from multiple resonators over two samples is given in Fig. 6.3(a). The high yield of the process is evident, with only one device from each sample showing abnormal behavior with higher losses. The best device on sample B, which was Cl_2-etched, showed

a propagation loss of 0.84 dB/cm, corresponding to an intrinsic (unloaded) Q-factor of 450,000. The corresponding values on the best device on sample A are loss of 1.34 dB/cm and an intrinsic Q of 288,000. The highest attainable loaded Q values are 121,000 and 168,000 for sample A and B, respectively. The mean loss for Sample A and B are 1.78 $\pm$ 0.26 dB/cm and 1.08 $\pm$ 0.14 dB/cm, respectively, corresponding to a mean intrinsic Q of 215,000 and 350,000. Sample B shows better process uniformity with a lower standard deviation. The standard deviation and the mean loss were obtained by statistical analysis of the ensemble of resonators, excluding only the single abnormal resonator in each sample (outliers in Fig. 6.3(a)).

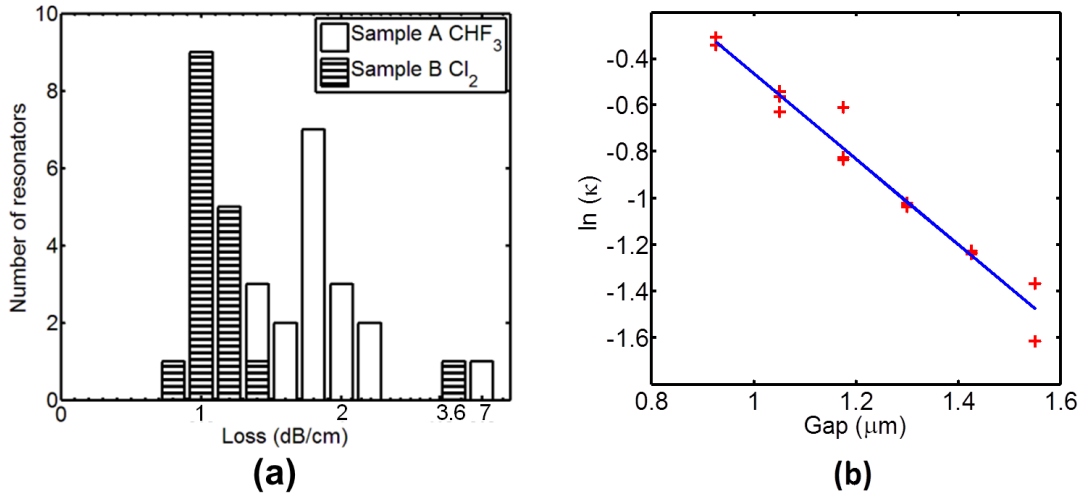

Figure 6.3: (a) Histogram of propagation losses for each measured resonator from the two samples; (b) Coupling coefficient of the microring resonators versus the edge-to-edge gap of the bus and ring waveguides. The red data points are measured values, and the blue line is a natural logarithmic fit to the data.

The Cl_2 plasma etching approach produces substantially lower etching-induced losses than CHF_3 as seen in sample B. The measured propagation loss can come from several different sources, namely, sidewall scattering from roughness on the waveguides, surface scattering, intrinsic ma-

terial losses, and bending losses due to the measurement of a bent waveguide in a microring. Although the material loss was not characterized in this work, thermally-evaporated $Ge_{23}Sb_7S_{70}$ films have been previously shown to have material losses of $\sim$ 0.15 dB/cm [105], so this is used as an estimate here. COMSOL^{TM} simulations show a critical bending radius of 52 μm for these waveguides, and a negligible bending loss of 0.004 dB/cm for the 200-μm-radius resonators employed. An atomic-force-microscope (AFM) scan of the blank film surface showed an RMS surface roughness of 0.64 nm, which introduces negligible loss [106]. Thus, sidewall scattering is expected to contribute most of the propagation loss. Analysis of an SEM image of the waveguide sidewalls (Fig. 6.1(c)) gave an estimated peak-to-peak sidewall line-edge roughness value of 20 nm. This may originate in the pattern produced by the lithography, though it is reduced by the reflow process. It is also apparent from Fig. 6.1(c) that the sidewalls are not completely vertical; accordingly, the plasma has some small isotropic component that etches the sidewalls, producing this effect. Considering the absence of a polymerizing agent generated in the plasma, this is plausible. To further investigate the influence of sidewall roughness on the losses, microring resonators from 1000-nm-wide waveguides were also fabricated. However, no significant difference in propagation loss was observed when compared to the 750-nm-wide waveguides. Further optimization of the etching conditions and resist patterning are expected to reduce the sidewall roughness and improve performance.

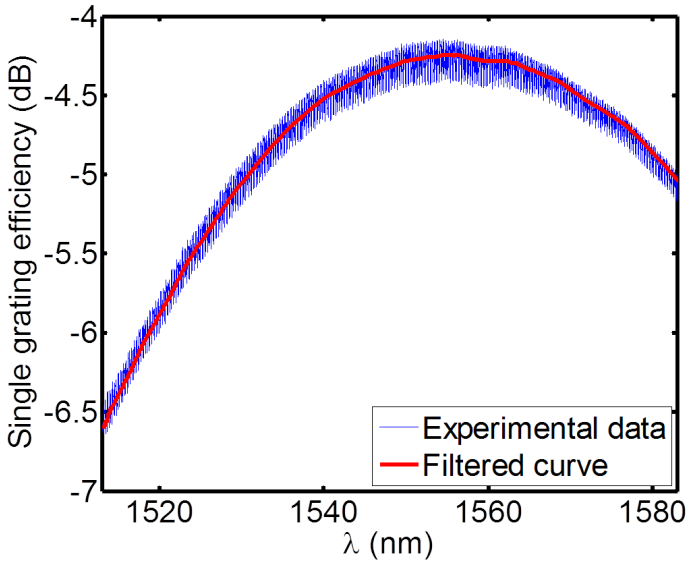

Figure 6.4: Grating coupler efficiency versus wavelength. The upper-wavelength measurement is limited by the tuning range of the laser.

Grating waveguide couplers were also demonstrated in chalcogenide integrated photonics. The grating has a fixed duty cycle of $\sim$ 35%, a period of 1 μm, an etch depth of 290 nm, and a film thickness of 630 nm. SMF-28e single-mode fibers were aligned to the grating couplers at an incident angle of 14 degrees. Index-matching fluid with a refractive index of 1.4 was used to reduce reflection losses from the grating facets. A partial sweep of the transmission through a chip with input and output gratings (limited by the lasers tuning range) is shown in Fig. 6.4, showing the insertion loss with respect to wavelength. The peak coupling efficiency for a single grating is measured to be 37% $\pm$ 6% (4.3 dB $\pm$ 0.7 dB) from the experimental data.

6.3 Conclusion

A technique for fabricating low-loss chalcogenide waveguides has been presented. With chlorine and argon dry etching, high-quality-factor subμm ridge waveguides based on $Ge_{23}Sb_7S_{70}$ were demonstrated. When compared with identical CHF_3-etched waveguides, a clear improvement in waveguiding performance for Cl_2-etched waveguides was observed. In addition, high-efficiency grating couplers with a single-grating loss of 4.3 dB were achieved. With enhanced apodized grating designs, even higher efficiencies should be possible.

CHAPTER 7: FUTURE WORK

In this dissertation, the design and development of several novel platforms has been discussed, including work on several micro-photonic devices which leverage their unique characteristics. Still, there is a great deal of room for further research in these technologies, which offer great potential for new photonic functionality, but also will bring to light many intriguing challenges during their progression. In this section, a collection of research concepts, each building on a specific branch of relevant technology, will be presented. Some of these projects are at the simulation or theoretical stage of development, whereas others have had extensive experimental work already conducted. Regardless, all represent promising directions for continued study.

7.1 Mid-IR silicon Raman lasers

A major application of the silicon photonics platforms that have been proposed and demonstrated is for frequency conversion in the mid-IR spectrum. Due to the general lack laser sources in this region, it is desirable to develop efficient methods for achieving non-conventional laser wavelengths, or to broaden the spectra of available sources to enable wideband sensing in this regime. In this section, experimental progress toward silicon Raman lasers in the mid-IR will be discussed.

7.1.1 Theory

In the introduction of this dissertation, silicon Raman lasers were introduced in the context of near-IR spectrum operation. Ultimately, the performance of near-infrared Raman lasers is limited by two-photon and subsequent free-carrier absorption, which are only partially mitigated by carrier-sweep-out techniques. To avoid these problems, SRS has been investigated in the mid-IR, where

TPA is absent. Raman amplification has been demonstrated in the mid-IR at 3.39 μm [107], and sub-lasing-threshold behavior in bulk silicon [108], but to date, a mid-IR silicon Raman laser has not been realized. One problem is the wavelength dependence of the Raman gain coefficient, which could be estimated to be only 4.5 cm/GW in [107] at 2.88 μm, making lasing more difficult. Nevertheless, the prospect of such a laser is enticing, due to its ability to obtain additional spectral coverage in the mid-IR for spectroscopic applications. By cascading Raman lasers in a cavity, very large frequency shifts can be achieved [109].

7.1.2 Cavity architectures and design

In Chapter 3, the ASOP was introduced as a robust platform suitable for mid-IR photonics, making it an ideal choice for implementing a Raman laser. For wavelengths above 4.2 μm, μm-scale SOI waveguides suffer from excess material absorption from the silicon-dioxide bottom cladding. For initial testing, however, it is convenient to fabricate the laser cavities using conventional SOI wafers, and choosing to test them in the range of 2.5 - 4 μm. After a Raman laser has been demonstrated under these conditions, it will be achieved with ASOP technology, lending to lower losses and longer-wavelength operation. The experimental setup for testing the cavities will be described, and then the design of SOI-based Raman laser cavities. The experimental setup is depicted in Fig. 7.1.

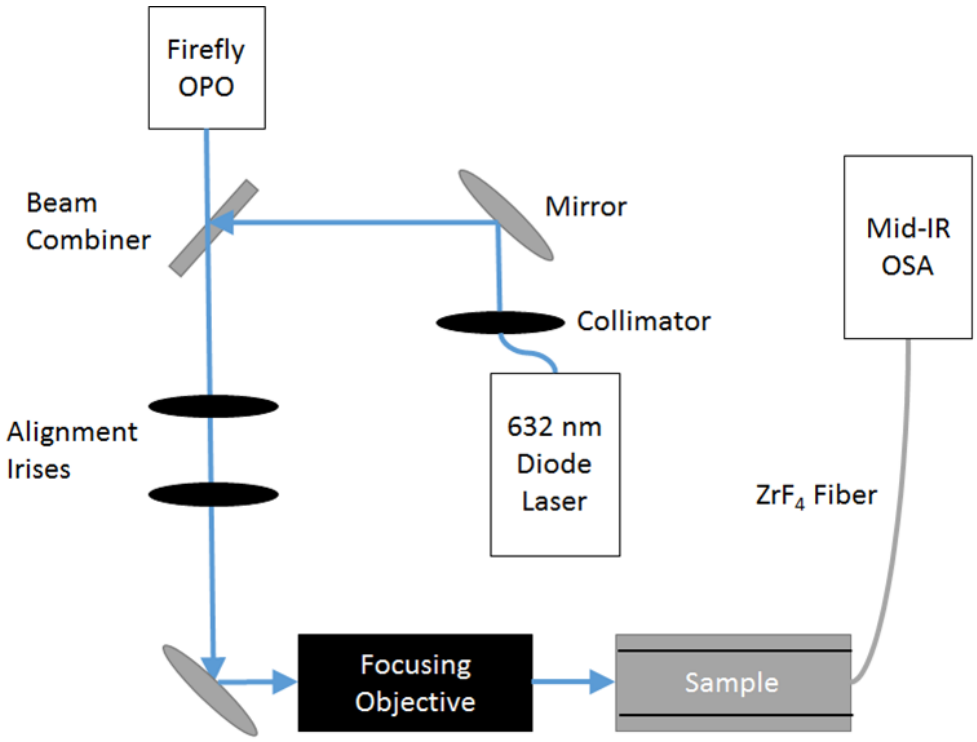

Figure 7.1: Mid-IR measurement setup.

An optical parametric oscillator (OPO) (M-Squared Firefly) was used as the pump source, tunable from 2.44 to 3.76 μm, with a pulse width of $\sim$ 10 ns, a linewidth of 100 - 300 GHz, and a peak power of approximately 100 W. It should be noted that the linewidth of this source is greatly reduced for wavelengths $>$ 3 μm, which in turn provides the most efficient pump power transfer. Thus, only pump wavelengths from 3 - 3.76 μm are considered in detail. The beam quality is estimated by the manufacturer to have an M^2 value of 1.5. The OPO was initially aligned with a collimated multimode red diode laser, then the beam was focused through a zinc selenide objective lens to a spot diameter of approximately 8 μm. After coupling losses, the pump intensity at the focal point was approximately 50 - 100 MW/cm^2. The objective lens can be translated slightly to provide fine alignment to the waveguide facet without disrupting the chip position. On the output

side, a single-mode zirconium fluoride fiber (Thorlabs) was used to collect light from the cavity. The fiber facet was left at the polished ferrule to preserve mechanical robustness. The fiber was coupled into an optical spectrum analyzer (Thorlabs OSA 205) for analysis. A red beam was coupled backward through the fiber, providing a convenient visible spot with which to align the output facet and the fiber core. The pump polarization was fixed in the vertical direction, however, the effective polarization for the cavity could be conveniently changed simply by mounting the substrate on a 90-degree-rotated holder, and viewing the top surface through an angled mirror directed at it. This ensured that the same setup could be used without the need to reconfigure the microscope every time the polarization was changed. The pump power was varied by adjusting a shutter in the input path.

7.1.2.1 Uncoated "Macrowire" Silicon Waveguides

In the early days of silicon photonics, there was considerable attention paid to very large waveguides, on the scale of several μm tall and wide. This provided low propagation loss, ease of coupling to fiber modes [110], and greatly relaxed fabrication tolerances lending to low production costs. In addition, they can more efficiently utilize coated mirrors due to the small diffraction of large-waisted beams. In contrast to modern nanoscale and μm-sized waveguides, these could be deemed macrowires. The benefits mentioned are opposed by trade-offs to compactness, as a low index contrast is achieved, and relatively large bending radii are required, on the order of millimeters. But this trade-off is not problematic in the context of Raman lasers - a simple straight waveguide suffers no drawbacks except for a larger mode area. The goal of efficient wavelength conversion requires only a simple cavity, so no other components need be integrated on a chip-scale optically pumped laser. Thus, macrowires are a promising candidate for achieving a Raman laser on silicon.

The waveguide mode was designed with the assistance of the COMSOL^{TM}mode-solver tool. A

total thickness of 10 μm was assumed, with an etch depth of 5.5 μm and a ridge width of 8 μm. Such a design exhibits wideband single-mode operation. In designing the laser cavities, an analytical model for the Raman laser behavior was used [78], lending to quick optimization. A Raman gain coefficient of 5 cm/GW at a pump wavelength of 2.6 μm was assumed, which uses a $1/\lambda$ dependence referenced to a 4.5 cm/GW gain coefficient at 2.88 μm. The input parameters are the front and back pump and stokes (signal) facet reflectivities, the linear propagation loss, and the cavity length. First, an uncoated facet is considered. The loss is assumed to be small from [110], since sidewall scattering is diminished greatly from the highly core-confined mode. A value of 0.3 dB/cm is assumed. Then, all four facet reflectivities are given as the Fresnel reflection coefficient of $\sim$ 30%, a valid assumption given the large size of the mode. The waveguide is assumed to be oriented anywhere on the (100) plane such that the cross-polarized Raman emission can be harnessed [111]. Thus, the choice of TE or TM pump polarization is unimportant in this case. The intensity threshold for lasing versus cavity length is given in Fig. 7.2. The threshold at 5 cm length is 83 MW/cm^2, which is achievable by the pump source.

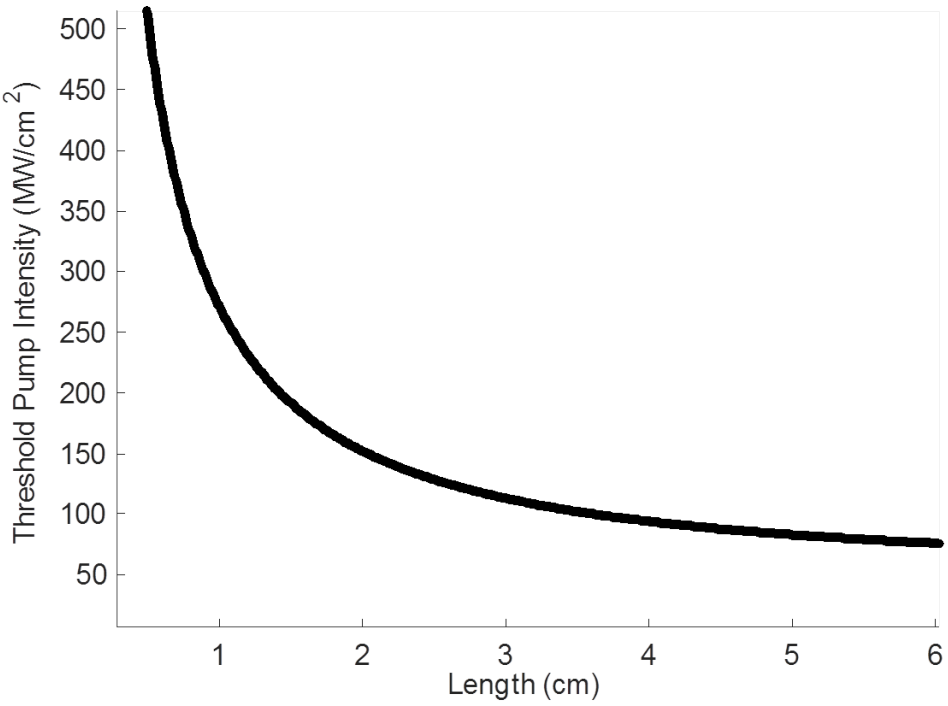

Figure 7.2: Theshold pump intensity versus cavity length for an uncoated silicon macrowire waveguide.

Straight waveguides of this design were fabricated using an in-house-made photomask with widths varying from 8 - 12 μm. The length was 5 cm. SOI substrates with a top layer silicon thickness of 10 $\pm$ 0.5 μm were used. Ridge waveguides were achieved by etching down by 5.5 μm. The chips were then diced, cleaved, and polished. Since the facets are much larger than the effective wavelengths involved, the facet internal reflectivity is very sensitive to the quality of the polish and the angle with respect to the waveguide propagation direction. This angle-sensitivity is commonly used in semiconductor chips to intentionally eliminate internal reflections [112], but here it presents an additional challenge to maintaining strong cavity resonances.

The fabricated macrowire chip was tested in the setup for pump wavelengths between 2.6 - 3.76

μm. Good modal confinement was confirmed by scanning the fiber around the output and observing strong intensity in the vicinity of the core and negligible power in the surrounding slab area. However, no Raman emission was detected at the output in any case, for either input polarization. Furthermore, destruction of the input facets was observed when the waveguide was placed at the focal spot of the pump at maximum power. It manifested as a sudden unrecoverable drop in transmitted power (typically $>$ 90 % loss). Inspection under microscope confirmed a catastrophic failure resulting in ejection of silicon micro-particles in the vicinity. The surface damage threshold of bulk silicon, in the nanosecond regime, and at 2 μm wavelengths, has been evaluated at roughly 370 MW/cm^2 [113], so this failure is unexpected for such low power levels in use. However, it is possible that the pulse width of the source is shorter than 10 ns and the peak power is higher, or that other imperfections to the waveguide facet contribute to a reduced damage threshold in this instance. Failure could be prevented by attenuating the input power by about 50 % adjusting an iris in the input, but this compromise to power also makes lasing in such a cavity unlikely.

7.1.2.2 Mirror-coated macrowires

Considering that the pump power is indeed constrained by the damage threshold, the threshold intensity for lasing must be lower. To achieve this, the reflection losses of the Stokes wave must be decreased. Thus, the mirror-coating of the macrowire facets was explored. To minimize the lasing threshold, a reflection coefficient of 90 % for the front and back facets was desired. Broadband behavior was also sought to allow flexibility in the pump wavelength tuning. To achieve high reflection coefficients and broad bandwidth, the coating must consist of alternating layers of low and high refractive index, with as large an index contrast as possible. It must also achieve good adhesion to the silicon facet so as to prevent stress-induced failure. Amorphous silicon and silicon dioxide provide a good index contrast (2.9 to 1.43) and adhere very strongly to each other and crystalline silicon, and they are also conveniently deposited using electron beam evaporation. The

mirrors were designed assuming normal incidence with the transfer-matrix-method (TMM) [114]. For convenient testing of the standalone mirror using the OPO, the reflection edge onset was chosen to be at a wavelength of 2.8 μm. This gives thicknesses of t_{si} = 319 nm and t_{SiO_2} = 647 nm. For a two-pair (four-layer) stack deposited on silicon, the resulting simulated reflection spectrum is shown as the blue line in Fig. 7.3, confirming a high peak reflection, a sharp edge (allowing low pump losses), and broad bandwidth.

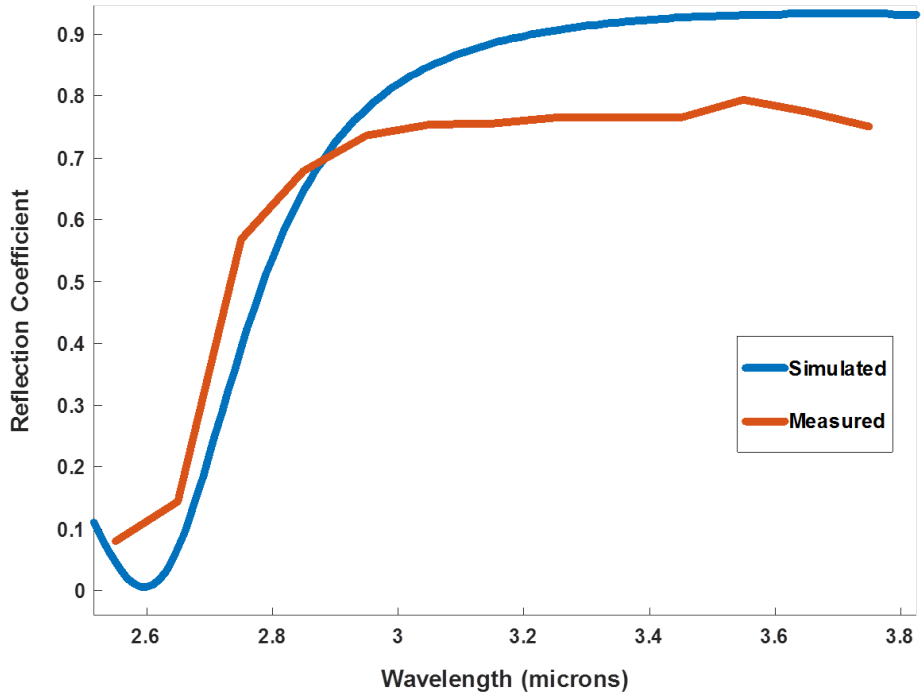

Figure 7.3: Single-facet mirror-coating performance.

Using the analytical model for the Raman laser, the estimated threshold for this configuration is plotted versus cavity length below. This mirror design was evaporated using electron-beam evaporation at CREOL, onto a double-side-polished silicon substrate. The mirror was then placed in the beam path of the OPO and analyzed using a power meter. Removing the back-side induced

reflection, the measured mirror reflectivity spectrum is shown in the red line of Fig. 7.3. Good agreement with the reflection edges position is shown, however, a significant reduction in peak reflection was observed. Furthermore, addition of a third pair of layers did not increase the reflection coefficient, and only increased background reflection (or parasitic absorption or scattering) out of the desired stop-band. As such, the actual benefit of the mirrors would not be as significant as expected. Mirrors were deposited on macrowires of various lengths, but no lasing was observed, indicating that the threshold was not lowered significantly, or that the facet quality was still not adequate. Although macrowires hold many potential benefits for efficient Raman laser cavities, the practical difficulties with facet preparation and high-quality mirror coating so far have prevented Raman lasing.

7.1.2.3 Distributed Bragg cavities

The distributed Bragg grating (DBR) is a ubiquitous element in photonics, applicable to many platforms and technologies. It consists of many alternating periods of high and low index regions, typically of a relatively small index contrast in comparison to typical deposited mirror coatings. As such, the bandwidth is smaller, on the order of several nanometers. In the context of integrated photonics, a DBR may be achieved by sidewall corrugation, a popular method for various silicon photonics applications [58]. In this way, the effective index of the waveguide mode is varied by changing the waveguide width. Depending on the depth of the corrugation and the initial waveguide width, the resulting index contrast can be varied considerably, and consequently, the bandwidth of the stop-band where reflection is highest. Adding or subtracting periods can be used to accurately control the reflection coefficient achieved. Thus, cavities formed by placing a simple waveguide between two DBRs can have highly controllable reflection characteristics, while maintaining a compact footprint thanks to the absence of bends.

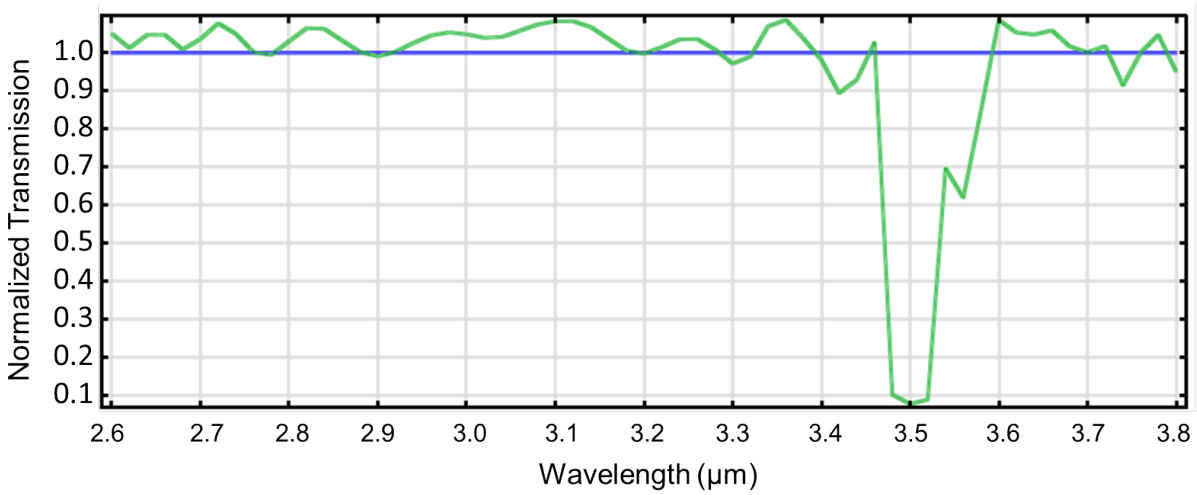

Figure 7.4: Transmission spectrum of an integrated DBR through COMSOL simulations.

Raman laser cavities based on DBRs are now considered. An 80-period DBR with a nominal waveguide width of 1000 nm and an outer corrugated waveguide width of 1200 nm, and a period of 630 nm. A 2D, effective-index-based model of a single-grating DBR was built in COMSOL using frequency-domain simulation methods. The relatively narrow waveguide widths were chosen such that the second symmetric guided mode was eliminated, preventing undesirable resonances at shorter wavelengths due to cross-mode coupling from the gratings. The simulation results are shown in Fig. 7.4. Note that the transmission fraction exceeds 1 (the blue line) in some portions due to normalization errors in the simulation, but these do not substantially affect the result.

The fabricated chip utilized several tapers to optimize cavity performance. For input coupling, a wide taper of 10 μm width was used, which was brought down to the nominal width of 1 μm for the DBR portion. After the DBR, it was tapered to up to 3 μm for the internal portion of the cavity for 5 mm total length, then brought down to 1 μm again for the outer grating. Finally, it was brought up to the 10 μm outer width for out-coupling. In this way, high-quality grating operation is ensured, while maintaining low scattering losses thanks to the moderate waveguide width in the

cavity region. A schematic of the cavity design approach is provided in Fig. 7.5.

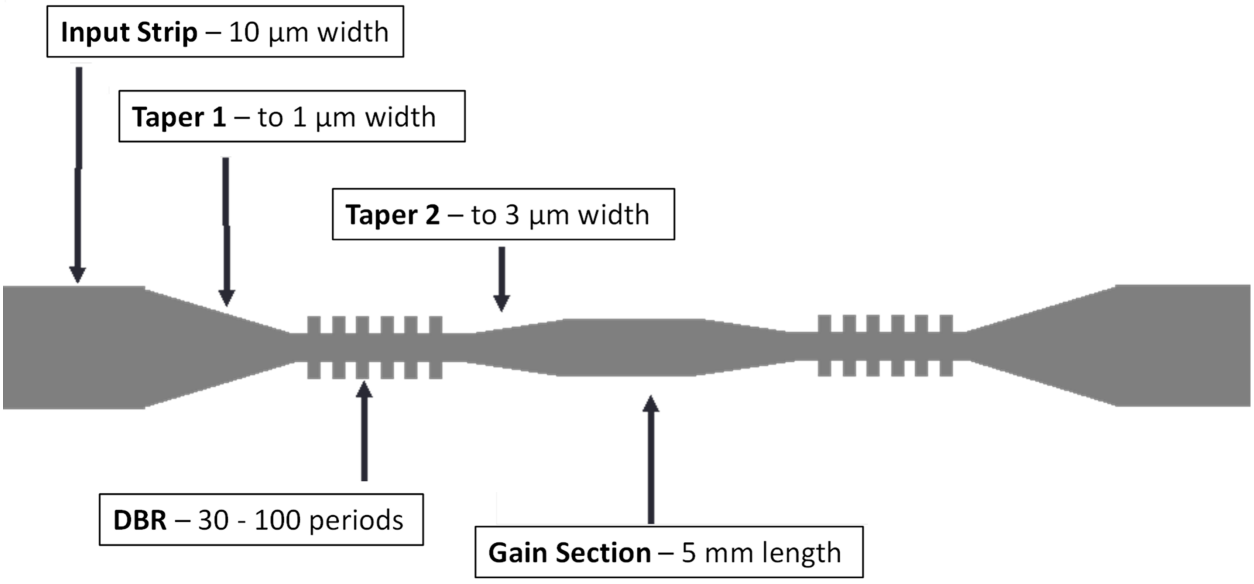

Figure 7.5: Integrated Raman laser cavity design, employing DBR-type mirrors.

A sample was fabricated following this design, however, catastrophic failure occurred at the beginning of the input-side 1-μm-width section, indicating that the intensity had exceeded the internal damage threshold. This sensitivity may have been due to parasitic absorption in the waveguides or material defects. Further work could include a more comprehensive assessment of the loss factors and examination of possible coatings to passivate the waveguide surfaces.

In conclusion of this section, the design and fabrication of integrated laser cavities for mid-IR silicon Raman lasers has been explored. With improvements to fabrication and processing techniques, and more sensitive measurement equipment, it is likely that high-quality devices could be realized in the near future. Once the concept has been verified on inexpensive substrates such as SOI, it can be readily adapted to more advanced and flexible platform such as ASOP, opening the door for broadband frequency conversion to be achieved at much longer wavelengths.

7.2 The augmented all-silicon optical platform

The ASOP platform, presented in Chapter 3, offers numerous benefits for the field of mid-IR integrated photonics. A promising variation on the technology, the *T*-Guide, was introduced later in Chapter 4. In fact, these two approaches are compatible with each other, and indeed provide complementary benefits. In this section, further refinements on each approach, as well as strategies for their mutual integration, will be discussed.

7.2.1 "Notched" T-Guide geometry

As discussed earlier, the *T*-Guide geometry naturally tends toward single-mode and single-polarization operation over broad bandwidths. For some applications, these characteristics are not as critical, or it may also be desirable to have both polarizations propagated. With this in mind, we have also explored a variation on the T-geometry, the notched-T which is shown in Fig. 7.6.

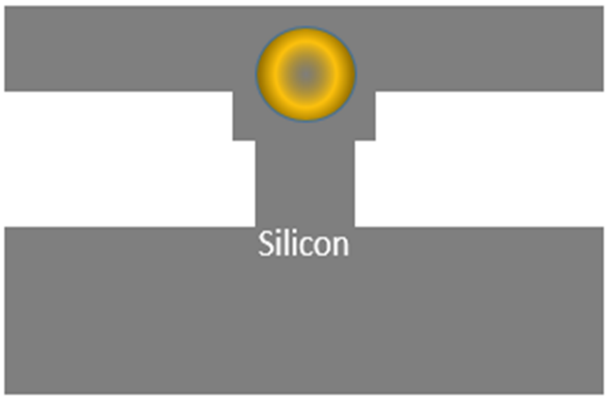

Figure 7.6: Cross-sectional view of the notched *T*-Guide geometry. The rough position of the optical mode is indicated by the bright dot in the middle.

Essentially, it is a narrowing of the post width that is applied somewhat above the position of

the optical mode. In effect, this provides an additional index contrast in the vertical direction, preventing excessive leakage into the substrate through that path. This also acts to strongly confine the TM mode, extending the spectral window for which it can be propagated in a T-Guide. This enables wider post widths to be used without increasing the post height to an impractical value.

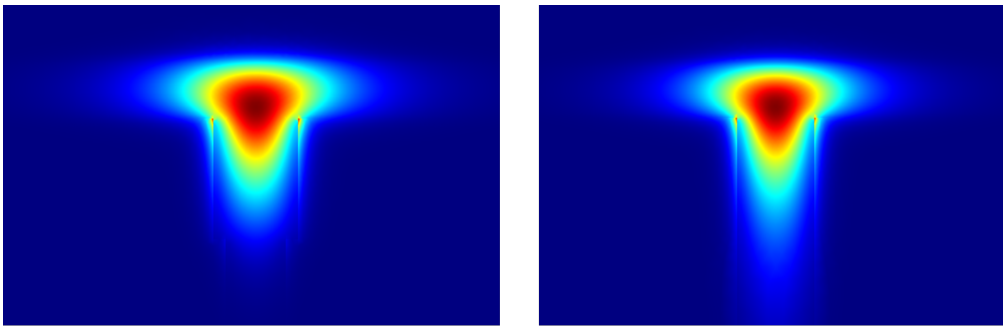

Figure 7.7: Comparison of the TE-mode normalized electric field profile for the (a) conventional T-Guide geometry and (b) the notched T-Guide geometry.

This is best demonstrated in Fig. 7.7, which provides a comparison between T-Guides with and without the notching. The slab thickness was fixed at 500 nm, the post width was varied between 300 - 700 nm, the notching depth applied was 50 nm on each side (100 nm total width reduction in the post), and the notching was chosen to start 800 nm above the slab interface. Simulations were conducted for λ = 1.55 μm. A marked change in the vertical extent of the mode is observed between the two cases, showing that the notch can improve the confinement in this direction. It is also notable that the TM mode is fully supported at w = 700 nm in the notched case, which would be impossible for the conventional T-Guide design with such dimensions. Another outcome of the notched-T geometry is an improvement in the bending radius which can be achieved for these structures. This is possible because wider posts can be used without introducing post-substrate leakage loss. This could be advantageous for applications that require compact bends,

e.g. for spiral waveguide patterns to create long optical paths on-chip. It should be noted that the introduction of notching may allow the propagation of higher-order modes, since more than one field lobe can now experience a local increase to the effective index at the junction area. Whether or not higher order modes are permitted depends on the extent of the notching that is applied. Examples of some fabricated notched-T waveguide cross sections are available in Fig. 7.8. A clear transition from the wider core area to the narrower section of the post can be observed in both cases. The full details on the fabrication technique employed to achieve the notched-T geometry are available in Appendix A.4.

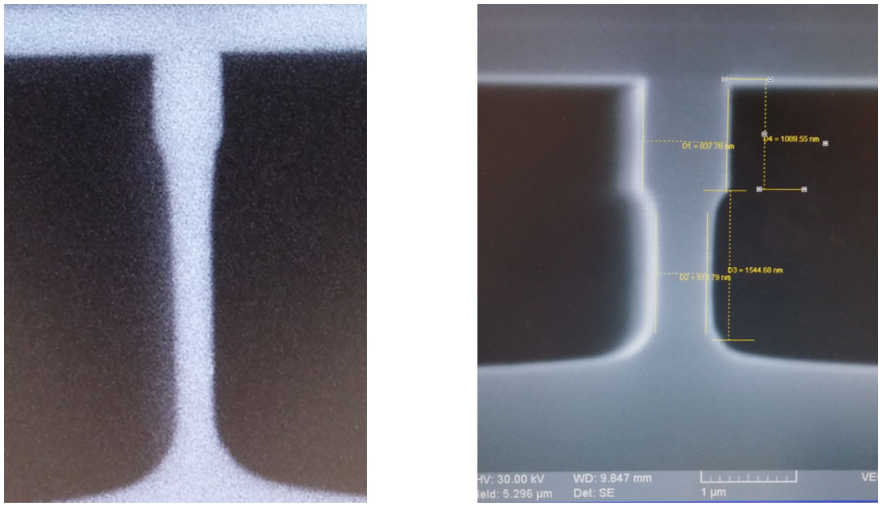

Figure 7.8: Examples of notched *T*-Guides fabricated with varying dimensions. (a) High-aspect ratio design; (b) notching applied to a shorter post.

7.2.2 Loss reduction of T-Guides via oxidation and planarization

The current *T*-Guide fabrication process already achieves reasonably low losses. However, there is the potential for reducing these losses even further. Primarily, the waveguide propagation loss

in *T*-Guides is due to the roughness of the etched sidewalls. Although care was taken to optimize the plasma etching recipes to reduce this, it is an inevitable byproduct of silicon etching. A small amount of thermal oxidation was used in the initial demonstration to reduce the severity of this roughness, followed by wet etching to remove the lossy silicon dioxide. However, more extensive thermal oxidation generally results in rounded corners, due to the diffusion gradients and the viscous flow of silicon dioxide at high temperatures [115]. An example of a *T*-Guide post which has been rounded by extensive thermal oxidation is shown in Fig. 7.9.

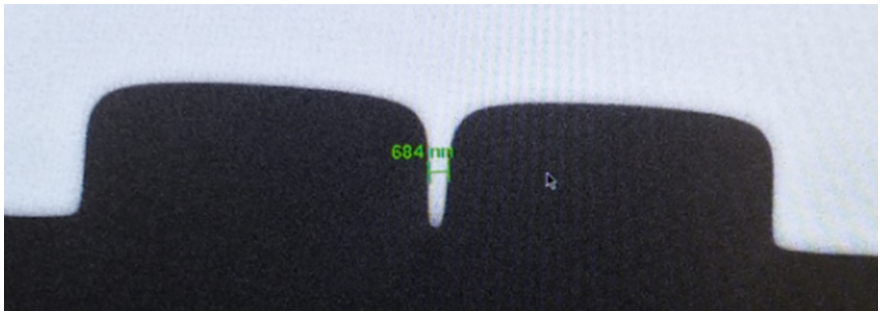

Figure 7.9: Trenches and the post on the handle wafer after over-oxidation and removal of the oxide. The silicon features are white, and the dark areas are air.

The top of the post is no longer level with that of the surrounding substrate; as a result, the slab is not in contact with the post after bonding and no waveguiding would occur. In a less severe instance, the post would have rounded corners even though it could successfully bond with a portion of the slab. Nevertheless, even a small degree of rounding (such as a 100 nm bite off the top of the post, as shown in Fig. 7.10) can result in significant deterioration of the guiding effect, as it decouples the post from the slab. The mode visibly widens in both the slab and post areas due to the weaker guiding effect.

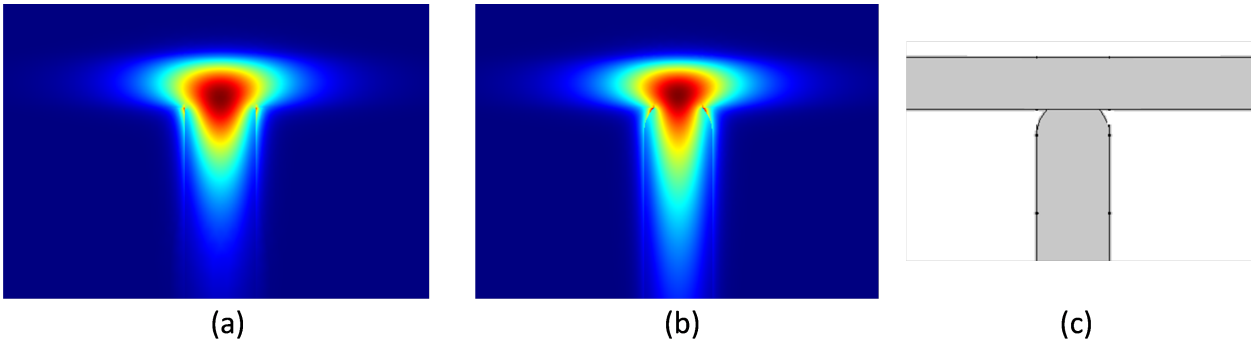

Figure 7.10: The effect of rounded post corners on waveguiding in T-Guides; the normalized TE electric field profiles for the modes are shown for (a) conventional, rectangular T-Guide; (b) T-Guide with $\sim$ 100 nm rounded corners. In (c), the truncated geometry is displayed showing the rounded post.

As such, it is desirable to be able to use thermal oxidation to smooth out etched sidewall roughness, but still retain the strict rectangular geometry inherent to the features of a T-Guide. We propose a simple and reliable method to address this:

1. Thermal oxidation of the silicon posts

2. Chemical mechanical planarization of the surface to remove the rounded features on top

3. Removal of the remaining thermal oxide

These steps are shown in Fig. 7.11. The advantage of this approach is that a large depth of oxidation can be applied, while still being able to recover the intended rectangular geometry thanks to the use of chemical-mechanical-planarization (CMP). For conventional ridge waveguides or channel waveguides, this is not possible since the entire shape undergoes rounding and only the top surface could be polished flat. Thus, T-Guides offer a unique opportunity to obtain high-performance membrane waveguides that could attain extremely low propagation losses. This technique could be invaluable for applications such as on-chip supercontinuum generation, where tight geometrical

control and ultra-low losses are paramount. Alternatively, it could enable a new approach for planar lightwave circuits (PLCs) fabricated at low cost when using silicon dioxide as the core material [116].

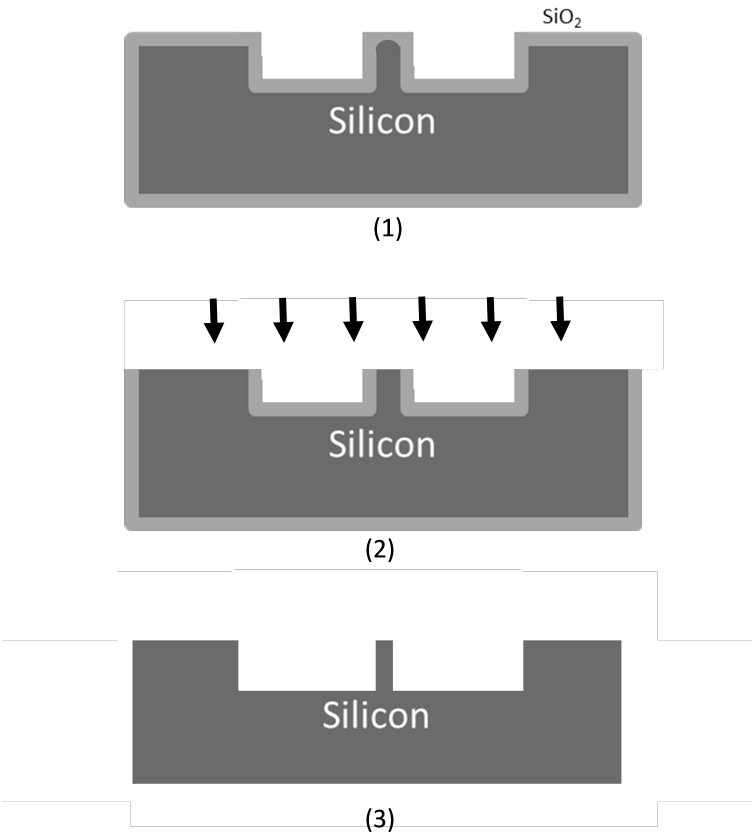

Figure 7.11: Process for reducing propagation losses in *T*-Guides, taking advantage of extensive thermal oxidation followed by surface planarization to restore the intended geometry.

7.2.3 Advanced fabrication and design for ASOP

In the fabrication of the waveguides for the previous supercontinuum generation experiment, contact-based optical lithography was employed for defining both the handle-wafer trenches as well as the

ridge waveguide features on the suspended membranes. Although this has the advantage of only requiring low-cost fabrication equipment, it does not give the best performance. It is limited to a typical alignment accuracy of $\pm$ 2 μm, depending on the equipment available. For substrates with defects, this could be worse due to the tendency for samples to stick to the optical mask during alignment. For the ASOP process, this alignment error necessitates larger-than-required suspended membrane widths in order to guarantee that the ridge is sufficiently far from the substrate on either side to prevent leakage. In turn, the wider suspended portions place some limit on how deep the etch can be performed without compromising the mechanical stability. This limits the degree of flexibility for dispersion engineering in an application such as supercontinuum generation.

A superior method would be to employ non-contact lithography to pattern the wafers, making use of steppers and/or electron beam lithography systems with machine vision tools to perform automatic pattern recognition-based alignment. Such systems can readily achieve alignment errors well below $\pm$ 500 nm, which would allow the suspended membrane width in an ASOP waveguide to be dramatically reduced. Consequently, the etch depth applied to the membrane could be increased drastically, enabling channel-like waveguides suspended by extremely thin membranes no more than 100 nm thick. In this sense, ASOP enables the ultimate index contrast by leveraging a practically perfect interface between silicon and air on all its sides.

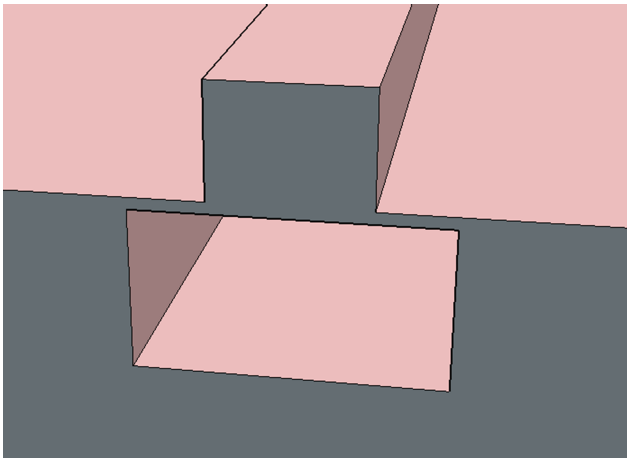

Figure 7.12: Envisioned quasi-channel waveguide enabled by the dimensional freedom and stability provided by ASOP.

Such a design is envisioned in Fig. 7.12, with a waveguide width of 1 μm, height of 800 nm, and a residual slab thickness of $\sim$ 75 nm. A total trench width of $\sim$ 2 μm is shown. Such a design is only possible with the ASOP approach, as compared to undercut-etched suspended membranes, thanks to the free choice of trench parameters provided in the process.

7.2.4 Hybrid integration of ASOP and T-Guide photonics

Another intriguing possibility for *T*-Guides is the eventual co-integration with ASOP-style photonics. *T*-Guides could be used for ultra-low-loss and high-beam-quality propagation, while the ridge ASOP waveguides provide more compact integration for routing. This is possible because a chip that is fabricated for *T*-Guides can support ASOP waveguides by simply adding another lithography and etching step after normal processing. But how can a smooth transition between these modes be realized? Consider a *T*-Guide and an ASOP waveguide which have comparable dimensions. These represent the starting and ending points of the transition between ASOP and

T-Guide. Somewhere in between, the mode becomes a hybrid of these states, which in this case is essentially the juxtaposition of those two geometries. Fig. 7.13 shows these three cases of ASOP, T-Guide and hybrid.

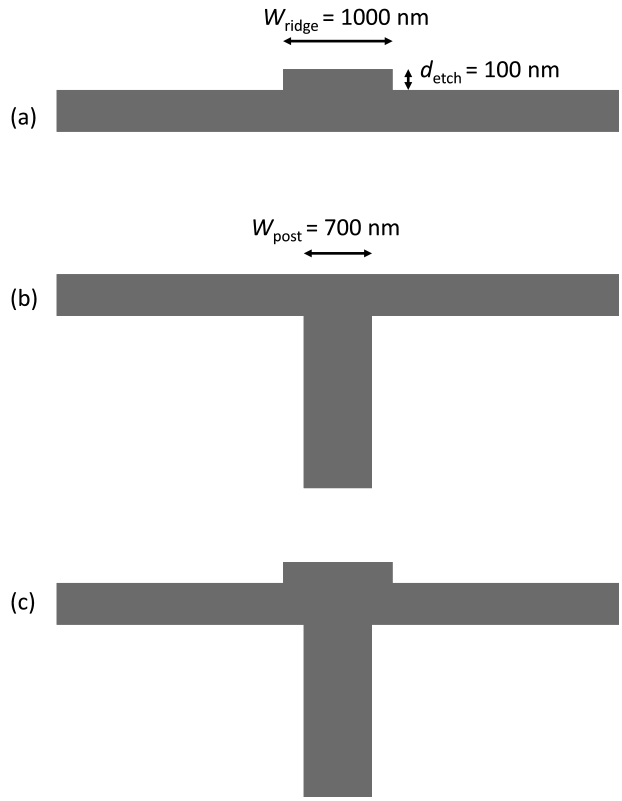

Figure 7.13: Dimensions for waveguides considered for conversion between the T-Guide and ASOP geometries; (a) ASOP, (b) T-Guide, and (c) hybrid.

In the hybrid state, one can convert to a pure T-guide by gradually increasing the width of the ridge feature in the ASOP waveguide until it is simply the un-etched slab. Similarly, to convert to a pure ASOP waveguide, the post feature needs to be gradually narrowed until it disappears, at which point the energy has been transformed to the eigenmode of the ASOP ridge waveguide. The transformation of the optical mode from the hybrid state to the ASOP state is shown in Fig. 7.14. As the post decreases in size, the mode broadens to match the natural profile of the ASOP

waveguide.

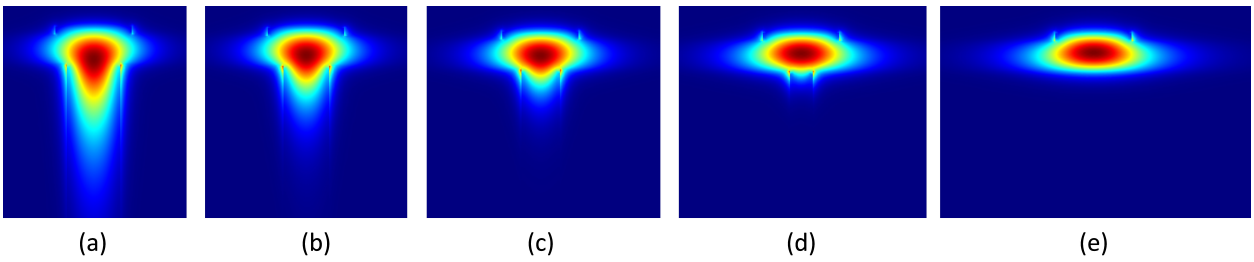

Figure 7.14: Transition from the hybrid waveguide to the pure ASOP ridge waveguide, showing the evolution of the normalized electric field profile of the TE mode: (a) hybrid state with w = 700 nm; (b) w = 600 nm; (c) w = 500 nm; (d) w = 300 nm; (e) post completely removed.

In practice, this transition would be simple to realize with a simple linear taper-down of the post width over a short distance. This could allow the mode to be converted to a more diffraction-limited profile for efficient coupling off the chip.

7.3 Novel techniques for quasi-phase-matching on integrated photonics

Achieving power-efficient frequency conversion in integrated photonics is a challenging but extremely promising pursuit, with the hope of converting cheaply available optical energy to more exotic frequencies in a compact and mass-manufacturable form-factor. This pursuit brings many challenges, arguably the most significant of which is the need for a robust, flexible and accurate means of achieving quasi-phase-matching between the involved optical frequencies.

We will consider the case of second harmonic generation to elucidate the situation. The relevant conservation relations are provided in Eq. 7.1 below [117]:

$$\Delta k = 2k_p - k_s \tag{7.1}$$

$$\omega_s = 2\omega_p \tag{7.2}$$

Where k is the wavenumber inside the medium and ω is the optical frequency, with subscript *p* denoting the pump and *s* the signal or second-harmonic wave. In a fictitious optical medium with negligible dispersion of the refractive index, momentum conservation is automatically satisfied for the case of co-propagating pump and signal waves, and the situation is trivial. In reality, all optical media display some degree of dispersion, resulting in a momentum mismatch between the two waves. In effect, the generated signal wave will undergo a periodic reversal with a coherence length dictated by the degree of momentum mismatch as follows:

$$L_{coh} = 2/\Delta k \tag{7.3}$$

Thus, it is necessary to reduce the momentum mismatch to as small a value as possible, to maximize the usable nonlinear length. Some method of compensating this mismatch is required to effectively utilize the nonlinearity of the material for a longer distance (which will usually result in much higher conversion efficiencies). This is possible in bulk media (the most common approach for nonlinear optical systems these days) through various means, such as birefringent phase matching, or the use of crossed beams, the angle of which can be adjusted to achieve momentum conservation [117].

Alternatively, certain materials such as lithium niobate ($LiNbO_3$) are amenable to techniques such as periodic poling, in which the orientation of the crystal domains is periodically reversed, allowing the phase mismatch to be compensated over an arbitrary distance [22]. Such techniques are referred to as quasi-phase-matching (QPM). Similarly, the domains of semiconductor crystals can be grown in an alternating sequence, as in the orientation-patterned GaAs approach [23]. Still, bulk optical systems suffer from limited useful nonlinear interaction lengths due to the diffraction of the beams

or from walk-off angles. The peak intensity is constrained from the same issue, as a larger beam waist is required to forestall the expansion of the focused beam.

With these issues in mind, the use of integrated photonics for nonlinear frequency conversion is a burgeoning field of research. In principle, an integrated platform could enable high optical intensities thanks to the small mode area of the waveguides, long propagation lengths from the waveguiding effect, and co-integrated optical devices such as filters, splitters, and modulators which may be necessary depending on the application. Being able to simultaneously fabricate them on the same chip could enormously simplify the replication of these systems. However, integrated platforms too must address the issue of momentum conservation. Additionally, due to the contributions of waveguide dispersion (which can be stronger than material dispersion in some cases), the magnitude of the mismatch is usually much worse. In a waveguided situation, it can simply be stated that phase-matching and momentum conservation are achieved for second-harmonic generation when $n_{eff,p} = n_{eff,s}$. Fortunately, the unique fabrication and processing techniques available in planar systems have enabled several possible solutions. One approach is to utilize a higher-order mode at the second harmonic wavelength, which can have a substantially lower effective index than that of the fundamental [118, 119]. By applying the proper design for the geometry of the waveguide and selecting the right mode, it is possible to find a crossing point at which the effective index of the fundamental mode of the pump is equal to the specific mode chosen at the harmonic. If the fabrication is reliable and controllable, this provides a relatively simple way to achieve phase-matched second harmonic generation without complicated post-processing, and it can be applied to almost any material system. But it is not without its drawbacks. In the process of second harmonic generation, the degree of overlap between the pump and harmonic waves has a significant impact on the efficiency of the process. In non-resonant, bulk optical systems, this is usually not an issue, making it a unique challenge for waveguided systems. By using a higher order mode, the degree of overlap can be severely impacted since the lobes of opposite sign will partially cancel

out the contribution of the center lobe [120]. As such, the effective strength of the nonlinearity may be much lower than the bulk value. Arguably, this negates the benefit of the small mode area, since the greater intensities may just compensate for this problem. A promising alternative means of quasi-phase-matching that is still applicable to integrated platforms is periodic poling. In the $LiNbO_3$ material system, diffused optical waveguides have been fabricated on periodically poled substrates, yielding efficient optical parametric oscillators [121]. However, this platform does not yield compact waveguides, making it difficult to co-integrate several devices without consuming excessive chip area. Alternatively, the thin-film lithium niobate on silicon platform, developed by our research group, provides compact waveguiding on a substrate compatible with conventional processing techniques [122]. This platform consists of a thin (sub-μm) film of $LiNbO_3$ transferred onto an oxidized silicon wafer. Ridge waveguides are achieved by depositing and etching a rib-loading feature on top of the $LiNbO_3$, consisting of a material with suitable refractive index. A novel technique for periodic poling was applied by our group to this platform, resulting in highly efficient second-harmonic generation in μm-sized waveguides [rao shg ref]. The periodicity of the grating can be easily varied and potentially brought to very small periods, enabling harmonic generation well into the visible spectrum.

Unfortunately, periodic poling is a technique that is applicable only to a select few nonlinear optical materials. The technique is not suitable for GaAs crystals, which exhibit extremely large nonlinear coefficients (such as the d_{14} element with a value of 90 pm/V) and have a broad transparency range into the far-infrared [23]. Additionally, OP-GaAs technology is not readily suitable for sub-μm scale waveguide integration. Some other means of QPM must then be found to enable high-performance nonlinear frequency conversion on this and other similar material systems.

An intriguing but little-explored alternative was proposed by Huang et al. in 1998 [123], dubbed intensity-modulation QPM. In this approach, two parallel waveguides were designed such that the pump light would periodically decouple from that of the second harmonic light being generated.

This could be controlled by the gap between the waveguides. In this way, the generation of light would be most efficient when they pump and signal are in-phase, and would be prevented when they are out-of-phase. It places no processing constraints on the material to be used, which is highly valuable. Since the light is only generated half of the time, however, it is not as efficient as periodic poling. Experimental studies on this approach did not achieve promising results, reaching a maximum normalized conversion efficiency of only 1.6 $W^{-1}cm^{-2}$ [124]. Most likely, the greatest difficulty was in achieving the precise phase matching constraints demanded by the approach.

The notion of employing a periodic variation of the pump intensity for QPM is still worthy of consideration. Considering the practical difficulties with the prior approach, it would be prudent to implement some scheme which does not depend on precisely engineered coupling constants, resonant effects or critical geometrical relations. Instead, I propose a novel approach, which will be deemed mode size modulation (MSM). In this method, an optical waveguide undergoes a periodic variation in its width, the length of which corresponds to the coherence length dictated by phase matching considerations. As a result of the width variation, the optical mode of the pump wave experiences a modulation of both its size and shape during propagation through the waveguide. As it expands to follow a widening waveguide, the intensity of the mode decreases. Since the efficiency of the second harmonic generation process is directly related to the intensity of the pump wave, QPM is achieved by this periodic change in efficiency. For simplicity, and to avoid optical losses from any abrupt transitions, a sinusoidal width variation pattern has been adopted. This scheme is shown in Fig. 7.15, where a thin slab of material is loaded to become a ridge waveguide with a sinusoidally varying pattern.

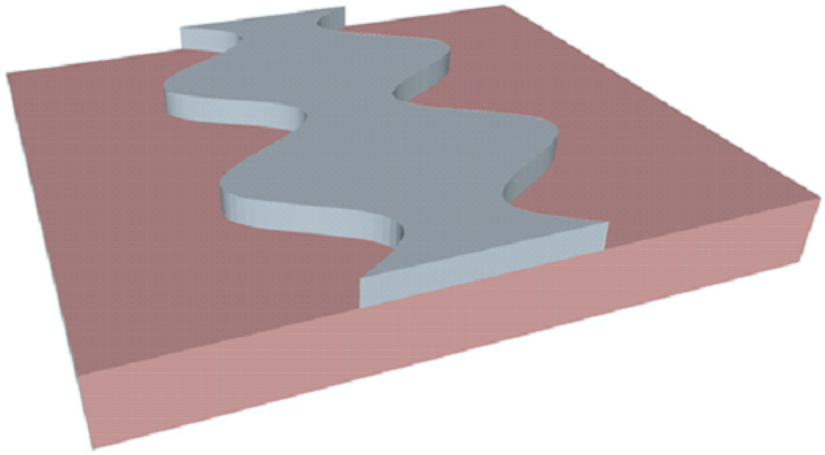

Figure 7.15: MSM ridge waveguide, showing the longitudinally varied waveguide width following a sinusoidal pattern (exaggerated in its magnitude for visibility).

Coupled-amplitude equations can be used to describe the process of second harmonic generation in waveguides. The general relations are given below:

$$dA_p/dz = -\alpha_p A_p/2 + A_s A_p^* e^{-i\Delta kz} 2i\omega_p^2 d_{eff}/k_p c^2 \tag{7.4}$$

$$dA_s/dz = -\alpha_s A_s/2 + A_p^2 e^{i\Delta kz} 2i\omega_p^2 d_{eff}/k_s c^2 \tag{7.5}$$

Where A is the wave amplitude, z is the distance in the propagation axis, a is the propagation loss, w is the optical frequency, d_{eff} is the effective nonlinear coefficient in use, k is the wavevector, c is the speed of light, and Δk is the momentum difference given by Eq. 7.1. The subscripts p and s denote applicability to the pump or signal, respectively. In order to adapt these equations for the case of MSM, the pumps intensity variation must be taken into account. To a first order approxi-

mation, the pump intensity will follow a sinusoidal variation, offset by some average intensity, in good agreement to the geometrical variation imposed on it. A numerical function which encapsulates this variation in amplitude resulting from the mode size modulation, referred to as F(z), was incorporated into the pump wave coupled-amplitude equation as below:

$$dA_p/dz = A_p F(z) - \alpha_p A_p/2 + A_s A_p^* e^{-i\Delta kz} 2i\omega_p^2 d_{eff}/k_p c^2 \tag{7.6}$$

This reflects the apparent perturbation to the pump wave amplitude experienced by the signal wave as it propagates in the z direction. Importantly, it does so while conserving the average power of the pump, to preserve a fair comparison of conversion efficiency. The variation in signal amplitude was not incorporated, as the conversion efficiency does not depend on the signal amplitude in the case of negligible pump depletion. The signal amplitude variation may also be much smaller in magnitude than that of the pump due to the linear scaling of diffraction effects with wavelength.

Next, the simulation parameters were established, with the goal of finding a comparison between the performance of MSM and periodically-poled QPM techniques. The thin-film $LiNbO_3$ material system (X-cut orientation) was selected for this purpose. A pump wavelength of 1550 nm was assumed, giving rise to a second harmonic signal at 775 nm. Only the TE modes were considered, which results in the d_{33} element of the nonlinear susceptibility tensor (30 pm/V) being used. The effective coefficient used was 14 pm/V, after adjustment to consider the overlap integrals of the modes with each other and the lithium niobate slab. The waveguides were of a ridge waveguide form, with the ridge element consisting of $Ge_{23}Sb_7S_{70}$ chalcogenide glass, with a refractive index of roughly 2.3 (although the full dispersion behavior is included for all materials). For the MSM structure, a maximum and minimum width of 2000 and 1000 nm were used, respectively. The ridge element was 150 nm thick, and the slab was 400 nm thick. An air cladding on top was assumed, with a bottom cladding of silicon dioxide sufficiently thick to prevent leakage to the silicon

substrate underneath. A grating periodicity of 3 μm was assumed which correctly compensates the momentum mismatch between the pump and signal waves, whose effective indices were determined by eigenmode simulations in COMSOL. The effectiveness of MSM for QPM depends strongly on the degree of intensity variation that is achieved by the grating, so simulations were conducted to determine the effective mode area at both extremes of the grating width. As seen in Fig. 7.16, the mode expands when the ridge is widened. The maximum variation in intensity that can be achieved in this configuration is 35 %.

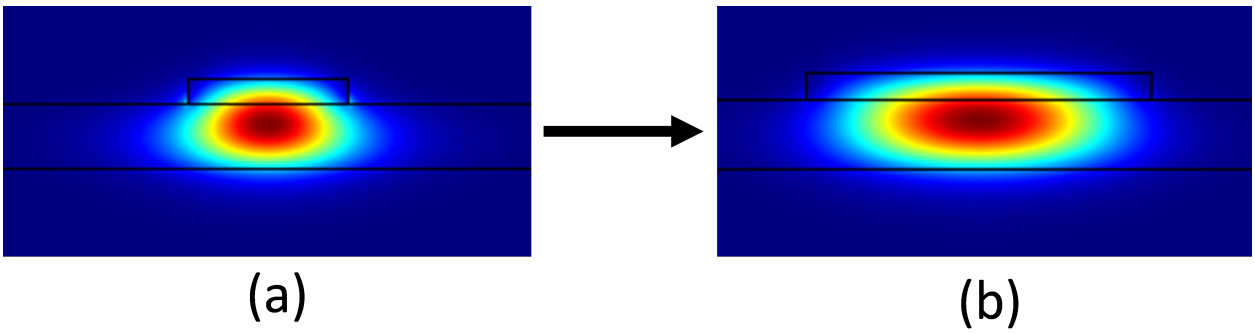

Figure 7.16: When the ridge-loading element is widened from 1 to 2 μm, the mode area increases.

Both the case of MSM-QPM as well as periodically poled QPM will be compared in the numerical study. The intensity of the input light was determined by fixing the input power and dividing by the effective mode area. For the MSM case, the size of the mode at its minimum width was used, giving a mode area of 0.4 um^2. For the PP case, the same value was used. The PP effective nonlinear coefficient was 9.1 pm/V, based on overlap and fabrication consideration. A power of 50 mW chosen to be coupled into each waveguide, initially, and loss values of 3 dB/cm were included for both the pump and signal to allow for grating-induced or material losses. In both cases, a total propagation length of 3 cm was simulated, but the efficiency figure was chosen from the optimal point along the curve. The initial conditions and coupled amplitude equations (Eqs. 7.6, 7.5 and

7.1 for MSM and 7.4, 7.5 and 7.1 for PP-QPM) were incorporated into an ordinary differential equation solver in MATLAB. Both solutions are plotted in Fig. 7.17.

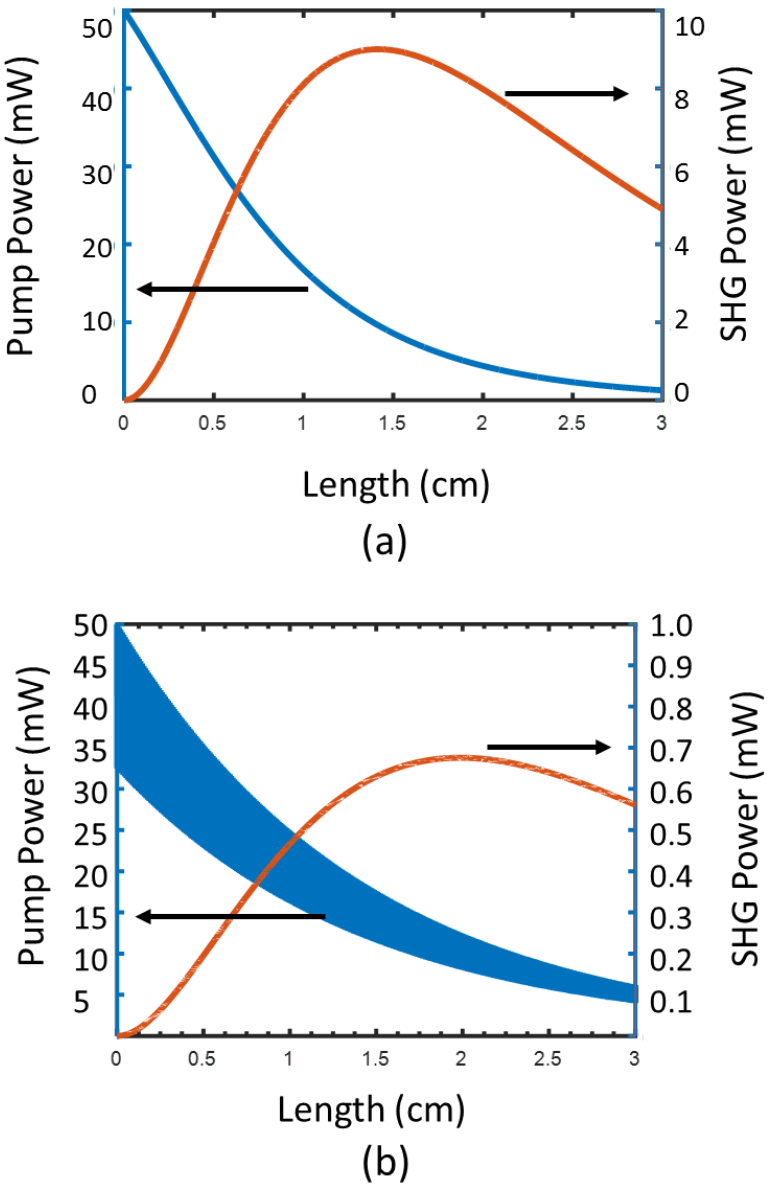

Figure 7.17: Numerical solution for the coupled amplitude equations for the (a) PP-QPM case, showing the pump power (left axis) and generated second harmonic power (right axis), and (b) MSM-QPM case.

In the case of PP-QPM, a peak conversion efficiency of 18 % was achieved at an optimal length of 1.4 cm. For MSM-QPM, the peak conversion efficiency was 1.4 % at an optimal length of 2 cm. Under these circumstances, it is roughly 8 % as efficient as PP-QPM. The large decrease in conversion efficiency is a result of the back-conversion that occurs when the signal is out-of-phase with the pump. Because only 35 % variation in achieved in the pump intensity, this is only partly suppressed. With a larger variation in the intensity modulation, the effect could be enhanced significantly. Another factor to consider is the modulation of the overlap integral between the pump and signal waves that occurs simultaneously with the modulation in mode size. The two waves experience different degrees of expansion and contraction inside the grating, and in the case of a diminished overlap integral during the wider width portion, this can potentially help suppress the back-conversion, and increase the overall conversion efficiency. Additionally, it should also be noted that with lower losses, MSM-QPM can still provide a reasonable means of achieving similar conversion efficiencies in the regime of high pump depletion, albeit with longer lengths. Because of this, MSM-QPM may find application in material systems where PP-QPM is not possible.

7.4 Conclusion

Integrated photonics is a technological pursuit that started many decades ago, in the technological revolution of the mid-20th century. Since the beginning, it was the obvious need to scale down and merge photonic technologies that drove its progress. While many foundational elements were envisioned in the early days, it has been the steady accumulation of techniques, apparatuses and clever tricks that put the field where it is now - at the brink of a new phase of rapid development. Although just a few platforms and processes have dominated the focus of research over the past decade, they do not necessarily represent the course of the future. It was the goal of this dissertation to seek out and develop new technologies for integrated photonics, making use of hybrid material

systems that would enable new functionality for burgeoning applications. Several platforms were investigated to this end, such as ASOP, T-Guides, SiLN and TAP. A unifying theme to come out of these works is the access to unprecedented optical bandwidths through transparency or unique waveguiding techniques, for physical optical applications such as remote sensing. In the near future, these platforms may seed new paths of development for the field as a whole.

APPENDIX A: FABRICATION METHODOLOGY

In the main body of this dissertation, multiple new photonic technologies have been discussed, with the emphasis more on design and testing rather than their fabrication. In this section of the appendix, the specific techniques involved in their fabrication will be discussed in greater detail. It is subdivided by project to allow accurate replication of each technology. Certain equipment-specific recipes are separately detailed in Appendix B.

A.1 Silicon-on-Lithium-Niobate (SiLN)

A.1.1 SiLN die preparation (wet-backside-etching method)

This procedure describes the preparation of SiLN dies (via manual bonding) for later processing. The expected die size should be roughly 2 x 2 cm^2 for hand-cleaved LN dies, which may be subject to failure from microcrack-initiated stresses at the peak annealing temperature. With ground and polished wafers, the sample size may be substantially larger.

Supplies required: 1. Lithium niobate wafer (X- or Y-cut, CMP polished on one or two sides, $>$ 50mm diameter)

2. SOI wafer - device layer thickness 220 nm, $>$ 10 ohm·cm resistivity, $>$ 2 μm BOX thickness, $>$50 mm diameter, thermal oxide should be removed from the backside of the wafer prior to processing.

3. Conventional photoresist

4. Apiezon W Black Wax

5. 70% HNO_3, 50% HF, deionized water

6. Toluene

Procedure:

1. Coat the lithium niobate and SOI wafers each in a thick layer of any photoresist and bake until solid. This acts to preserve surface cleanliness during initial processing.

2. Cleave or dice the SOI wafer into roughly 20 x 20 mm dies.

3. Cleave or dice the LN wafer into roughly 25 x 25 mm dies (should be slightly larger than the SOI dies, regardless of the specific dimension).

4. Select one SOI and one LN die.

5. Clean them in an ultrasonically agitated mixture of equal parts acetone, isopropanol, and deionized water.

6. Rinse each die in same solvents and dry with nitrogen.

7. Perform surface activation via Recipe B.4.

8. Perform a quick nitrogen spray across the surface to remove any debris accumulated during handling.

9. Place the SOI die on a clean, hard and flat surface such as an old photomask.

10. Arrange stops slightly taller than the SOI die around it, so as to prevent the LN die from sliding off later.

11. Invert the LN die and contact it to the SOI die, keeping them as parallel as possible.

12. Tap the center of the LN die with the blunt end of a tweezer to initiate bonding. With proper surface activation and cleanliness, a bond-wave will visibly and very quickly propagate out from the point of contact, encompassing most of the surface area.

13. Tap the remaining unbonded areas in an outward pattern to drive air gaps out, where possible.

14. Place on a hotplate and slowly ramp the temperature up to 100°C over a period of 10 minutes, then hold at this temperature for another 15 minutes.

15. Ramp the temperature up to 170°C over 10 minutes, then hold for a period of 36 hours; this annealing step further increases the bond energy to prevent de-bonding under liquid immersion.

16. After this period, slowly ramp the sample down to 110°C over 10 minutes.

17. Flip the sample upside-down such that the SOI backside is now facing upward.

18. Apply Apiezon W Black Wax to the edge of the SOI die, such that the interface becomes fully sealed. Avoid contact with the top surface of the SOI die.

19. Ramp the sample down to room temperature over 10 minutes.

20. The following several steps involve the preparation of an extremely dangerous acid solution; all such steps should be conducted inside a fume hood and only with proper safety training and personal protective equipment. Never place your hands close to the etchant solution or any of its ingredients!

21. Prepare an HNA solution of at least 500 mL in an acid-safe beaker with the following proportions: 50:37:17 HNO_3:HF:H_2O (volume ratios). HNO_3 should have 70% concentration, and HF should have 50% concentration. Stir thoroughly and let stand for 20 minutes to let cool to roughly room temperature.

22. Prepare separately a large plastic beaker with deionized water for rinsing.

23. Place the bonded and annealed SOI/LN sample in the HNA etchant and agitate thoroughly during etching. Insufficient or uneven agitation will result in a curved etch profile, resulting in

premature exposure of the edges compared to the middle, and subsequent surface damage. Use a PTFE or PP plastic fixture to manipulate the sample at a safe distance from the beaker.

24. The etch rate should proceed at roughly 20 μm/minute, though it will vary substantially based on the doping level of the backside silicon on the SOI die, the agitation rate, and the temperature. The goal is to reach the buried oxide (BOX) layer at a similar time across the surface. Since HF etches buried oxide, there is a limited window over which it will protect the silicon layer underneath before punching through and destroying it. The etch rate of BOX in this solution is roughly 500 nm/min. Remove the sample and inspect periodically to keep track of its progress.

25. If the solution heats above 40°C, the black wax will begin to degrade rapidly, resulting in undercut of the solution. Do not continue etching if the solution heats excessively. This can be mitigated by cycling out the solution with fresh HNA etchant at room temperature, then continuing.

26. Once the center of the sample appears smooth, flat and shiny, the silicon backside has been removed. At this point, the sample should be rinsed in deionized water.

27. Dry the sample thoroughly with nitrogen.

28. Anneal on a hotplate at 130°C for 1 hour.

29. Remove the SiLN die from the black wax, using toluene or o-xylene to dissolve it, followed by IPA rinsing to remove residues.

30. Anneal on a hotplate at 250°C for 2 hours, using a 10 minute ramp up to temperature.

31. Let cool, then dip in buffered oxide etchant for an appropriate amount of time based on its given etch rate in order to remove the BOX layer on top of the silicon.

32. Rinse in deionized water and dry. The SiLN die is now fully prepared for further processing.

Be sure to inspect the surface to confirm that there are no silicon islands remaining which may cause issues later. For non-contact lithography methods, however, these should not cause any issues other than a reduction in usable area.

It should be noted that the technique using wet etching, comprising steps 18-29, is not the only means of backside-removal (BSR) that can be used to prepare SiLN dies. Dry etching techniques, such as that described later in Appendix B, Recipes B.9-10, can also achieve the same result, with the advantage that the die need not be exposed to any liquids after bonding. The initial anneal may not be necessary if dry etching techniques are used. Instead, the sample could be annealed at higher temperatures after BSR, which avoids the high stresses normally encountered with whole dies.

A.1.2 SiLN Modulator Fabrication

Once the SiLN dies have been prepared, they can be used to achieve a variety of interesting devices. The procedure for fabricating integrated electro-optic SiLN modulators will now be described. This procedure involves multiple steps first is the initial e-beam lithography to define the waveguides and gratings. The first etch is a half-etch. The initial hard-mask is left on the surface to protect the waveguides during the second etch, which removes the remaining silicon in the middle of the chip where the modulators will be placed. The silicon is preserved in the vicinity of the grating couplers, which improves their efficiency. Finally, another lithography step is used to define the electrodes for the modulators via the lift-off process.

Supplies Required:

1. SiLN die

2. Hydrogen silsesquioxane (HSQ) e-beam resist

3. AZ5214E Image-Reversal Photoresist

4. Tetramethylammonium hydroxide 25% in H_2O

Procedure

1. Spin HSQ resist onto sample to achieve 144 nm thickness.

2. Bake for 1 min at the edge of a hotplate set to 180°C.

3. Bake for 4 min at 180°C at the center.

4. Deposit 50 nm gold on top of the HSQ using thermal evaporation. It is critical that it is done with this method and not sputtering or e-beam evaporation, as those can easily expose the resist prematurely.

5. Write pattern with the required dose (used 450 uC/cm^2 in this case)

6. Develop for 1 min in 25% TMAH:H_2O, with rapid agitation. Increase to 3 min for 700 nm thick HSQ.

7. Rinse in H_2O and dry.

8. Etch 120 nm of silicon using Recipe B.6 in an ICP etching system (other recipes are suitable as well).

9. DO NOT remove the HSQ at this point, if a two-zone etch is desired.

10. Use photolithography (Recipe B.18 if image reversal is required) to expose areas in the middle, away from the grating couplers.

11. Perform a brief oxygen clean if necessary to remove any residual photoresist that was not

developed. (Recipe B.5)

12. Etch the remaining silicon with Recipe B.6.

13. Remove photoresist using a soft oxygen clean (Recipe B.5).

14. Remove the HSQ hard-mask using dilute HF (1:10 HF:H_2O). Do not expose to the solution for longer than is necessary.

15. Anneal the clean sample in a wet-oxidation environment (nitrogen bubbled through boiling water) at 400°C for 1.5 hours.

16. Use image reversal photolithography (Recipe B.18) to define openings on the surface for the modulator electrodes.

17. Deposit 20 nm chromium and 216 nm gold via e-beam evaporation (e-beam typically allows low-temperature operation compared to thermal evaporation). Ensure that the sample is oriented perpendicular to the direction of oncoming evaporated matter; this improves the liftoff quality by avoiding coating on the sidewalls of the photoresist.

18. Lift off the undesired material by placing the sample in warm acetone and agitating with an ultrasonic bath for a few seconds.

19. Clean the sample with solvents to remove any flakes or residual organic material.

20. Anneal the metal electrodes with rapid-thermal-annealing (RTA) at 400°C for 30 seconds.

21. Clean the sample with solvents once more to remove any metal flakes which may have peeled up during annealing.

22. The sample is now ready for testing.

A.2 ASOP waveguide fabrication

This section details the steps involved in fabricating waveguides or devices on the ASOP platform. There have been several iterations involved in improving the process, therefore, only the latest and most effective will be included. The process involves several key steps: etching trenches into the handle wafer, bonding and annealing, BSR, waveguide-definition lithography and etching, and cleaving.

Supplies Required:

1. Silicon handle wafer with $>$ 10 ohm·cm resistivity

2. SOI wafer with $>$ 1 μm thick BOX layer, and $>$ 10 ohm·cm device layer resistivity (preferably much higher)

Procedure

1. Coat both wafers in a protective photoresist layer prior to dicing or cleaving.

2. Prepare a cleaved or diced die of appropriate size from the silicon handle wafer.

3. Clean the surface, then coat in an appropriate photoresist for conventional lithography. It should be at least half as thick as the expected trench depth.

4. Open trenches on the surface using photolithography (Recipe B.17 or B.18).

5. Etch trenches onto the die using high-aspect ratio silicon etching (Recipe B.6). The trench depth should be sufficient to prevent leakage from the optical mode in the suspended membrane into the substrate below.

6. Remove the residual photoresist using a combination of oxygen plasma (Recipe B.5) and sol-

vents if necessary.

7. Clean both the SOI die and the silicon handle die in an ultrasonically agitated mixture of equal parts acetone, isopropanol, and deionized water.

8. Rinse each die in same solvents and dry with nitrogen.

9. Perform surface activation via O_2 plasma treatment (Recipe B.3)

10. Perform a quick nitrogen spray across the surface to remove any debris accumulated during handling.

11. Dip each sample in ultra-pure deionized water and dry with nitrogen.

12. Place the handle die on a clean, hard and flat surface such as an old photomask.

13. Arrange stops slightly taller than the handle die around it, so as to prevent the SOI die from sliding off later.

14. Invert the SOI die and contact it to the handle die, keeping them as parallel as possible.

15. Tap the center of the SOI die with the blunt end of a tweezer to initiate bonding.

16. Tap the SOI die in an outward pattern to drive air gaps out.

17. Place on a hotplate and slowly ramp the temperature up to 90°C over a period of 10 minutes, then hold at this temperature for another 15 minutes.

18. Ramp the temperature up to 250°C over 10 minutes, then hold for a period of 30 minutes.

19. Remove from hotplate and anneal in a dry oxygen environment at 1000°C for 1 hour. Load and unload sample slowly to allow it to thermally equalize. If a small amount of oxide formed in the

trenches is unacceptable for the application (such as for long-wavelength operation), the trenches should be sealed and not exposed to air during bonding.

20. Remove from the furnace and let cool.

21. Perform BSR with the dry-etching approach in Recipes B.9 and B.10. Mount the sample on a sapphire handle wafer to prevent punch-through during deep etching.

22. Once most of the smooth BOX surface has been exposed by the etch, remove the sample and blow off any flakes using nitrogen, then resume etching to remove any islands masked by said flakes.

23. Remove the BOX layer using dilute (1:10) HF:H_2O. Do not use BOE; this may cause crystallites to become trapped under the membranes, which can be difficult to remove fully.

24. Perform lithography with Recipe B.17 to produce ridge features over the suspended membranes. For membrane thicknesses of a few microns or less, the location should be clearly visible under microscope examination despite the absorption of silicon.

25. Etch the ridges using Recipe B.6. The maximum permissible etch depth depends on the membrane width and thickness; however, 70% etch depth is safely achieved in most cases. More is possible for narrower membrane widths.

26. Remove the residual photoresist with oxygen cleaning (Recipe B.5).

27. Coat the sample with a thick ($>$ 4 microns thick) layer of photoresist to protect the surface during dicing.

28. Perform partial dicing + cleaving to produce end-facets for coupling in and out of the chip (Recipe B.1).

29. Remove the protective photoresist, and ensure that no residual resist has invaded the trenches. Oxygen cleaning (Recipe B.5) should be used before solvent cleaning, to minimize the amount that enters the trench.

30. The ASOP chip is now ready for testing.

A.3 *T*-Guide fabrication

This procedure is very similar to the one followed for ASOP waveguides. The main difference is simply in the inclusion of a post in the middle of the trench which defines the *T*-Guide. After etching of the handle wafer, additional processing may be applied to reduce the sidewall roughness on the post. To do this, follow Recipe B.2 for thermal-oxidation-based processing. The thermal oxide should be removed, but after this, the handle wafer is suitable for processing identical to that for ASOP (Appendix A.2) through Step 23 of that section.

A.4 Notched-*T*-Guide fabrication

The proposed notched-T structure discussed in Chapter 7, Section 7.2.1 can be fabricated with the following procedure. This procedure can be inserted into the *T*-Guide processing flow, replacing the normal etching procedure used to define trenches:

1. Deposit 700-1500 nm of PECVD SiO_2 (Recipe B.14) to use as an etch mask on the handle die. Do not use thermally grown silicon dioxide, as it sputters and micromasks the exposed surface during etching.

2. Perform lithography (B.17 or e-beam) to define where the posts and trenches will be after etching. Use a polymer mask material such as photoresist or e-beam resist on top of the PECVD

SiO_2.

3. Fully etch the SiO_2 hard mask down to the silicon surface, and overetch by 5-10% to ensure that no residual material remains (Recipe B.11).

4. Remove the polymer mask with soft O_2 cleaning (Recipe B.5).

5. Perform the first stage of post etching (typically 800 1500 nm depth, or sufficiently tall to confine the optical mode in this region) with Recipe B.6.

6. Clean the sample with 2 minutes of soft O_2 cleaning (Recipe B.5) to remove any fluorocarbon contamination on the sidewalls.

7. Deposit 200 nm of PECVD SiO_2 (Recipe B.14), which should cover the sidewalls with roughly half this amount.

8. Use an anisotropic SiO_2 etch (Recipe B.11) to etch through about twice the deposited thickness of SiO_2. The sidewall SiO_2 should remain intact. Ensure that enough of the SiO_2 mask on top of the waveguide will remain after removing this amount.

9. Etch the rest of the post height with Recipe B.6. This should keep in mind the etching selectivity and remaining mask thickness.

10. Isotropically etch the silicon with Recipe B.13 by a small amount. Since the top part of the waveguide and its sidewalls are protected with SiO_2, they will not be etched. However, the substrate and the lower part of the post will be etched, result in the notching effect.

11. Remove the SiO_2 from all surfaces with dilute HF.

12. The handle wafer is then ready for the normal bonding and BSR for any *T*-Guide.

A.5 TAP device fabrication

This section details the process of fabricating a TAP chip suitable for broadband polarization-selective devices.

Supplies needed:

1. Oxidized silicon wafer

Procedure:

1. Cleave the wafer into 2 x 2 cm dies.

2. Deposit alignment markers on the surface with $\sim$ 10 nm Cr and $\sim$ 70 nm Au.

3. Deposit the multilayer stack on the surface (Recipe B.15)

4. Perform electron beam lithography with ZEP to open up trenches on the surface where SiON will be placed later.

5. Etch the full thickness of the MLS without over-etching, using Recipe B.12.

6. Remove any residual resist with a soft oxygen clean. (Recipe B.5)

7. Re-fill the etched trenches with PECVD SiON (Recipe B.16)

8. Spin-coat the sample with S1805 photoresist at 1 krpm to planarize the surface.

9. Etch-back the top surface until the MLS surface is reached (Recipe B.19)

10. Clean the sample with a soft O_2 clean. (Recipe B.5)

11. Perform the second electron beam lithography to define areas where SiO_2 cladding will be

deposited.

12. Etch the pattern such that the MLS is fully etched down again (do not base the etch rate on the SiON etch depth). (Recipe B.12)

13. Clean the sample with a soft O_2 clean. (Recipe B.5)

14. Deposit $\sim$ 1.3 μm SiO_2 as a side and top cladding. (Recipe B.14)

15. Cleave or polish the sample as necessary (B.1 if desired)

APPENDIX B: PROCESS RECIPES

B.1 Partial Dice & Cleave

Equipment: K&S 986-2 Plus Dicing Saw (should use a blade with ~ 250 μm thickness), diamond scribe

This procedure enables silicon waveguide facets to be prepared rapidly, and with fairly good quality. Other materials with sufficiently good adhesion to a silicon / silicon dioxide substrate are suitable for this method as well.

1. If necessary, coat the top surface of the sample with some kind of protective cladding prior to dicing, to avoid contamination (dicing is a very dirty process).

2. Examine the top surface of the chip and determine where the cleave is desired to occur. This process requires that cuts be made at least 4 mm from the edge of the chip. The first and last waveguides on the surface should be a minimum of 5 mm from the beginning and end of the cut, so as to allow the crack to straighten properly before reaching the devices.

3. Mount the sample upside down on the dicing saw mounting tape and secure with an extra piece of tape on top, oriented such that it will not be sliced apart during the cuts.

4. Align the sample such that the cuts will be made perpendicular to the waveguides. Note: the waveguides should be aligned as close to the crystalline axes of silicon as possible, to keep the cleave quality high and avoid shearing.

5. On each facet, execute six parallel cuts across the entire width of the sample, spaced by 100 μm from each other (they must overlap heavily). The cut depth should be such that roughly 150-200 μm of the substrate remain underneath.

6. Carefully remove the sample from the mounting tape, pulling in such a way as to avoid stresses

on the partially diced ledges. Any bending may result in a premature cleave, which will inevitably damage the facets from grinding and scraping.

7. Dry the sample off and set on a lint-free wipe (such as an AlphaWipe) on a hard, flat surface. Set it upside down such that the diced surface is visible.

8. Press gently down on the sample with two fingers, and lightly press with the diamond scribe at the beginning of one of the cuts. Be sure to press precisely in the middle of the cut. With very little force, the cut should cleave down the middle, resulting in a very smooth surface finish on the cleaved ledge.

9. Carefully separate the two pieces: avoid scraping them against one another!

10. Move the sample to a clean area on the cloth and repeat for the other cut (if necessary).

11. Inspect the cleaved-off bits under cross-sectional view on an optical microscope. The surface should appear uniform near the top where the waveguides are.

12. Clean off any temporary coating that may have been applied prior to dicing.

13. The facets are now fully prepared. Note that the ledges are mechanically sensitive and may snap off if the sample is pushed against a hard surface or dropped.

B.2 Silicon oxidation-based smoothing

1. Remove any existing oxides or surface cladding materials prior to oxidation by using dilute (1:10) HF:H_2O.

2. Load silicon sample into quartz tube furnace on a silica handle piece (do not use a microscope

slide, as it has a low melting point and will contaminate the furnace permanently).

3. In a wet oxygen environment, oxidize the sample at 1085°C for the required time (time can be calculated with various online tools). At lower temperatures, the viscosity of silica becomes small low enough that it does not effectively remove rough or sharp features. Thus, oxidation should be conducted at 1085°C or higher temperatures, depending on what the furnace is capable of.

4. Remove sample and let cool to room temperature.

5. Remove the new oxide if desired (or keep it on as a cladding). Use dilute HF or BOE if removal is required.

6. The process may be repeated if additional smoothing is required.

B.3 O_2 surface activation (APEX SLR ICP Etcher)

This achieves surface activation by pure O_2 plasma.

ICP Power: 600 W

RF / Bias Power: 15 W

Pressure: 15 mT

O_2 Flow: 50 sccm

Time: 40 sec.

B.4 O_2/Ar surface activation (APEX SLR ICP Etcher)

This achieves surface activation by a combination of O_2 and Ar plasma.

ICP Power: 600 W

RF / Bias Power: 15 W

Pressure: 15 mT

O_2 Flow: 10 sccm

Ar Flow: 40 sccm

Time: 40 sec.

B.5 Soft oxygen clean (APEX SLR ICP Etcher)

This recipe is useful for removing polymers or organic contamination without causing damage to most materials. Note: ChG may be sensitive to this, and it should be used with caution in that case. However, silicon and silicon dioxide will not be removed by this etch. Bear in mind that if a fluorine-based etch is used prior to this recipe, the oxygen clean will kick up fluorine radicals which can etch many materials. Whenever fluorine etches are used in the same chamber, be sure to run a dummy oxygen clean on a dummy wafer with no sample, in order to prevent this issue. Typically, 5 10 min of soft oxygen cleaning is sufficient.

ICP Power: 700 W

RF / Bias Power: 5 W

Pressure: 5 mT

O_2 Flow: 50 sccm

B.6 Pseudo-Bosch Silicon Etch (APEX SLR ICP Etcher)

This fluorine-based etch provides smooth sidewalls and a highly vertical etch profile for silicon features. SF_6 provides continuous chemical etching of exposed silicon on a sample. C_4F_8 provides passivation to the sidewalls, greatly diminishing the effects of SF_6 on vertical surfaces. Finally, argon is used to provide directional milling of the horizontal surface to break up the C_4F_8 and enable chemical etching of the floor.

ICP Power: 485 W

RF / Bias Power: 10 W

Pressure: 15 mT

SF_6 Flow: 12 sccm

C_4F_8 Flow: 20 sccm

Ar Flow: 20 sccm

B.7 Chlorine-based chalcogenide etch (Unaxis Shuttleline ICP Etcher)

This recipe is suitable for etching of Germanium-Antimony-Sulfide (GeSbS)-type chalcogenide glass films.

ICP Power: 100 W

RF / Bias Power: 50 W

Pressure: 5 mT

Cl_2 Flow: 2 sccm

Ar Flow: 40 sccm

B.8 Fluorine-based chalcogenide etch (Unaxis Shuttleline ICP Etcher)

This recipe is suitable for etching of Germanium-Antimony-Sulfide (GeSbS)-type chalcogenide glass films. This recipe attains more vertical etch profiles than Recipe 5, at the expense of slightly higher propagation losses.

ICP Power: 500 W

RF / Bias Power: 50 W

Pressure: 10 mT

CHF_3 Flow: 5 sccm

Ar Flow: 30 sccm

B.9 Rapid silicon back-side removal (BSR) (APEX SLR ICP Etcher)

This recipe is suitable for bulk, isotropic removal of silicon material from the sample, for example in the case of backside etching. For very deep etches, use a handle wafer which is resistant to the

etch, such as sapphire. Ensure that any sample detectors are satisfied despite the transparent handle material.

ICP Power: 300 W

RF / Bias Power:200 W

Pressure: 95 mT

SF_6 Flow: 20 sccm

Selectivity of etching for Si to SiO_2: about 30:1 Silicon etch rate: Depends heavily on the sample size, as the fluorine radical concentration can be consumed by large exposed areas.

B.10 Polishing silicon back-side removal (BSR) (APEX SLR ICP Etcher)

This recipe is intended to follow the previous recipe after most (but not all) of a sample backside has been removed. This recipe has superior selectivity to silicon dioxide, allowing it to stop on the BOX layer with wide tolerances to the timing, rather than simply punching through.

ICP Power: 450 W

RF / Bias Power:15 W

Pressure: 95 mT

SF_6 Flow: 50 sccm

Selectivity of etching for Si to SiO_2: about 300:1 Silicon etch rate: Depends heavily on the sample size, as the fluorine radical concentration can be consumed by large exposed areas.

B.11 Anisotropic SiO_2 etch (APEX SLR ICP Etcher)

This recipe is ideal for etching of vertical features into silicon dioxide, using a polymer hard-mask.

ICP Power: 750 W

RF / Bias Power:20 W

Pressure: 5 mT

CHF_3 Flow: 40 sccm

B.12 Multimaterial etch (SiO_2 and Si3N4) (APEX SLR ICP Etcher)

This recipe is a modified version of Recipe the previous recipe, making use of SF_6 added to the mix to speed up etching of silicon nitride without compromising the silicon dioxide etch rate.

ICP Power: 750 W

RF / Bias Power:15 W

Pressure: 6 mT

CHF_3 Flow: 40 sccm

SF_6 Flow: 10 sccm

B.13 Isotropic Silicon Etch (APEX Vision RIE)

This recipe allows quite isotropic etching of silicon surfaces.

RF / Bias Power: 30 W

Pressure: 900 mT

SF_6 Flow: 300 sccm

Temperature: 300°C

B.14 Silicon Dioxide RF (Vision 310 PECVD)

This recipe provides a general-purpose silicon dioxide coating, making use of RF plasma excitation rather than LF. It seems to have fairly low losses as a cladding or core material.

RF Power: 20 W

Pressure: 800 mT

SiH_4 Flow: 400 sccm

N_2O Flow: 1420 sccm

Temperature: 300°C

Deposition rate: 25 nm/min

B.15 Multilayer SiO_2/Si_3N_4 RF (Vision 310 PECVD)

This recipe is for PECVD deposition of a multilayer stack consisting of alternating layers of silicon nitride and silicon dioxide. The fill factors are chosen to give a TE refractive index of roughly 1.72 at 633 nm wavelength. Cycling this for a total of 15 pairs, a total thickness of $\sim$ 700 nm is obtained.

Step 1:

RF Power: 30 W

Pressure: 750 mT

SiH_4 Flow: 2000 sccm

NH_3 Flow: 40 sccm

Temperature: 300°C

Time: 2 min., 14 sec.

Step 2:

RF Power: 20 W

Pressure: 800 mT

SiH_4 Flow: 400 sccm

N_2O Flow: 1420 sccm

Temperature: 300°C

Time: 50 sec.

Repeat, with 1 min gas stabilization in between each step to allow sufficient purging of unwanted species before striking plasma.

B.16 Silicon Oxynitride (SiON) RF (Vision 310 PECVD)

This recipe uses RF plasma for PECVD deposition of silicon oxynitride films with a refractive index of approximately 1.68 at a wavelength of 633 nm.

RF Power: 30 W

Pressure: 950 mT

SiH_4 Flow: 1450 sccm

NH_3 Flow: 100 sccm

N_2O Flow: 115 sccm

Temperature: 300°C

B.17 Positive Optical Lithography (S1805/S1813

This recipe is for positive-tone contact lithography using the Microposit S18XX series of photoresists.

1. Dispense through a < 1 μm-pore particle filter and syringe onto substrate, and spin at the required speed per the datasheet's spin-speed curve.

2. Bake at the edge of a hotplate set to 115°C for 1 minute to slowly evaporate the bulk of the solvents.

3. Move to the middle of the hotplate and bake for an additional minute.

4. Expose on the Suss MJB4 aligner for the required time (roughly 3 seconds, but will vary based on thickness).

5. Develop with freshly poured AZ 726 developer solution for 5-15 seconds with moderate agitation.

6. Rinse with water and dry with N_2 gas.

7. If reflow smoothing of the resist pattern is required, bake at 140°C for 30 - 120 sec.

B.18 Image-Reversal Optical Lithography (AZ5214e)

This recipe is for positive-tone contact lithography using AZ5214e resist.

1. Dispense through a < 1 μm-pore particle filter and syringe onto substrate, and spin at 3000 rpm to produce 1400 nm of resist.

2. Perform a soft-bake of the resist on a hotplate at 90°C for 90 seconds on a hotplate.

3. Expose the pattern on the MJB4 aligner for 6 sec.

5. Perform a second hotplate bake at 105°C for 60 sec.

6. Flood-expose the pattern (no mask) on the MJB4 aligner for 16 sec.

7. Develop for 15 sec. with AZ 726 developer solution. Over-development will result in the erosion of desired areas.

8. To check the resist profile (if desired), cleave a dummy sample and inspect the resist cross-section through a high-magnification microscope. If performed correctly, a negative slope should

be observed, suitable for lift-off processing.

B.19 Etch-back - PR/SiON 1:1 (APEX SLR ICP Etcher)

This recipe is used to uniformly etch the top surface of a sample after planarization of SiON topography using S1805 photoresist. It is designed to give nearly identical etch-rates for these two materials to ”smooth out” differences on the surface.

ICP Power: 750 W

RF / Bias Power:20 W

Pressure: 5 mT

CHF_3 Flow: 25 sccm

Etch rate: $\sim$ 230 nm/min

LIST OF REFERENCES

1. Soref, R. & Larenzo, J. All-silicon active and passive guided-wave components for λ = 1.3 and 1.6 μm. *IEEE Journal of Quantum Electronics* **22,** 873–879. ISSN: 0018-9197 (1986).

2. Jalali, B., Yegnanarayanan, S. & Trinh, P. Integrated optical directional couplers in silicon-on-insulator. *Electronics Letters* **31,** 2097–2098. ISSN: 0013-5194 (1995).

3. Fischer, U., ZInke, T. & Petermann, K. *Integrated optical waveguide switches in SOI* in *1995 IEEE International SOI Conference Proceedings* (IEEE, 1995), 141–142. ISBN: 0-7803-2547-8. doi:10.1109/SOI.1995.526500. <http://ieeexplore.ieee.org/lpdocs/epic03/wrapper.htm?arnumber=526500>.

4. Trinh, P., Yegnanarayanan, S. & Jalali, B. 5 x 9 integrated optical star coupler in silicon-on-insulator technology. *IEEE Photonics Technology Letters* **8,** 794–796. ISSN: 1041-1135 (1996).

5. Jalali, B. *et al.* Advances in silicon-on-insulator optoelectronics. *IEEE Journal of Selected Topics in Quantum Electronics* **4,** 938–947. ISSN: 1077260X (1998).

6. Jalali, B. & Fathpour, S. Silicon Photonics. *Journal of Lightwave Technology* **24,** 4600–4615. ISSN: 0733-8724 (2006).

7. Connelly, M. J. *Semiconductor Optical Amplifiers* 169. ISBN: 0792376579. <http://books.google.com/books?hl=en{\&}lr={\&}id=vEhIB4HxfiUC{\&}pgis=1> (Springer, 2002).

8. Park, H., Fang, A. W., Kodama, S. & Bowers, J. E. Hybrid silicon evanescent laser fabricated with a silicon waveguide and III-V offset quantum wells. *Optics Express* **13,** 9460. ISSN: 1094-4087 (2005).

9. Fang, A. W. *et al.* Electrically pumped hybrid AlGaInAs-silicon evanescent laser. *Optics Express* **14,** 9203. ISSN: 1094-4087 (2006).

10. Hsiao, H.-K., Winick, K. A., Monnier, J. D. & Berger, J.-P. An infrared integrated optic astronomical beam combiner for stellar interferometry at 3-4 microm. *Optics express* **17,** 18489–500. ISSN: 1094-4087 (2009).

11. Soref, R. Mid-infrared photonics in silicon and germanium. *Nature Photonics* **4,** 495–497. ISSN: 1749-4885 (2010).

12. Soref, R. A., Emelett, S. J. & Buchwald, W. R. Silicon waveguided components for the long-wave infrared region. *Journal of Optics A: Pure and Applied Optics* **8,** 840–848. ISSN: 1464-4258 (2006).

13. Cheng, Z., Chen, X., Wong, C. Y., Xu, K. & Tsang, H. K. Mid-infrared Suspended Membrane Waveguide and Ring Resonator on Silicon-on-Insulator. *IEEE Photonics Journal* **4,** 1510–1519. ISSN: 1943-0655 (2012).

14. Simpson, J. *et al.* A single-polarization fiber. *Journal of Lightwave Technology* **1,** 370–374. ISSN: 0733-8724 (1983).

15. Lee, K. K. Y., Avniel, Y. & Johnson, S. G. Design strategies and rigorous conditions for single-polarization single-mode waveguides. *Optics Express* **16,** 15170. ISSN: 1094-4087 (2008).

16. Zhu, B. *et al. Space-, Wavelength-, Polarization-Division Multiplexed Transmission of 56-Tb/s over a 76.8-km Seven-Core Fiber* in *Optical Fiber Communication Conference/National Fiber Optic Engineers Conference 2011* (OSA, Washington, D.C., 2011), PDPB7. ISBN: 978-1-55752-906-0. doi:10.1364/OFC.2011.PDPB7. <https://www.osapublishing.org/abstract.cfm?uri=OFC-2011-PDPB7>.

17. Eggleton, B. J., Luther-Davies, B. & Richardson, K. Chalcogenide photonics. *Nat Photon* **5,** 141–148. ISSN: 1749-4885 (2011).

18. Claps, R., Dimitropoulos, D., Raghunathan, V., Han, Y. & Jalali, B. Observation of stimulated Raman amplification in silicon waveguides. *Optics Express* **11,** 1731. ISSN: 1094-4087 (2003).

19. Claps, R., Dimitropoulos, D. & Jalali, B. Stimulated Raman scattering in silicon waveguides. *Electronics Letters* **38,** 1352. ISSN: 00135194 (2002).

20. Boyraz, O. & Jalali, B. Demonstration of a silicon Raman laser. *Optics Express* **12,** 5269. ISSN: 1094-4087 (2004).

21. Rong, H. *et al.* A continuous-wave Raman silicon laser. *Nature* **433,** 725–8. ISSN: 1476-4687 (2005).

22. Miller, G. D. *et al.* 42%-efficient single-pass cw second-harmonic generation in periodically poled lithium niobate. *Optics Letters* **22,** 1834. ISSN: 0146-9592 (1997).

23. Eyres, L. A. *et al.* All-epitaxial fabrication of thick, orientation-patterned GaAs films for nonlinear optical frequency conversion. *Applied Physics Letters* **79,** 904. ISSN: 00036951 (2001).

24. Baehr-Jones, T. *et al.* Silicon-on-sapphire integrated waveguides for the mid-infrared. *Optics express* **18,** 12127–35. ISSN: 1094-4087 (2010).

25. Shankar, R., Bulu, I. & Loncar, M. Integrated high-quality factor silicon-on-sapphire ring resonators for the mid-infrared. *Applied Physics Letters* **102,** 051108. ISSN: 00036951 (2013).

26. Khan, S., Chiles, J., Ma, J. & Fathpour, S. Silicon-on-nitride waveguides for mid- and near-infrared integrated photonics. *Applied Physics Letters* **102,** 121104. ISSN: 00036951 (2013).

27. Borlaug, D., Fathpour, S. & Jalali, B. Extreme Value Statistics in Silicon Photonics. *IEEE Photonics Journal* **1,** 33–39. ISSN: 1943-0655 (2009).

28. Lau, R. K. W. *et al.* Octave-spanning mid-infrared supercontinuum generation in silicon nanowaveguides. *Optics letters* **39,** 4518–21. ISSN: 1539-4794 (2014).

29. Kuyken, B *et al.* Generation of 3.6 μm radiation and telecom-band amplification by four-wave mixing in a silicon waveguide with normal group velocity dispersion. *Optics letters* **39,** 1349–52. ISSN: 1539-4794 (2014).

30. Densmore, A. *et al.* Compact and low power thermo-optic switch using folded silicon waveguides. *Optics Express* **17,** 10457. ISSN: 1094-4087 (2009).

31. Nedeljkovic, M. *et al.* Mid-Infrared Thermo-Optic Modulators in SoI. *IEEE Photonics Technology Letters* **26,** 1352–1355. ISSN: 1041-1135 (2014).

32. Tu, X. *et al.* 50-Gb/s silicon optical modulator with traveling-wave electrodes. *Optics express* **21,** 12776–82. ISSN: 1094-4087 (2013).

33. Thomson, D. J. *et al.* Optical detection and modulation at 2µm-2.5µm in silicon. *Optics express* **22,** 10825–30. ISSN: 1094-4087 (2014).

34. Nedeljkovic, M., Soref, R. & Mashanovich, G. Z. Free-Carrier Electrorefraction and Electroabsorption Modulation Predictions for Silicon Over the 114-μm Infrared Wavelength Range. *IEEE Photonics Journal* **3,** 1171–1180. ISSN: 1943-0655 (2011).

35. Chmielak, B. *et al.* Pockels effect based fully integrated, strained silicon electro-optic modulator. *Optics express* **19,** 17212–9. ISSN: 1094-4087 (2011).

36. Palmer, R. *et al.* High-Speed, Low Drive-Voltage Silicon-Organic Hybrid Modulator Based on a Binary-Chromophore Electro-Optic Material. *J. Lightwave Technol.* **32,** 2726–2734 (2014).

37. Noguchi, K., Mitomi, O. & Miyazawa, H. Millimeter-Wave Ti:LiNbO3 Optical Modulators. *J. Lightwave Technol.* **16,** 615– (1998).

38. Becker, R. A., Rediker, R. H. & Lind, T. A. Wide-bandwidth guided-wave electro-optic intensity modulator at λ=3.39 μm. *Applied Physics Letters* **46,** 809. ISSN: 00036951 (1985).

39. Lee, Y. S. *et al.* Hybrid Si-LiNbO microring electro-optically tunable resonators for active photonic devices. *Optics letters* **36,** 1119–21. ISSN: 1539-4794 (2011).

40. Chen, L., Xu, Q., Wood, M. G. & Reano, R. M. Hybrid silicon and lithium niobate electro-optical ring modulator. *Optica* **1,** 112. ISSN: 2334-2536 (2014).

41. Solmaz, M. & Madsen, C. K. *Silicon-on-Lithium Niobate Waveguides for Mid-Infrared* in (eds Analoui, M., Belyanin, A. A., Drezek, R. A., Gmachl, C. F. & Robinson, J. P.) **6386** (2006), 63860F–63860F–10. doi:10.1117/12.691089. <http://proceedings.spiedigitallibrary.org/proceeding.aspx?articleid=1332591>.

42. Cao, L., Aboketaf, A., Wang, Z. & Preble, S. Hybrid amorphous silicon (a-Si:H)LiNbO3 electro-optic modulator. *Optics Communications* **330,** 40–44. ISSN: 00304018 (2014).

43. Dave, U. D. *et al.* Telecom to mid-infrared spanning supercontinuum generation in hydrogenated amorphous silicon waveguides using a Thulium doped fiber laser pump source. *Optics express* **21,** 32032–9. ISSN: 1094-4087 (2013).

44. Rabiei, P., Ma, J., Khan, S., Chiles, J. & Fathpour, S. Heterogeneous lithium niobate photonics on silicon substrates. *Optics express* **21,** 25573–81. ISSN: 1094-4087 (2013).

45. Chiles, J. & Fathpour, S. *Silicon on Lithium Niobate: A Hybrid Electro-Optical Platform for Near- and Mid-Infrared Photonics* in *CLEO: 2014* (OSA, Washington, D.C., 2014), STh1M.6. ISBN: 978-1-55752-999-2. doi:10.1364/CLEO_SI.2014.STh1M.6. <http://www.opticsinfobase.org/abstract.cfm?URI=CLEO{_}SI-2014-STh1M.6>.

46. Chiles, J. & Fathpour, S. Mid-infrared integrated waveguide modulators based on silicon-on-lithium-niobate photonics. *Optica* **1,** 350. ISSN: 2334-2536 (2014).

47. Chiles, J. & Fathpour, S. *On-Chip Modulation in the Mid-Infrared with Silicon-on-Lithium-Niobate Photonics* in *CLEO: 2015* (OSA, Washington, D.C., 2015), STu4I.5. ISBN: 978-1-55752-968-8. doi:10.1364/CLEO_SI.2015.STu4I.5. <https://www.osapublishing.org/abstract.cfm?uri=CLEO{_}SI-2015-STu4I.5>.

48. Wooten, E. *et al.* A review of lithium niobate modulators for fiber-optic communications systems. *IEEE Journal of Selected Topics in Quantum Electronics* **6,** 69–82. ISSN: 1077-260X (2000).

49. Lin, H. *et al.* Demonstration of high-Q mid-infrared chalcogenide glass-on-silicon resonators. *Optics letters* **38,** 1470–2. ISSN: 1539-4794 (2013).

50. Ito, H., Takyu, C. & Inaba, H. Fabrication of periodic domain grating in LiNbO3 by electron beam writing for application of nonlinear optical processes. *Electronics Letters* **27,** 1221. ISSN: 00135194 (1991).

51. Chiles, J., Khan, S., Ma, J. & Fathpour, S. High-contrast, all-silicon waveguiding platform for ultra-broadband mid-infrared photonics. *Applied Physics Letters* **103,** 151106. ISSN: 00036951 (2013).

52. Chiles, J., Khan, S. & Fathpour, S. *Wafer-Fusion-Enabled Platforms for Mid-Infrared Integrated Silicon Photonics* in *2014 IEEE Photonics Society Summer Topical Meeting Series* (IEEE, 2014), 47–48. ISBN: 978-1-4799-2767-8. doi:10.1109/SUM.2014.35. <http://ieeexplore.ieee.org/lpdocs/epic03/wrapper.htm?arnumber=6902980>.

53. Xiu, K. & Ketchen, M. *Hierarchical Thermal Modeling for SOI Technology* in *IEEE SemiTherm Symposium* (2004).

54. Bengtsson, S. Low-Temperature Preparation of Silicon/Silicon Interfaces by the Silicon-to-Silicon Direct Bonding Method. *Journal of The Electrochemical Society* **137,** 2297. ISSN: 00134651 (1990).

55. Bruel, M. *Process for the production of thin semiconductor material films* 1994.

56. Oskooi, A. F. *et al.* Meep: A flexible free-software package for electromagnetic simulations by the FDTD method. *Computer Physics Communications* **181,** 687–702 (2010).

57. Vassallo, C. Finite-difference derivation of the reflectivity at output facets of dielectric waveguides with a highly diverging output beam. *Journal of the Optical Society of America A* **15,** 717. ISSN: 1084-7529 (1998).

58. Khan, S. & Fathpour, S. Demonstration of complementary apodized cascaded grating waveguides for tunable optical delay lines. *Optics letters* **38,** 3914–7. ISSN: 1539-4794 (2013).

59. Dudley, J. M., Genty, G. & Coen, S. Supercontinuum generation in photonic crystal fiber. *Reviews of Modern Physics* **78,** 1135–1184. ISSN: 0034-6861 (2006).

60. Kuyken, B. *et al.* An octave-spanning mid-infrared frequency comb generated in a silicon nanophotonic wire waveguide. *Nature Communications* **6,** 6310. ISSN: 2041-1723 (2015).

61. Singh, N. *et al.* Midinfrared supercontinuum generation from 2 to 6μm in a silicon nanowire. *Optica* **2,** 797. ISSN: 2334-2536 (2015).

62. Saitoh, K. & Koshiba, M. Single-polarization single-mode photonic crystal fibers. *IEEE Photonics Technology Letters* **15,** 1384–1386. ISSN: 1041-1135 (2003).

63. Ju, J., Jin, W. & Demokan, M. S. Design of Single-Polarization Single-Mode Photonic Crystal Fiber at 1.30 and 1.55 m. *Journal of Lightwave Technology, Vol. 24, Issue 2, pp. 825-* **24,** 825 (2006).

64. Lin An *et al. Ultra-wideband single-polarization single-mode photonic crystal fiber with high nonlinearity and low dispersion* 2009.

65. X. Zheng, Y. G. Liu, Z. Wang, T. Han & B. Tai. Tunable Single-Polarization Single-Mode Photonic Crystal Fiber Based on Liquid Infiltrating. *IEEE Photonics Technology Letters* **23,** 709–711. ISSN: 1041-1135 (2011).

66. Dell'Olio, F., Tatoli, T., Ciminelli, C. & Armenise, M. N. Recent advances in miniaturized optical gyroscopes. *Journal of the European Optical Society: Rapid Publications* **9,** 14013. ISSN: 1990-2573 (2014).

67. Johnson, A. R. *et al.* Octave-spanning coherent supercontinuum generation in a silicon nitride waveguide. *Optics letters* **40,** 5117–20. ISSN: 1539-4794 (2015).

68. Yu, Y. *et al.* Experimental demonstration of linearly polarized 210μm supercontinuum generation in a chalcogenide rib waveguide. *Optics Letters* **41,** 958. ISSN: 0146-9592 (2016).

69. Oliner, A., Song-Tsuen Peng, S.-T., Ting-Ih Hsu, T.-I. & Sanchez, A. Guidance and Leakage Properties of a Class of Open Dielectric Waveguides: Part II–New Physical Effects. *IEEE Transactions on Microwave Theory and Techniques* **29,** 855–869. ISSN: 0018-9480 (1981).

70. Webster, M. A., Pafchek, R. M., Mitchell, A. & Koch, T. L. Width Dependence of Inherent TM-Mode Lateral Leakage Loss in Silicon-On-Insulator Ridge Waveguides. *IEEE Photonics Technology Letters* **19,** 429–431. ISSN: 1041-1135 (2007).

71. Chen, C.-H., Pang, L., Tsai, C.-H., Levy, U. & Fainman, Y. Compact and integrated TM-pass waveguide polarizer. *Optics Express* **13,** 5347. ISSN: 1094-4087 (2005).

72. Cheng, J. *et al.* Single polarization transmission in pedestal-supported silicon waveguides. *Optics letters* **36,** 1797–1799. ISSN: 1539-4794 (2011).

73. Chiles, J. & Fathpour, S. Demonstration of ultra-broadband single-mode and single-polarization operation in T-Guides. *Optics Letters* **41,** 3836. ISSN: 0146-9592 (2016).

74. Chiles, J. & Fathpour, S. Single-mode and single-polarization photonics with anchored-membrane waveguides. *Optics Express* **24,** 19337. ISSN: 1094-4087 (2016).

75. Singh, N., Hudson, D. D. & Eggleton, B. J. Silicon-on-sapphire pillar waveguides for Mid-IR supercontinuum generation. *Optics express* **23,** 17345–54. ISSN: 1094-4087 (2015).

76. Powell, O. Single-mode condition for silicon rib waveguides. *Journal of Lightwave Technology* **20,** 1851–1855. ISSN: 0733-8724 (2002).

77. Ma, J. & Fathpour, S. Noise figure in near-infrared amorphous and mid-infrared crystalline silicon optical parametric amplifiers. *Journal of Lightwave Technology* **31,** 3181–3187. ISSN: 07338724 (2013).

78. Ma, J & Fathpour, S. Pump-to-Stokes relative intensity noise transfer and analytical modeling of mid-infrared silicon Raman lasers. *Optics express* **20,** 17962–72. ISSN: 1094-4087 (2012).

79. Tyo, J. S., Goldstein, D. L., Chenault, D. B. & Shaw, J. A. Review of passive imaging polarimetry for remote sensing applications. *Applied Optics* **45,** 5453. ISSN: 0003-6935 (2006).

80. Tan, S. & Narayanan, R. M. Design and performance of a multiwavelength airborne polarimetric lidar for vegetation remote sensing. *Applied Optics* **43,** 2360. ISSN: 0003-6935 (2004).

81. Goloub, P. *et al.* Cloud thermodynamical phase classification from the POLDER spaceborne instrument. *Journal of Geophysical Research: Atmospheres* **105,** 14747–14759. ISSN: 01480227 (2000).

82. Cornwell, D. Space-Based Laser Communications Break Threshold. *Optics and Photonics News* **27,** 24. ISSN: 1047-6938 (2016).

83. Dai, D. & Wu, H. Realization of a compact polarization splitter-rotator on silicon. *Optics Letters* **41,** 2346. ISSN: 0146-9592 (2016).

84. Kim, D. W., Lee, M. H., Kim, Y. & Kim, K. H. Planar-type polarization beam splitter based on a bridged silicon waveguide coupler. *Optics Express* **23,** 998. ISSN: 1094-4087 (2015).

85. Su, Z. *et al.* Four-port integrated polarizing beam splitter. *Optics Letters* **39,** 965. ISSN: 0146-9592 (2014).

86. Xiong, Y., Xu, D.-X., Schmid, J. H., Cheben, P. & Ye, W. N. High Extinction Ratio and Broadband Silicon TE-Pass Polarizer Using Subwavelength Grating Index Engineering. *IEEE Photonics Journal* **7,** 1–7. ISSN: 1943-0655 (2015).

87. Shahin, M. M., Gevorgyan, H., Dahlem, M. & Khilo, A. *TM-Polarizer using Segmented Silicon Waveguide* in *Advanced Photonics 2015* (OSA, Washington, D.C., 2015), IM2A.4. ISBN: 978-1-55752-000-5. doi:10.1364/IPRSN.2015.IM2A.4. <https://www.osapublishing.org/abstract.cfm?URI=IPRSN-2015-IM2A.4>.

88. Kapon, E. *Polarizing optical waveguides* 1989.

89. Suzuki, Y., Iwamura, H. & Mikami, O. TE/TM mode selective channel waveguides in GaAs/AlAs superlattice fabricated by SiO2 cap disordering. *Applied Physics Letters* **56,** 19. ISSN: 00036951 (1990).

90. Suzuki, Y., Iwamura, H., Miyazawa, T. & Mikami, O. A novel waveguided polarization mode splitter using refractive index changes induced by superlattice disordering. *IEEE Journal of Quantum Electronics* **30,** 1794–1800. ISSN: 00189197 (1994).

91. Watanabe, O., Tsuchimori, M., Okada, A. & Ito, H. Mode selective polymer channel waveguide defined by the photoinduced change in birefringence. *Applied Physics Letters* **71,** 750. ISSN: 00036951 (1997).

92. Min-Cheol Oh, M.-C., Myung-Hyun Lee, M.-H. & Hyung-Jong Lee, H.-J. Polymeric waveguide polarization splitter with a buried birefringent polymer. *IEEE Photonics Technology Letters* **11,** 1144–1146. ISSN: 1041-1135 (1999).

93. Forrest, S. R., So, F. F. & Zang, D. Y. *Polarization-selective integrated optoelectronic devices incorporating crystalline organic thin films* 1992.

94. Sun, R., Cheng, J., Michel, J. & Kimerling, L. Transparent amorphous silicon channel waveguides and high-Q resonators using a damascene process. *Optics Letters* **34,** 2378. ISSN: 0146-9592 (2009).

95. Li, L. *et al.* Integrated flexible chalcogenide glass photonic devices. *Nature Photonics* **8,** 643–649. ISSN: 1749-4885 (2014).

96. Zou, Y. *et al.* High-Performance, High-Index-Contrast Chalcogenide Glass Photonics on Silicon and Unconventional Non-planar Substrates. *Advanced Optical Materials* **2,** 478–486. ISSN: 21951071 (2014).

97. Gai, X., Choi, D.-Y., Madden, S. & Luther-Davies, B. Polarization-independent chalcogenide glass nanowires with anomalous dispersion for all-optical processing. *Optics express* **20,** 13513–21. ISSN: 1094-4087 (2012).

98. Chiles, J. *et al.* Low-loss, submicron chalcogenide integrated photonics with chlorine plasma etching. *Applied Physics Letters* **106,** 111110. ISSN: 0003-6951 (2015).

99. Chiles, J. *et al. Extremely Low-Loss Chalcogenide Photonics Devices with Chlorine-Based Plasma Etching* in *CLEO: 2015* (OSA, Washington, D.C., 2015), STh1G.6. ISBN: 978-1-55752-968-8. doi:10.1364/CLEO_SI.2015.STh1G.6. <https://www.osapublishing.org/abstract.cfm?uri=CLEO{_}SI-2015-STh1G.6>.

100. Nazabal, V. *et al.* Chalcogenide coatings of Ge_15Sb_20S_65 and Te_20As_30Se_50. *Applied Optics* **47,** C114. ISSN: 0003-6935 (2008).

101. Petit, L. *et al.* Correlation between physical, optical and structural properties of sulfide glasses in the system GeSbS. *Materials Chemistry and Physics* **97,** 64–70. ISSN: 02540584 (2006).

102. Musgraves, J. *et al.* Comparison of the optical, thermal and structural properties of GeSbS thin films deposited using thermal evaporation and pulsed laser deposition techniques. *Acta Materialia* **59,** 5032–5039. ISSN: 13596454 (2011).

103. Langhoff, C. A., Stokich, T. & Heistand, B. *BenzoCycloButene (BCB): a polymeric system for passive optical interconnects* in *OE/LASE'93: Optics, Electro-Optics, & Laser Applications in Science& Engineering* (ed Chen, R. T.) (International Society for Optics and Photonics, 1993), 336–341. doi:10.1117/12.147110. <http://proceedings.spiedigitallibrary.org/proceeding.aspx?articleid=1005492>.

104. Rabus, D. G. *Integrated Ring Resonators* 5. ISBN: 978-3-540-68786-3. doi:10.1007/978-3-540-68788-7. <http://www.springerlink.com/index/10.1007/978-3-540-68788-7> (Springer Berlin Heidelberg, Berlin, Heidelberg, 2007).

105. Scherer, D. *et al. Characterization of Mid-Infrared Interband Cascade Laser Coupling to a GeSbS Chalcogenide Glass Waveguide* 2012.

106. Hu, J. *et al.* Si-CMOS-compatible lift-off fabrication of low-loss planar chalcogenide waveguides. *Optics Express* **15,** 11798. ISSN: 1094-4087 (2007).

107. Raghunathan, V., Borlaug, D., Rice, R. R. & Jalali, B. Demonstration of a Mid-infrared silicon Raman amplifier. *Optics Express* **15,** 14355. ISSN: 1094-4087 (2007).

108. MA, J. *NONLINEAR INTEGRATED PHOTONICS ON SILICON AND GALLIUM ARSENIDE SUBSTRATES* PhD thesis (University of Central Florida, 2014).

109. Rong, H. *et al.* A cascaded silicon Raman laser. *Nature Photonics* **2,** 170–174. ISSN: 1749-4885 (2008).

110. Fischer, U., Zinke, T., Kropp, J.-R., Arndt, F. & Petermann, K. 0.1 dB/cm waveguide losses in single-mode SOI rib waveguides. *IEEE Photonics Technology Letters* **8,** 647–648. ISSN: 1041-1135 (1996).

111. Jones, R., Cohen, O., Hak, D. & Paniccia, M. Optical amplification and lasing by stimulated Raman scattering in silicon waveguides. *Journal of Lightwave Technology* **24,** 1440–1455. ISSN: 0733-8724 (2006).

112. Collar, A. *et al.* Low residual reflectivity of angled-facet semiconductor laser amplifiers. *IEEE Photonics Technology Letters* **2,** 553–555. ISSN: 1041-1135 (1990).

113. Shah, L. *et al. Backside Surface Machining of Silicon Wafers Using a Nanosecond Tm:fiber MOPA System* in *CLEO: 2013* (OSA, Washington, D.C., 2013), JTh2A.07. ISBN: 978-1-55752-972-5. doi:10.1364/CLEO_QELS.2013.JTh2A.07. <http://www.osapublishing.org/abstract.cfm?uri=CLEO{_}QELS-2013-JTh2A.07>.

114. Bjork, G. & Nilsson, O. A new exact and efficient numerical matrix theory of complicated laser structures: properties of asymmetric phase-shifted DFB lasers. *Journal of Lightwave Technology* **5,** 140–146. ISSN: 0733-8724 (1987).

115. Marcus, R. B. & Sheng, T. T. The Oxidation of Shaped Silicon Surfaces. *Journal of The Electrochemical Society* **129,** 1278. ISSN: 00134651 (1982).

116. Doerr, C. R. & Okamoto, K. Advances in Silica Planar Lightwave Circuits. *Journal of Lightwave Technology, Vol. 24, Issue 12, pp. 4763-4789* **24,** 4763–4789 (2006).

117. Boyd, R. W. *Nonlinear Optics* 578. ISBN: 0121216829. <http://books.google.com/books/about/Nonlinear{_}Optics.html?id=30t9VmOmOGsC{\&}pgis=1> (Acad. Press, 2003).

118. Van der Ziel, J. P., Miller, R. C., Logan, R. A., Jr., W. A. N. & Mikulyak, R. M. Phase-matched second-harmonic generation in GaAs optical waveguides by focused laser beams. *Applied Physics Letters* **25,** 238. ISSN: 00036951 (1974).

119. Ducci, S. *et al.* Continuous-wave second-harmonic generation in modal phase matched semiconductor waveguides. *Applied Physics Letters* **84,** 2974. ISSN: 00036951 (2004).

120. Jager, M., Stegeman, G. I., Flipse, M. C., Diemeer, M. & Mohlmann, G. Modal dispersion phase matching over 7 mm length in overdamped polymeric channel waveguides. *Applied Physics Letters* **69,** 4139. ISSN: 00036951 (1996).

121. Sohler, W. *et al. Integrated optical parametric oscillators with Ti:PPLN waveguides* in *(CLEO). Conference on Lasers and Electro-Optics, 2005.* **1** (IEEE, 2005), 195–197 Vol. 1. ISBN: 1-55752-795-4. doi:10.1109/CLEO.2005.201723. <http://ieeexplore.ieee.org/lpdocs/epic03/wrapper.htm?arnumber=1572789>.

122. Rao, A. *et al.* Heterogeneous microring and Mach-Zehnder modulators based on lithium niobate and chalcogenide glasses on silicon. *Optics Express* **23,** 22746. ISSN: 1094-4087 (2015).

123. Huang, X. G. & Wang, M. R. A novel quasi-phase-matching frequency doubling technique. *Optics Communications* **150,** 235–238. ISSN: 00304018 (1998).

124. Dong, P., Upham, J., Jugessur, A. & Kirk, A. G. Observation of continuous-wave second-harmonic generation in semiconductor waveguide directional couplers. *Optics Express* **14,** 2256. ISSN: 1094-4087 (2006).